

Original Article

Cite this article: Lan Z, Wu S, Roberts NMW, Zhang S, Cao R, Wang H, and Yang Y. Geochronological and geochemical constraints on the origin of highly $^{13}\text{C}_{\text{carb}}$ -depleted calcite in basal Ediacaran cap carbonate. *Geological Magazine* <https://doi.org/10.1017/S001675682200019X>

Received: 30 November 2021

Revised: 9 February 2022

Accepted: 28 February 2022

Keywords:


cap carbonate; South China; calcite U–Pb geochronology; calcite REE; LA-ICP-MS

Author for correspondence:

Zhongwu Lan,

Email: lzw1981@126.com

Geochronological and geochemical constraints on the origin of highly $^{13}\text{C}_{\text{carb}}$ -depleted calcite in basal Ediacaran cap carbonate

Zhongwu Lan^{1,2,3} , Shitou Wu¹, Nick M. W. Roberts⁴, Shujing Zhang⁵, Rong Cao^{1,6}, Hao Wang¹ and Yueheng Yang¹

¹State Key Laboratory of Lithospheric Evolution, Institute of Geology and Geophysics, Chinese Academy of Sciences, Beijing 100029, China; ²State Key Laboratory of Palaeobiology and Stratigraphy, Nanjing Institute of Geology and Palaeontology, Chinese Academy of Science, Nanjing 210008, Jiangsu, China; ³State Key Laboratory of Geological Processes and Mineral Resources, China University of Geosciences, Wuhan 430074, Hubei, China; ⁴Geochronology and Tracers Facility, British Geological Survey, Keyworth, NG12 5GG, UK; ⁵Department of Geology, School of Natural Sciences, Trinity College Dublin, Dublin 2, Ireland and ⁶University of Chinese Academy of Sciences, Beijing 100049, China

Abstract

Ediacaran cap dolostone atop Marinoan glacial deposits contains complex sedimentary structures with extremely negative $\delta^{13}\text{C}_{\text{carb}}$ values in close association with oscillations in palaeoclimatic and oceanographic proxy records. However, the precise geological, geochronological and geochemical context of the cap dolostone is not clarified, which hampers us from correctly interpreting the extremely negative $\delta^{13}\text{C}_{\text{carb}}$ values and their causal relationships with the Snowball Earth hypothesis. In this study, we conducted detailed *in situ* geochronological and geochemical analyses on the calcite within the cap dolostone from the Ediacaran Doushantuo Formation in South China in order to define its formation and relationship to the Snowball Earth hypothesis. Petrographic observations show that formation of dolomite pre-dates precipitation of calcite and pyrite, which pre-dates quartz cementation in the basal cap carbonate. Calcite cement within the cap dolostone yielded a U–Pb age of $636.5 \pm 7.4/17.8$ Ma (2σ , MSWD = 1.6, $n = 36/40$), which is within uncertainty of a published dolomite U–Pb age of 632 ± 17 Ma (recalculated as $629.3 \pm 16.7/22.9$ Ma). These age constraints negate the possibility that the calcite cement was formed by late Ediacaran or Cambrian hydrothermal activity. The rare earth element distribution patterns suggest a dominant seawater origin overprinted by subsequent early Ediacaran hydrothermal activity. The combined age, petrographic and geochemical data suggest oxidization of methane clathrates in response to complicated interplay between eustasy and isostatic rebound and hydrothermal fluids.

1. Introduction

The globally distributed Marinoan cap dolostone overlying the Marinoan glaciogenic deposits represents a suite of unique sedimentary successions that continues to attract worldwide attention (Kennedy *et al.* 2001; Hoffman & Schrag, 2002; Jiang *et al.* 2003, 2006; Shields *et al.* 2007; Bao *et al.* 2008; Wang *et al.* 2008; Zhou *et al.* 2010, 2017; Bristow *et al.* 2011). Yet, the perplexing sedimentary structures and anomalously negative carbon isotope signals registered in the Marinoan cap dolostone make it difficult to explain the detailed sedimentological and petrographic context, although numerous geochemical and isotopic data have been intermittently reported. Specifically, the origin of calcite with extremely negative $\delta^{13}\text{C}$ values, and its petrographic and genetic relationships with paragenetic minerals and Marinoan deglaciation, remains disputed. Oxidization of methane was proposed to have offered excess CO_3^{2-} inducing carbonate precipitation and explained the observed extremely negative carbon isotope anomaly (Jiang *et al.* 2003; Kennedy *et al.* 2008; Wang *et al.* 2008), but whether such a process occurred during deposition/early diagenetic or later hydrothermal activity remains disputed (Zhou *et al.* 2010, 2017; Bristow *et al.* 2011). It follows that ascertaining the temporal sequence of calcite and paragenetic minerals and their formation mechanisms would contribute to our understanding of their causal relationships with the Snowball Earth hypothesis, as well as providing a sound interpretation of geochemical data.

Calcite has frequently been utilized in probing the timing and causal relationships of biological and environmental events recorded in carbonates by means of measuring radiogenic U–Pb and stable C–O isotopic systems and trace-element compositions (Wang *et al.* 2008; Bristow *et al.* 2011; Franchi *et al.* 2015; Kalliomäki *et al.* 2019; MacDonald *et al.* 2019; Roberts *et al.* 2020). This is because calcite commonly incorporates rare earth elements (REEs)

and uranium during its crystallization, making it a suitable host for REE analyses and a potential chronometer for U–Pb geochronology. Calcite REE compositions are used as key evidence to distinguish its origin, as variations in REE distribution patterns are suggestive of variations of circulating fluid chemistry. Specifically, calcite with low REE concentrations and a positive Eu anomaly commonly precipitates from hydrothermal fluids, whereas calcite with positive La and Gd anomalies, a superchondritic Y/Ho ratio and light REE (LREE) depletion commonly forms in normal seawater (Van Kranendonk *et al.* 2003; Franchi *et al.* 2015; Kalliomäki *et al.* 2019).

Owing to differential geochemical behaviour and the abundance of U and Pb in seawater (Ku *et al.* 1977; Shen & Boyle, 1987), marine carbonates are particularly suitable for U–Pb dating because of their commonly high U/Pb ratios (Rasbury *et al.* 2004). As such, calcite geochronology could potentially produce direct age constraints in various geoscience applications (Rasbury & Cole, 2009; Roberts *et al.* 2020). Laser ablation-inductively coupled plasma-mass spectrometry (LA-ICP-MS) has been demonstrated to be an effective tool for *in situ* calcite U–Pb dating and REE composition measurement because of rapid *in situ* spot analysis with adequate levels of precision (Li *et al.* 2014; Roberts & Walker, 2016; Coogan *et al.* 2016; Ring & Gerdes, 2016; Nuriel *et al.* 2017; Kalliomäki *et al.* 2019; MacDonald *et al.* 2019; Roberts *et al.* 2020; Wu *et al.* 2022). This paired approach proves robust in constraining the formation timing of calcite and fingerprinting the source of fluids and thus tracing fluid evolution processes. To this end, we carry out detailed REE and U–Pb isotope analyses combined with scanning electron microscope (SEM) and cathodoluminescence (CL) imaging techniques on calcite from the Marinoan cap dolostone at the Jiulongwan type section to decipher its genesis and timing of formation. The findings provide further constraints on our understanding of its relationship with the Snowball Earth hypothesis.

2. Geological setting and sampling information

The late Mesoproterozoic to earliest Neoproterozoic Jiangnan Orogeny resulted in the formation of the South China Block (SCB) by means of amalgamating the Yangtze Block to the northwest with the Cathaysia Block to the southeast, along the Jiangnan Orogen (Li *et al.* 2009). The SCB experienced a subsequent intra-continental rifting, and accommodated abundant well-preserved Neoproterozoic sedimentary successions in the Nanhua Basin: the largest Neoproterozoic basin in the SCB (Wang & Li, 2003). Such a suite of sedimentary successions is well exposed in the Hubei–Hunan–Guizhou–Guangxi regions of the Nanhua Basin. The Ediacaran Yangtze platform in South China developed on a Neoproterozoic rifted continental margin that is interpreted to have started along the southeastern side of the Yangtze Block at c. 800 Ma (Wang & Li, 2003; Jiang *et al.* 2007). The Ediacaran carbonate and siliciclastic rocks were assumed to have been accommodated in a passive margin setting (Jiang *et al.* 2003, 2007). Ediacaran sedimentary rocks in South China are composed of the fossiliferous Doushantuo and Dengying formations, which show a wide spatial occurrence around the Yangtze Block, preserving key biostratigraphic and chemostratigraphic records regarding the coevolution of life and environmental conditions (Fig. 1a, b; Lan *et al.* 2019 and references therein).

Previous sedimentological research suggests deposition of the Doushantuo Formation in two stages. The first stage witnessed deposition of the couplet of cap carbonate and overlying black

shale of the lower Doushantuo Formation in an open shelf/ramp depositional environment, whereas the second stage is typical of a rimmed carbonate shelf with a shelf-margin barrier separating the intra-shelf lagoon from open ocean settings (Jiang *et al.* 2011). The Yangtze Gorges area accommodated the most complete and continuous outcrops of the Doushantuo Formation exposed at the Jiulongwan, Huajipo and other sections (Jiang *et al.* 2011). The Doushantuo Formation is best exposed at the intra-shelf basin Jiulongwan section (Jiang *et al.* 2011). Therein, the Doushantuo Formation has a conformable contact with the underlying Nantuo Formation (Fig. 2a, b), and is composed of c. 160 m thick mixed shale and carbonate. The Nantuo Formation is dominated by glaciogenic greenish diamictite with minor sandstone beds correlative with the late Cryogenian ‘Marinoan glaciation’ (Lang *et al.* 2018). The Doushantuo Formation is dividable into, in ascending order, Member 1 composed of cap dolostone, Member 2 dominated by black shale, Member 3 dominated by dolostone and Member 4 composed exclusively of black shale (with carbonate concretions). Regionally traceable cap carbonates in the basal Doushantuo Formation show anomalously negative $^{13}\text{C}_{\text{carb}}$ excursions and intriguing sedimentary structures such as stromatolite-like cavities, botryoidal cemented breccias, layer-parallel sheet cracks and tepee-like positive reliefs (Jiang *et al.* 2003; Wang *et al.* 2008), which has led to them receiving the most intensive investigation among the worldwide Neoproterozoic successions.

A time interval between c. 635 Ma and 550 Ma was constrained for the depositional age of the Doushantuo Formation exposed at the Jiulongwan and Jijiawan sections by means of thermal ionization mass spectrometry (TIMS) U–Pb dating of zircon grains from two interbedded tuff beds around the basal Doushantuo Formation and near the Doushantuo–Dengying Formation boundary (Condon *et al.* 2005; Yang *et al.* 2021; Fig. 1c). The cap dolostone at the Jiulongwan section is mainly composed of three components; they are a disrupted poorly stratified limestone/dolostone layer, laminated limestone/dolostone displaying tepee-like structures, and laminated silty limestone/dolostone (Jiang *et al.* 2003; Fig. 1c). Multiple generations of botryoidal cements filled in irregular cavities possibly formed by vertical extension of micritic crusts (Jiang *et al.* 2003; Fig. 2c, d). The tepee-like structures display positive relief and are made up of laminated micrite and dolomicrite, which bear layer-parallel sheet cracks surrounding the host carbonate (Jiang *et al.* 2003). These characteristics suggest they were probably formed by means of layer-parallel compression and vertical extension (c.f. Hoffman & MacDonald, 2010). Sample 1-2 is a fresh grape-structured dolostone collected from the disrupted dolostone layer that is c. 130 cm below the c. 635 Ma tuff bed; it is mainly composed of dolomite and calcite that are quartz cemented (Fig. 2e).

3. Analytical methods

In this study, both imaging analysis and *in situ* element and isotope analyses were conducted in order to reveal the formation timing and origin of calcite and its relationship with a syngenetic mineral assemblage in cap dolostone, as detailed below.

3.a. Imaging analysis

Polished thin-sections were prepared for petrographic observations and selection of spots for *in situ* mineral chemistry and calcite geochronology. A Nikon Eclipse E800 microscope equipped with a

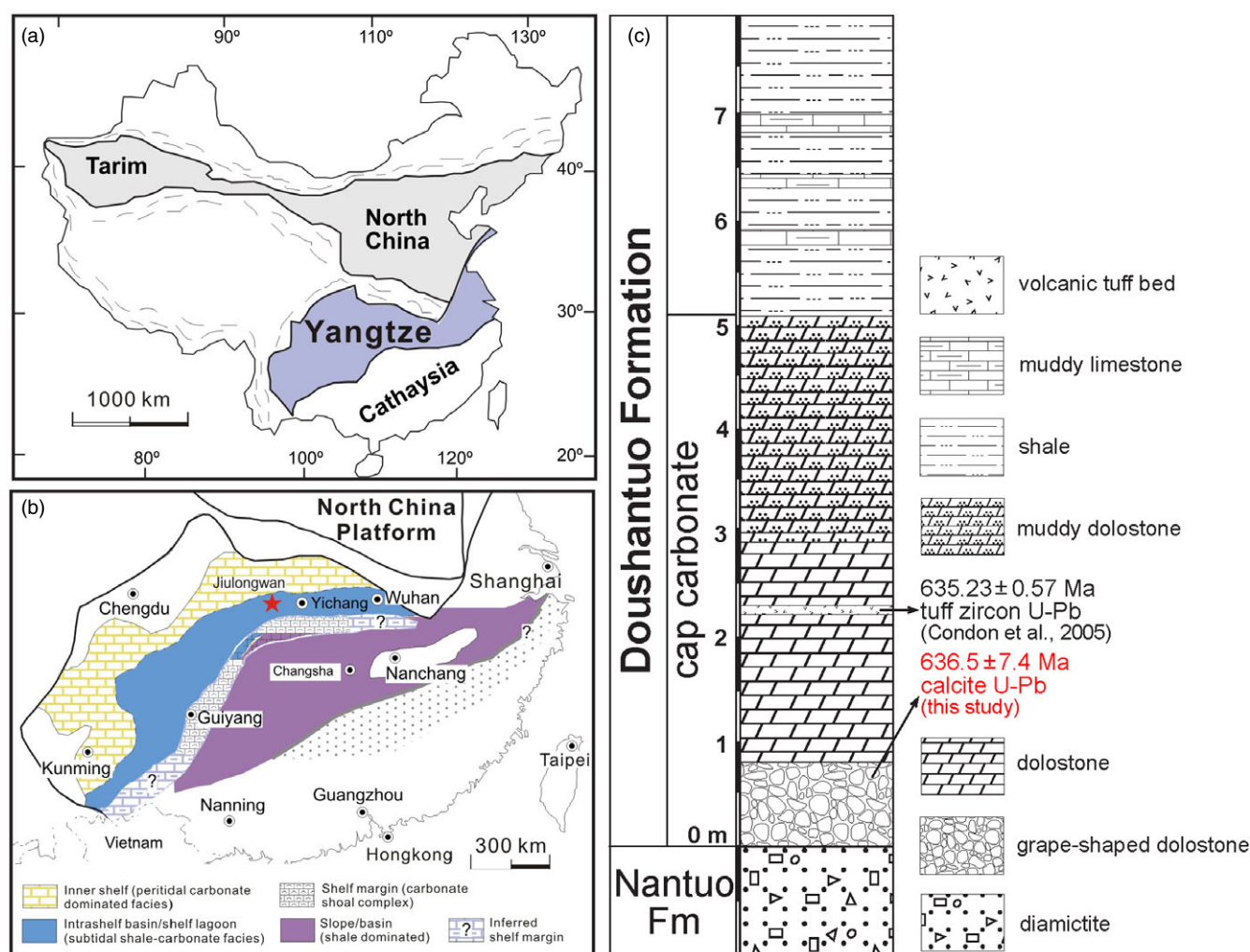


Fig. 1. (Colour online) (a) Geological map of China with the Yangtze platform highlighted in purple colour. (b) Reconstructed Ediacaran depositional environments on the Yangtze platform (Jiang *et al.* 2011). Red star marks the study location. (c) Stratigraphic column showing the sampling horizon in the cap dolostone of Doushantuo Formation.

Nikon DS-Fi 1 camera and Zeiss 1555 VP-FESEM at the State Key Laboratory of Lithospheric Evolution, Institute of Geology and Geophysics, Chinese Academy of Sciences (SKLE, IGGCAS) were utilized to detect textural relationships for syngenetic minerals. The SEM was specifically manipulated under backscattered electron mode to get an optimal resolution at 50–650 \times magnification. It was adjusted to an optimal working distance of 6–8 mm and a voltage of 10 kV. In order to obtain CL images of carbonates, a cold CL microscope at the Key Lab of Petroleum Resources at IGGCAS was utilized with a beam voltage of 16 kV, a current of 325 μA and a beam diameter of 4 mm.

3.b. Calcite REE composition analysis

Trace-element contents of calcite were determined by LA-ICP-MS employing an Element XR HR-ICP-MS instrument (Thermo Fisher Scientific, USA) coupled to a 193 nm ArF excimer laser system (Geolas HD, Lambda Physik, Göttingen, Germany) at SKLE, IGGCAS. The approach is similar to those outlined in Wu *et al.* (2018) with isotopes measured using a peak-hopping mode with a laser beam diameter of c. 44 μm , a repetition rate of 5 Hz and a laser energy density of ~ 3.0 J cm^{-2} . Helium was employed as the ablation gas to improve the transporting efficiency

of ablated aerosols. ARM-3 (Wu *et al.* 2019) reference glass was used as a calibration reference material, and BIR was analysed for data quality control. Calcium (^{40}Ca) was used as an internal standard. The resulting data were reduced using the GLITTER program (Griffin *et al.* 2008). For most trace elements (>0.05 $\mu\text{g/g}$), the accuracy is better than $\pm 10\%$ with analytical precision (1 RSD) of $\pm 10\%$.

3.c. Calcite U-Pb dating

Detailed procedures of the instrumentation and analytical protocol for calcite U-Pb dating are given in Wu *et al.* (2022) and are only briefly summarized herein. A Photo Machine Analyst G2 laser ablation system (Teledyne CETAC, Omaha, USA) coupled to an Element XR (Thermo Fisher Scientific, Bremen, Germany) was adopted to carry out *in situ* calcite U-Pb dating on polished thin-sections using LA-ICP-MS at SKLE, IGGCAS. A high-capacity vacuum pump was used to make the high-performance Jet sample cone work efficiently. The guard electrode was used to improve sensitivity (Wu *et al.* 2020a,b), while a T junction was adopted to add N_2 into the Ar sample gas flow behind the ablation cell.

A blind spot analysis was conducted using a laser beam of 80 μm to screen for high uranium regions for subsequent detailed



Fig. 2. (Colour online) Field and petrographic photos showing the cap dolostone of the Doushantuo Formation at the Jiulongwan section, Three Gorges area, South China. (a) The boundary between the Nantuo and Doushantuo formations. (b) Cap dolostone of the Doushantuo Formation. (c, d) Cap dolostone with botryoidal structures. Hammers in (c) and (d) are c. 35 cm long. (e) Merged reflected light images showing the petrography of grape-structured dolostone that is dominated by dolomite and calcite that are quartz cemented. D – dolomite; C – calcite; Q – quartz. The white dotted circles indicate laser analysis spots in calcite.

in situ U–Pb spot dating analysis. An automated mode in sequences of 60 to 80 spot analyses was used to acquire raw data. Each spot analysis is composed of 8 s of background acquisition followed by 25 s of sample ablation and 30 s washout. A peak jumping mode with a total integration time of 0.30 s to produce 130 mass scans was adopted to detect the signals of ^{202}Hg , $^{204}(\text{Hg} + \text{Pb})$, ^{206}Pb , ^{207}Pb , ^{208}Pb , ^{232}Th and ^{238}U during the data acquisition. In this study, a total of four reference materials (RMs) were used including two calcite U–Pb reference materials for calibration of U/Pb ratios and validation of the results (WC-1 and Duff Brown Tank; Hill *et al.* 2016; Roberts *et al.* 2017) and two glass reference materials for calibration of Pb/Pb ratios and

drift correction (ARM-3 and NIST SRM 614; Woodhead & Hergt, 2001; Wu *et al.* 2021). Two analyses of glass NIST SRM 614 and ARM-3 in combination with three analyses of WC-1 were analysed bracketing every ten analyses of unknown samples. The Duff Brown Tank (64.04 ± 0.67 Ma; Hill *et al.* 2016) was treated as an unknown sample to monitor data accuracy.

A total of 40 spot analyses were carried out on sample 1-2. The data reduction method follows those described recently by Wu *et al.* (2022), and uses the premise of calibrating against a material with known age but heterogeneous composition as per Roberts *et al.* (2017) and Chew *et al.* (2014). The Iolite 3.7 data reduction software and the VizualAge data reduction scheme were used to

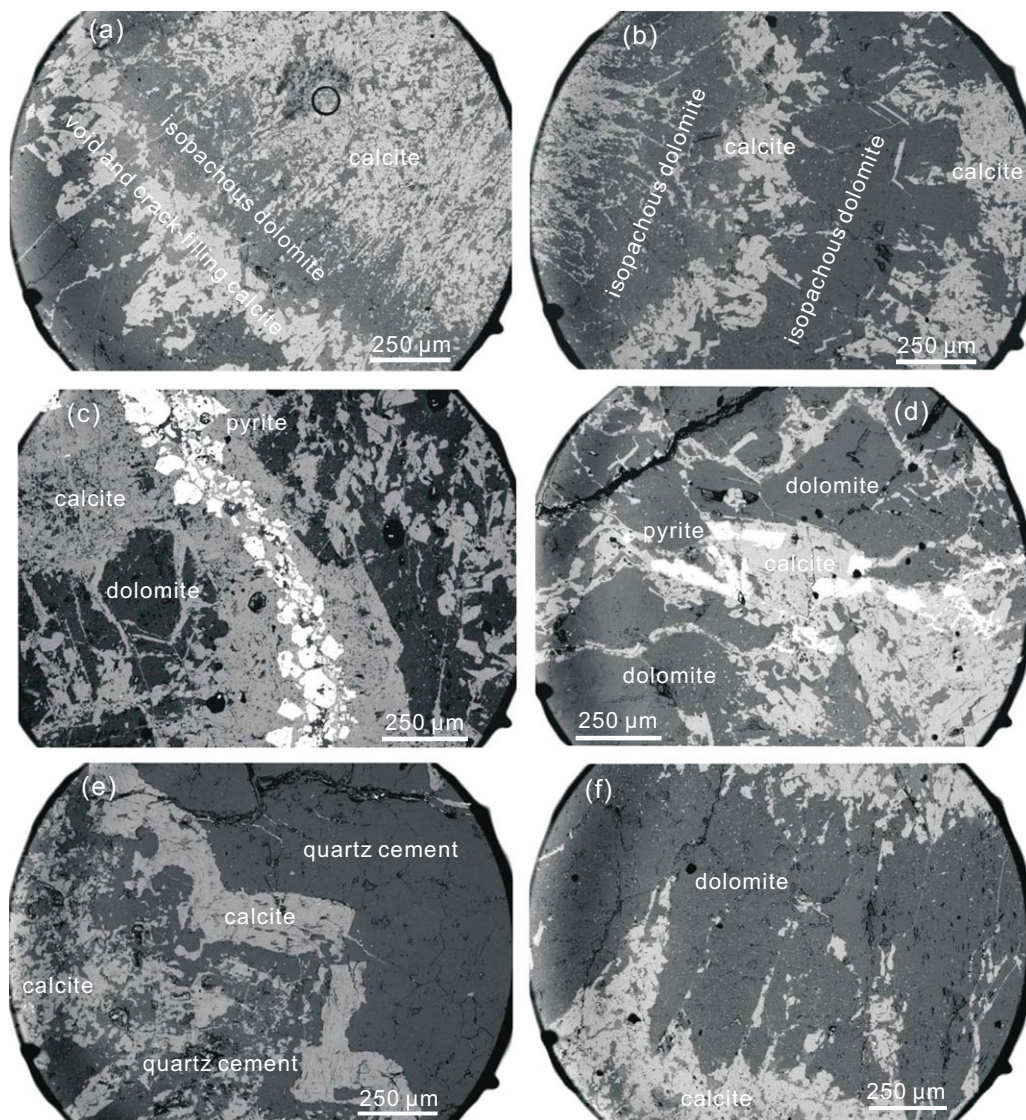


Fig. 3. Backscattered electron (BSE) images of cap dolostone showing paragenetic mineral assemblage. Initial dolostone deposition was followed by exposure and karstification due to isostatic rebound, forming voids and cracks that were subsequently filled by multidirectional straight or flexured pyrite and calcite cements/veins (a–e), which were then quartz cemented (e). The dolostone is mainly composed of isopachous dolomite. Black circle in (a) represents laser analysis spot.

reduce the raw data (time-resolved intensities) from the ICP-MS (Paton *et al.* 2011; Petrus & Kamber, 2012). Correction of instrument drift and calculation of isotope ratios of $^{207}\text{Pb}/^{206}\text{Pb}$ is accomplished by linear fit of ARM-3. The recommended value of $^{207}\text{Pb}/^{206}\text{Pb}$ is taken from Wu *et al.* (2021). NIST SRM 614 is used for the accuracy monitoring of $^{207}\text{Pb}/^{206}\text{Pb}$. Ten analyses of NIST SRM 614 yielded a mean of 0.8684 ± 0.0093 (2s), which is in agreement with the recommended value of 0.8710 ± 0.0004 (2s) (Baker *et al.* 2004). The downhole fractionation profile from ARM-3 glasses was used to calibrate the laser induced elemental fractionations of WC-1 and other samples (Wu *et al.* 2022). After the initial correction, WC-1 was used for further calibration of matrix-induced mass bias in $^{238}\text{U}/^{206}\text{Pb}$ ratios between RMs and unknown samples, which was accomplished in Microsoft Excel. The uncertainty propagation of LA-ICP-MS calcite geochronology is a modified approach based upon Horstwood *et al.* (2016), wherein the final age is quoted without and with systematic uncertainties, as $\pm \alpha/\beta$, respectively.

4. Results

4.a. Petrography of the studied samples

Field outcrops show that botryoidal structures and cavities widely occur in the basal cap dolostone, which is poorly stratified (Fig. 2a, c, d). Initial deposition of cap dolostone was followed by subsequent uplifting because of isostatic rebound, during which the cap dolostone experienced karstic dissolution in shallow marine to marginal depositional settings in South China, forming abundant cavities (Zhou *et al.* 2010). The botryoidal structures probably formed during a subsequent transgression, which induced a series of mineral precipitation within these cavities. The botryoidal structures not only encrust the bed surface but also the surface of cavities, with a thickness of 1–5 cm (Fig. 2c, d). Microscopic observations show the dolostone sample is mainly composed of dolomite, calcite, pyrite with minor barite and iron oxide (Figs 3, 4, 5). In most cases, calcite occurs as void and crack fillings among isopachous (about 200–500 μm thick) dolomite

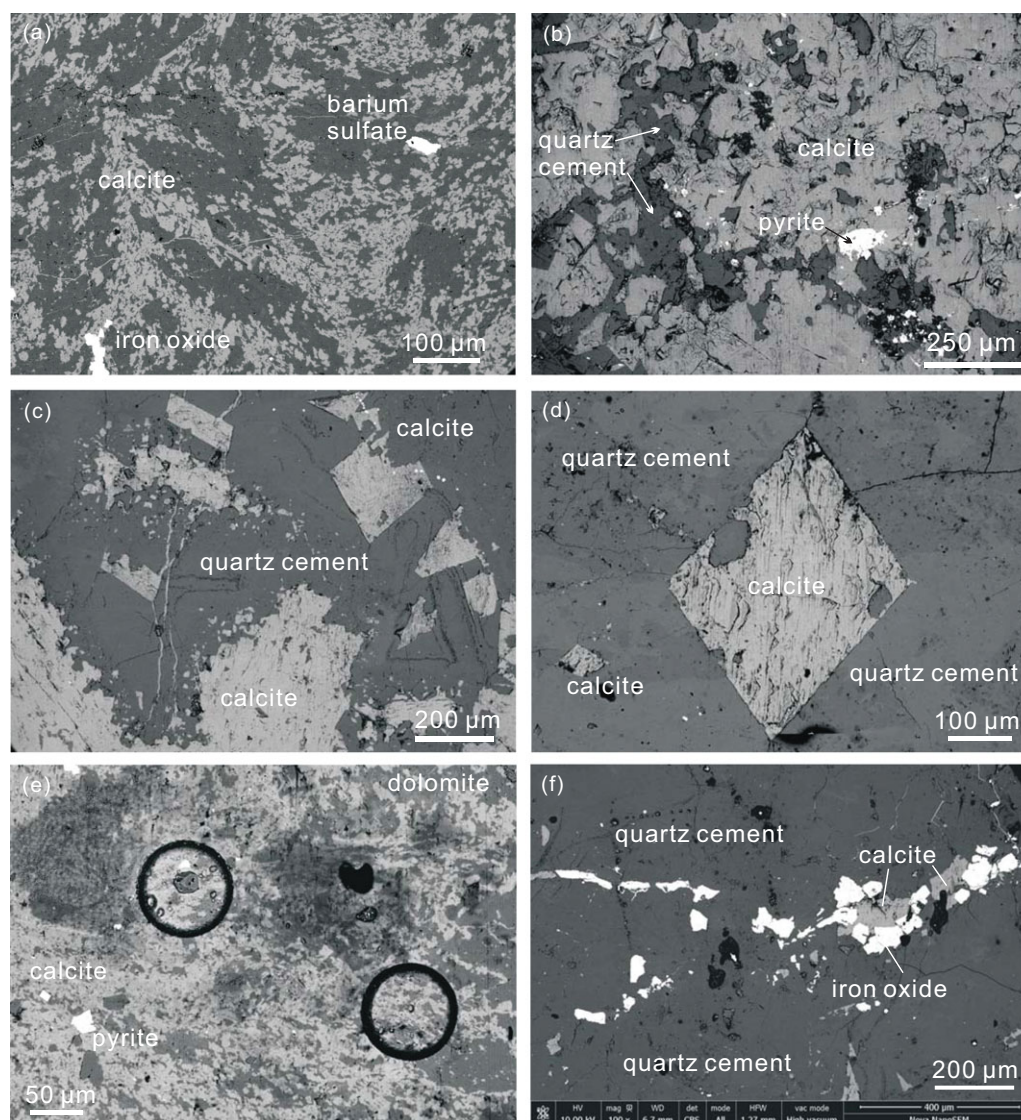


Fig. 4. Backscattered electron (BSE) images of cap dolostone showing paragenetic mineral assemblage. Various kinds of calcite cements/grains, pyrite or iron oxide, and barite filled in the cracks and cavities in dolostone that was formed via karstification, and was then quartz cemented. Black circles in (e) represent laser analysis spots.

(Fig. 3a, b, f). Most of the crack fillings display tapering ends. Finer cracks locally occur abundantly as meshworks (Fig. 3b, c). In some places, calcite veins, 30–500 μm thick, co-occur with pyrite (up to 250 μm) as vein fillings extending in various directions (Fig. 3c, d). Some calcite occurs as flexured isopachous veins, about 250 μm thick in quartz cements (recrystallized chalcedony and micro-quartz) (Fig. 3e). Aside from these phenomena, fibrous/amorphous calcite cements are seen to co-occur with fine barite and iron oxides/pyrite of 30–100 μm within dolomites (Fig. 4a, e). Amorphous quartz cement widely occurs filling the pore spaces of calcite cement (Fig. 4b) or entombing euhedral calcite or iron oxide grains (Fig. 4c, d). The euhedral calcite grains have a size range of 50–350 μm , some of which bear porous margins infilled by quartz cements (e.g. Fig. 4d). The iron oxides, 50–150 μm in size, are intimately associated with calcite (Fig. 4f). Under CL, calcite cements display a bright orange colour, whereas dolomite crystals show a blue colour (Fig. 5).

4.b. Calcite REE composition

LA-ICP-MS calcite REE compositions are tabulated in online Supplementary Material Table S1. Overall, the calcite shows a bell-shaped distribution pattern. They are characterized by positive La and Y anomalies, and high Y/Ho ratios (39–61 with an average of 50) (Fig. 6). Except for three points that have Y/Ho ratios of 39–41, the other 20 points all have Y/Ho ratios of >44. A prominent positive Gd anomaly is also present with δGd in the range of 1.1–1.96. Eu is dominated by positive anomalies ($\delta\text{Eu} = 1.02$ –1.38) with minor slightly negative anomalies ($\delta\text{Eu} = 0.79$ –0.96). $\text{Pr}_{\text{SN}}/\text{Yb}_{\text{SN}}$ ratios vary from 0.3 to 3.0 with an average of 0.9.

4.c. Calcite U-Pb geochronology

LA-ICP-MS calcite U-Pb dating results are tabulated in online Supplementary Material Table S2. A total of 185 spot analyses (over one month) were conducted for Duff Brown Tank, which

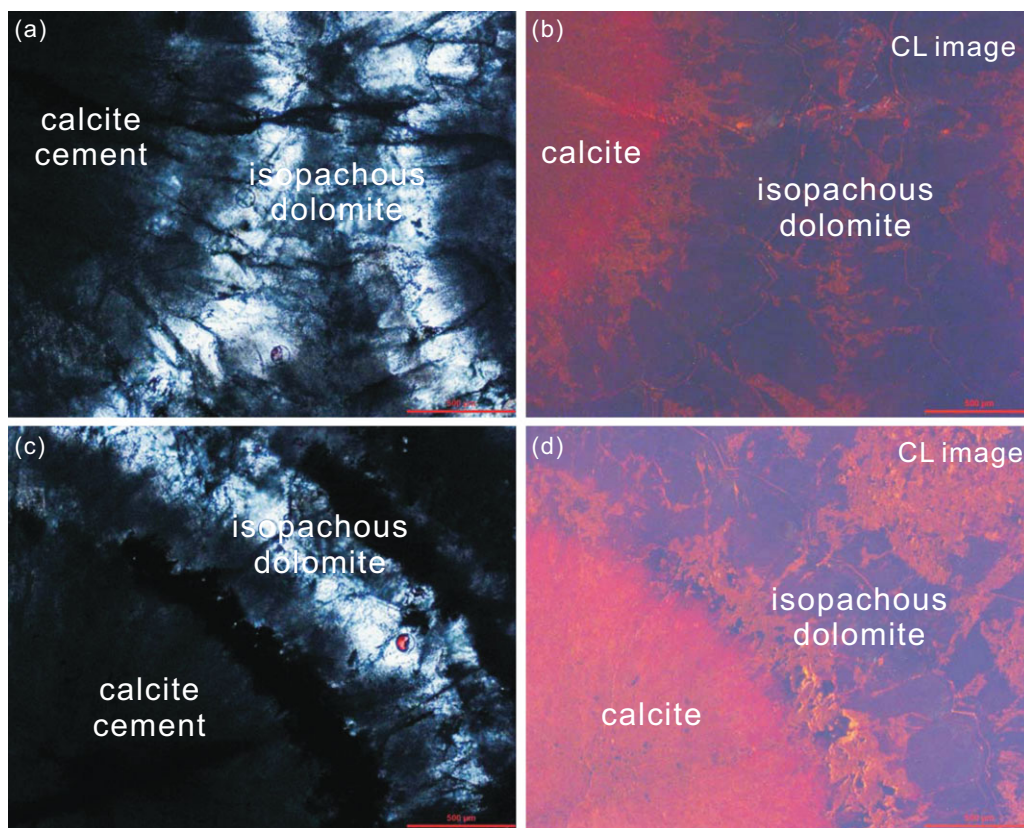


Fig. 5. (Colour online) Cathodoluminescence (CL) photomicrographs for sample 1-2 used as reference for choosing laser spots. (a) and (c) are reflected light images, whereas (b) and (d) are their corresponding CL images. Calcite cements show a distinct bright orange colour, which is in sharp contrast to the isopachous dolomite crystals which show a blue colour.

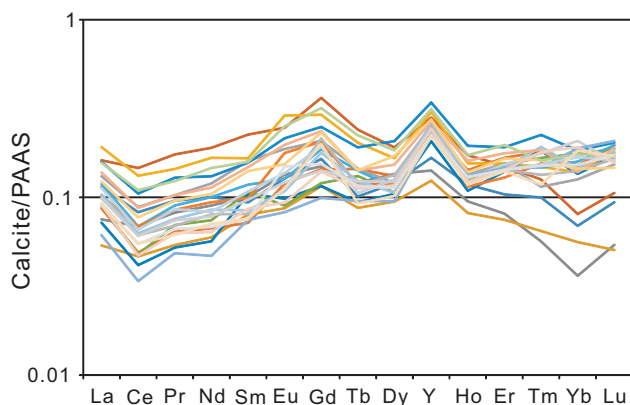


Fig. 6. (Colour online) Calcite rare earth element (REE) post-Archaean Australian shale (PAAS) normalized plot.

yielded a pooled age of 62.44 ± 0.91 Ma (MSWD = 7.2) (Fig. 7a), whereas 10 spot analyses during the analytical session for sample 1-2 yielded an intercept age of 62.63 ± 2.80 Ma (MSWD = 1.7). Both of these two ages are within uncertainty of the published isotope dilution age (Hill *et al.* 2016). These results suggest the long-term reproducibility across different analytical sessions is no larger than the limiting 2.5 % age uncertainty of the WC-1 reference material. During analysis, only calcite cements with smooth surfaces were chosen for U–Pb geochronology. A total of 40 spot analyses were conducted on the calcite cements of sample 1-2. Four

spots fall to the right of a distinct regression in Tera–Wasserburg space, and thus were removed; they may reflect a slight amount of open-system behaviour, i.e. U mobility, in the sampled region. The remaining 36 spots yield a lower intercept age of 636.5 ± 7.4 Ma (2σ , MSWD = 1.6, $n = 36/40$) (Fig. 7b). After propagation of decay constant and reference material (WC-1) uncertainties, the final age uncertainty that is required for age comparison is 17.8 Ma. As such, $636.5 \pm 7.4/17.8$ Ma is interpreted as the depositional age of the sampling horizon.

5. Discussion

5.a. Constraints on the cap dolostone

The complex sedimentary structures and anomalously negative carbon isotope signals registered in the cap dolostone are deemed to be associated with methane release induced by destabilization of low-latitude permafrost clathrates, which have aided in triggering the Marinoan deglaciation and subsequent flooding of continental shelves (Kennedy *et al.* 2001, 2008; Jiang *et al.* 2003). Authigenic calcite cements with extremely negative $\delta^{13}\text{C}_{\text{carb}}$ values (< -45 ‰) are the critical evidence in favour of the hypothesis that oxidization of methane hydrate offered excess CO_3^{2-} and induced the precipitation of cap dolostone (Jiang *et al.* 2003; Kennedy *et al.* 2008; Wang *et al.* 2008). It remains disputed, however, whether such a process occurred during deposition or early diagenesis, or during later hydrothermal activity (Zhou *et al.* 2010, 2017; Bristow *et al.* 2011). Our petrographic, geochemical and geochronological data demonstrate that these calcite cements were either originally

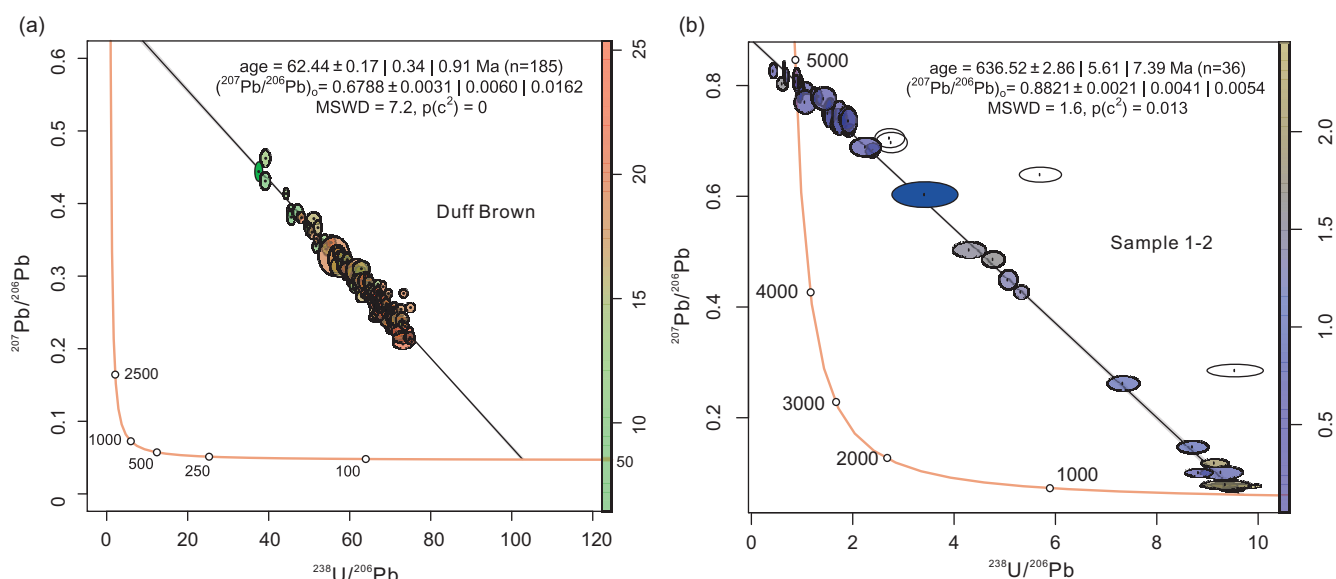


Fig. 7. (Colour online) Tera-Wasserburg Concordia plots (using IsoplotR; Vermeesch, 2018) of (a) reference material Duff Brown Tank and (b) sample 1-2. The upper intercepts define common Pb compositions, whereas the lower intercepts define dates that are quoted as $\pm \alpha/\beta$; see text for explanation.

precipitated in normal seawater and subsequently overprinted by early Ediacaran hydrothermal activities or were purely formed in early Ediacaran hydrothermal fluids, as detailed below.

It is commonly accepted that the shale-normalized REE + Y pattern of modern seawater is characterized by strong LREE depletion ($\text{Pr}_{\text{SN}}/\text{Yb}_{\text{SN}} = 0.2\text{--}0.4$), positive La and Gd ($\text{Gd}/\text{Gd}^* = 1.05\text{--}1.30$) and negative Ce anomalies, and super-chondritic Y/Ho ratios ranging from 44 to 74 (Franchi *et al.* 2015 and references therein). The post-Archaeon Australian shale (PAAS)-normalized REE distribution patterns for the calcite cements in the cap dolostone display an overall slightly LREE depletion ($\text{Pr}_{\text{SN}}/\text{Yb}_{\text{SN}} = 0.3$ to 3.0), positive La and Gd anomalies ($\text{Gd}/\text{Gd}^* = 1.10\text{--}1.96$) and negative Ce anomalies, and high Y/Ho ratios (most of which are >44 with an average of 50), which are typical of precipitation from normal marine seawater. Y and Ho have the same charge and similar ionic radius, with the latter removed from seawater much faster than the former because of differential complexation behaviour (Nozaki *et al.* 1997). This explains why the calcite has high Y/Ho ratios. Ce is present as Ce(IV) in oxygenated environments that can be readily incorporated into Fe-oxyhydroxides (Derry & Jacobsen, 1990), resulting in a negative Ce anomaly in marine precipitate. As such, Ce anomalies can be used to infer the seawater redox state; a negative Ce anomaly indicates an oxygenated oceanic condition, whereas a positive Ce anomaly reflects an anoxic depositional environment (Hu *et al.* 2014; Franchi *et al.* 2015). The uniform negative Ce anomalies in our calcites are consistent with an oxygenated oceanic condition.

Insofar as barite is cogenetic with dolomite, calcite, pyrite/Fe-oxide and quartz in the basal Doushantuo Formation at the Jiulongwan section, a seawater origin also receives support from Ba-isotopes of barite (BaSO_4) in the Jiulongwan and other basal cap dolostone sections in South China (Crockford *et al.* 2019), which have nearly invariable isotope compositions of $\leq 0.1\text{‰}$ that are within the range of modern pelagic barite and barites in worldwide Marinoan cap dolostones. This is in sharp contrast to modern cold-seep barites, which have variable Ba-isotope compositions of $\leq 0.9\text{‰}$ (Crockford *et al.* 2019). Whereas the Ba-isotopes suggest a

well-mixed residual snowball brine for the source of Ba, $\Delta^{17}\text{O}$ anomalies of atmospheric origin recorded in the same barites suggest a runoff origin for the sulfate. Redox reaction may have driven barite precipitation in the context of mixing of anoxic brine with meteoric ice meltwater (Bao *et al.* 2008; Zhou *et al.* 2010).

On the other hand, REE patterns with positive Eu and negative Ce anomalies are suggestive of mixing of hydrothermal solutions with seawater at unknown dilution ratios (Franchi *et al.* 2015). Hydrothermal solutions are commonly enriched in LREEs and Eu because of breakdown of plagioclase; thus hydrothermal influence tends to induce LREE enrichment and positive Eu anomalies (e.g. Michard, 1989; Van Kranendonk *et al.* 2003). Almost half of our REE analyses show positive Eu and negative Ce anomalies, which, coupled with less distinctive LREE depletion patterns, can be interpreted to have resulted from a hydrothermal overprint. A hydrothermal overprint on the seawater composition is also demonstrated by the non-linear correlation between Y/Ho and La in our calcite cements, which are characterized by La excess (c.f. Kamber & Webb, 2001; Franchi *et al.* 2015), and commonly high Mn contents (7500–15 000 ppm) that are frequently recorded in typical hydrothermal calcite (Kalliomäki *et al.* 2019).

A hydrothermal influence also receives support from clumped isotope (Δ_{47}) analyses of calcite, fluid inclusion analyses of quartz cements and alteration of trioctahedral clays into chlorite (Bristow *et al.* 2011; Derkowski *et al.* 2013; Zhou *et al.* 2017). On the basis of clumped isotope (Δ_{47}) analyses, Bristow *et al.* (2011) found these calcite cements formed under a high-temperature regime ($T > 400^\circ\text{C}$) and thus interpreted them as thermogenic methane oxidation products by means of hydrothermal activity during early Ediacaran or even Cambrian time (Bristow *et al.* 2011). Meanwhile, fluid inclusion analyses in quartz cements produced homogenization temperatures of c. $160\text{--}220^\circ\text{C}$ with both high salinity (18.0–20.8 wt % NaCl equiv.) and low-salinity (6.3–8.3 wt % NaCl equiv.) end-members, which are suggestive of mixing of high- and low-salinity hydrothermal fluids (Zhou *et al.* 2017). Alteration of saponite into chlorite via corrensinite increased from lower in Member 2 to the cap dolostone, which is commensurate with a decrease of $\delta^{18}\text{O}$ and increase of

δD in trioctahedral clays and is interpreted to have resulted from hydrothermal fluid activity in the underlying Nantuo Formation and cap dolostone (Derkowski *et al.* 2013).

Petrographic observations allow identification of three sequences of depositional/cementation events. Dolomite was first precipitated, followed by the formation of calcite cements/minerals, pyrite/iron oxide and barite, which subsequently experienced quartz cementation (Figs 3, 4). Note that barite only occasionally occurs as finer microscopic grains in association with calcite and dolomite in our samples, whereas abundant macroscopic barite coating dolomites is present at shallow-platform facies sections in South China and NW Africa (Shields *et al.* 2007; Zhou *et al.* 2010). Such mineral assemblages could suggest multiple stages of cavity/crack filling in response to a complicated interplay between eustasy and isostatic rebound and hydrothermal solutions (Shields *et al.* 2007; Zhou *et al.* 2010, 2017). Dolomite was initially precipitated during glacier retreat and relative sea-level changes, and was subsequently uplifted and exposed as a result of isostatic rebound. This prompted the dolomite to experience a period of karstic dissolution followed by sequential calcite/pyrite/iron oxide/barite precipitation and quartz cementation. The wide occurrence of quartz cementation may suggest precipitation from silica-rich hydrothermal fluids (Zhou *et al.* 2017), which was compounded by intense silicate weathering of glacial loess during the Marinoan Snowball Earth deglaciation (Penman & Rooney, 2019).

How long calcite precipitation postdates the initial deposition of dolomite remains unclear. Gan *et al.* (2021) documented a LA-ICP-MS U–Pb age of 632 ± 17 Ma from the isopachous dolomite within the cap dolostone, which we recalculate as $629.3 \pm 16.7/22.9$ Ma, using IsoplotR to directly compare with our own date. This published date is within uncertainty consistent with the calcite U–Pb age of 636.5 ± 17.8 Ma in this study. Despite relatively large analytical uncertainties, these U–Pb ages deny a broad time interval between the dolomite and calcite precipitation, which means the latter should have been influenced by hydrothermal fluids associated with the early Ediacaran but not Cambrian volcanism, as previously assumed (Bristow *et al.* 2011). Derkowski *et al.* (2013) reported illite K–Ar ages of *c.* 430 Ma from Member 4 shale and *c.* 325 Ma from Member 2 K-bentonite at the Jiuqunao section, which is *c.* 25 km from the Jiulongwan section. These dates are best explained as Ar diffusion due to the effect of resetting of the K–Ar isotope system at 430–325 Ma. Instead, these earliest periods of calcite cementation possibly ascribe to early stage fluid activities in response to eustasy and isostatic rebound not exceeding 1.6 Myrs (Shields *et al.* 2007; Zhou *et al.* 2010), which was subsequently overprinted by *c.* 632 Ma hydrothermal fluid activity (Bristow *et al.* 2011).

Cui *et al.* (2019) specifically measured the C-isotope data of calcite cements within the basal cap dolostone, which reveals low $\delta^{13}\text{C}_{\text{carb}}$ values (down to -53.8 ‰) in multiple generations of vug-filling calcite cement surrounding the pre-existing dolomite crystals with positive $\delta^{13}\text{C}_{\text{carb}}$ values as high as $+6.3$ ‰. Such isotopic signatures occur in multiple sections in South China, including the Jiulongwan section from which samples were collected in this study. The commonly low $\delta^{13}\text{C}_{\text{carb}}$ values mean these calcite cements should have a common origin, i.e. precipitation in early Ediacaran seawater and subsequently overprinted by early Ediacaran, but not late Ediacaran or Cambrian, hydrothermal activity. These calcite cements should have formed within <3 Myr considering the interbedded tuff zircon TIMS U–Pb ages of *c.* 635 Ma and *c.* 632 Ma within the basal and lower cap dolostone.

Such a time interval can be negligible considering the analytical errors (*c.* 7 Myr) of our calcite U–Pb age.

In this regard, both anoxic oxidation of methane (Shields *et al.* 2007; Zhou *et al.* 2010) and thermogenic methane oxidation (Bristow *et al.* 2011; Zhou *et al.* 2017) could have occurred to account for the calcite + pyrite + barite + iron oxide assemblage and particularly anomalously negative $\delta^{13}\text{C}_{\text{carb}}$ values recorded in the cap dolostone. In the former case, precipitation of calcite with extremely negative $^{13}\text{C}_{\text{carb}}$ values would be nearly synchronous with deposition of cap dolostone, which means deglaciation was related to methane release into the atmosphere by means of destabilization of clathrates (Jiang *et al.* 2003; Kennedy *et al.* 2008; Wang *et al.* 2008). In the latter case, precipitation of calcite with extremely negative $^{13}\text{C}_{\text{carb}}$ values should postdate the initial deposition of cap dolostone to a time interval of *c.* 3 Myr, which means thermogenic methane oxidation would have occurred much later in the cap dolostone. In this scenario, deglaciation would be unrelated to methane release into the atmosphere by means of destabilization of clathrates (Shields *et al.* 2007; Zhou *et al.* 2010).

5.b. Reliability of calcite U–Pb geochronology for Precambrian application

A published tuff zircon TIMS U–Pb age from the lower cap carbonate of the Doushantuo Formation provides a direct test of our calcite laser U–Pb age. A tuff bed *c.* 230 cm above the base of the cap carbonate of the Doushantuo Formation yielded a zircon TIMS U–Pb age of 635.23 ± 0.57 Ma (MSWD = 0.55) (Condon *et al.* 2005). Our results from the sampling horizon, which is *c.* 130 cm from the dated tuff bed, produce a calcite U–Pb age of 636.5 ± 17.8 Ma. These ages overlap within uncertainty, with only a 0.2 % offset, indicating that the calcite U–Pb age is a robust estimate of the timing of sedimentation within the quoted analytical uncertainty. Also, our calcite U–Pb age of 636.5 ± 17.8 Ma is within uncertainty of the dolomite U–Pb age of 632 ± 17 Ma (Gan *et al.* 2021), again indicating its robustness for age estimation. LA-ICP-MS U–Pb dating of carbonates has been applied to material with ages ranging from the Mesoproterozoic to Quaternary, but mostly to the Mesozoic to Cenozoic (see Roberts *et al.* 2020). Because of high ratios of common to radiogenic lead, most older dates reported from Precambrian to Cambrian carbonates (Liivamägi *et al.* 2018, 2021; Meinhold *et al.* 2020) are rather imprecise (e.g. 5–12 % uncertainties 2σ). Along with the dolomite U–Pb age of 632 ± 17 Ma reported by Gan *et al.* (2021), and the recently reported 1010 ± 36 Ma age from an older sedimentary sequence in South China (Lan *et al.* 2022), our result is one of the most precise Precambrian dates obtained so far using the LA-ICP-MS method for U–Pb carbonate geochronology. These studies highlight the practicality of the LA-ICP-MS method and demonstrate the advantages of using an *in situ* technique, which namely, are the ability to make use of the heterogeneous distribution of U and Pb within calcite, in the measurement of a large spread in U–Pb ratios from a single sample along with the avoidance of altered or mixed domains (Roberts *et al.* 2020). These advantages are difficult to achieve with dissolution and dilution-based methods owing to the averaging effect of coarser sampling. The success of this study gives us confidence that reliable U–Pb carbonate ages for other Precambrian successions can be obtained. Given that Precambrian carbonate rocks contain key information regarding the coevolution of life and environment, laser ablation U–Pb dating of carbonate minerals has great potential for providing important age constraints on biological and

environmental events such as the Great Oxygenation Event and the Bitter Springs Anomaly.

6. Summary and conclusions

Based on an integrated calcite LA-ICP-MS U–Pb dating and REE measurement combined with SEM and CL imaging analyses, the following conclusions can be drawn:

- (1) Calcite cements widely occur as irregular cavity/crack fillings in the cap dolostone of the Doushantuo Formation at the Jiulongwan section, South China, where they co-occur with pyrite, iron oxide and barite.
- (2) Petrographic observations show calcite (including cements and single finer grains) and pyrite postdate the initial deposition of dolomite but pre-date quartz cements. Some calcite cements show a bright orange CL colour, probably indicating hydrothermal overprint.
- (3) Calcites show positive La and Gd anomalies ($\delta\text{Gd} = 1.1\text{--}1.96$), a negative Ce anomaly, high Y/Ho ratios (39–61 with an average of 50) and slightly LREE depletion patterns. Some samples show positive Eu anomalies ($\delta\text{Eu} = 1.02\text{--}1.38$), whereas others show slightly negative Eu anomalies ($\delta\text{Eu} = 0.79\text{--}0.96$). Such REE distribution patterns suggest a dominant seawater origin with subsequent hydrothermal overprints.
- (4) Calcite cements within the cap dolostone give a U–Pb age of $636.5 \pm 7.4/17.8$ Ma (2σ , MSWD = 1.6, $n = 36/40$), which is within uncertainty of a previous dolomite U–Pb age of $629.3 \pm 16.7/22.9$ Ma. These ages suggest Cambrian hydrothermal activity could not have been responsible for the formation of these calcite cements. Instead, they were probably formed during the early Ediacaran period via oxidation of methane clathrates or thermogenic methane oxidation.
- (5) Petrographic, geochronological and geochemical data point to early Ediacaran oxidation of methane clathrates in response to complex interactions between eustasy and isostatic rebound and hydrothermal solutions.

Supplementary material. To view supplementary material for this article, please visit <https://doi.org/10.1017/S001675682200019X>

Acknowledgements. Paul Hoffman and an anonymous reviewer are appreciated for reviewing this manuscript and giving constructive comments. This project was funded by the National Science Foundation of China (grant 41673016 to ZWL), State Key Laboratory of Lithospheric Evolution, Institute of Geology and Geophysics, Chinese Academy of Sciences (grant SKL-Z202001 to ZWL), State Key Laboratory of Palaeobiology and Stratigraphy, Nanjing Institute of Geology and Palaeontology, Chinese Academy of Sciences (grant 193112 to ZWL), and State Key Laboratory of Geological Processes and Mineral Resources, China University of Geosciences (grant GPMR201902 to ZWL).

References

- Baker JA, Peate DW, Waight T and Meyzen C (2004) Pb isotopic analysis of standards and samples using a ^{207}Pb – ^{204}Pb double spike and thallium to correct for mass bias with a double-focusing MC-ICP-MS. *Chemical Geology* **211**, 275–303.
- Bao HM, Lyons JR and Zhou C (2008) Triple oxygen isotope evidence for elevated CO_2 levels after a Neoproterozoic glaciation. *Nature* **453**, 504–6.
- Bristow TF, Bonifacie M, Derkowski A, Eiler JM and Grotzinger JP (2011) A hydrothermal origin for isotopically anomalous cap dolostone cements from south China. *Nature* **474**, 68–71.
- Chew DM, Petrus JA and Kamber BS (2014) U–Pb LA-ICPMS dating using accessory mineral standards with variable common Pb. *Chemical Geology* **363**, 185–99.
- Condon D, Zhu MY, Bowring S, Wang W, Yang AH and Jin YG (2005) U–Pb ages from the Neoproterozoic Doushantuo Formation, China. *Science* **308**, 95–8.
- Coogan LA, Parrish RR and Roberts NM (2016) Early hydrothermal carbon uptake by the upper oceanic crust: insight from in situ U–Pb dating. *Geology* **44**, 147–50.
- Crockford PW, Wing BA, Paytan A, Hodgskiss MSW, Mayfield KK, Hayles JA, Middleton JE, Ahm ASC, Johnston DT, Caxito F, Uhlein G, Halverson GP, Eickmann B, Torres M and Horner TJ (2019) Barium-isotopic constraints on the origin of post-Marinoan barites. *Earth and Planetary Science Letters* **519**, 234–44.
- Cui H, Orland IJ, Denny A, Kitajima K, Fournelle JH, Baele JM, De Winter NJ, Goderis S, Claeys P and Valley JW (2019) Ice or fire? Constraining the origin of isotopically anomalous cap carbonate cements by SIMS. *Geological Society of America Abstracts with Programs* **51**. doi: [10.1130/abs/2019AM-332456](https://doi.org/10.1130/abs/2019AM-332456).
- Derkowski A, Bristow TF, Wampler JM, Sřodoń J, Marynowski L, Elliott WC and Chamberlain CP (2013) Hydrothermal alteration of the Ediacaran Doushantuo Formation in the Yangtze Gorges area (South China). *Geochimica et Cosmochimica Acta* **107**, 279–98.
- Derry LA and Jacobsen SB (1990) The chemical evolution of Precambrian seawater: evidence from REEs in banded iron formations. *Geochimica et Cosmochimica Acta* **54**, 2965–77.
- Franchi F, Hofmann A, Cavalazzi B, Wilson A and Barbieri R (2015) Differentiating marine vs hydrothermal processes in Devonian carbonate mounds using rare earth elements (Kess Kess mounds, Anti-Atlas, Morocco). *Chemical Geology* **409**, 69–86.
- Gan T, Luo TY, Pang K, Zhou CM, Zhou GH, Wan B, Li G, Yi QR, Czaja AD and Xiao SH (2021) Cryptic terrestrial fungus-like fossils of the early Ediacaran Period. *Nature Communications* **12**, 641. doi: [10.1038/s41467-021-20975-1](https://doi.org/10.1038/s41467-021-20975-1).
- Griffin W, Powell W, Pearson NJ and O'Reilly S (2008) GLITTER: data reduction software for laser ablation ICP-MS. In *Laser Ablation-ICP-MS in the Earth Sciences: Current Practices and Outstanding Issues* (ed. P Sylvester), pp. 308–11. Mineralogical Association of Canada. Short Course Vol. 40.
- Hill CA, Polyak VJ, Asmerom Y and Provencio P (2016) Constraints on a Late Cretaceous uplift, denudation, and incision of the Grand Canyon region, southwestern Colorado Plateau, USA, from U–Pb dating of lacustrine limestone. *Tectonics* **35**, 896–906.
- Hoffman PF and Schrag DP (2002) The snowball Earth hypothesis: testing the limits of global change. *Terra Nova* **14**, 129–55.
- Hoffman PF and Macdonald FA (2010) Sheet-crack cements and early regression in Marinoan (635 Ma) cap dolostones: regional benchmarks of vanishing ice-sheets? *Earth and Planetary Science Letters* **300**, 374–84.
- Horstwood MSA, Kosler J, Gehrels G, Jackson SE, McLean NM, Paton C, Pearson NJ, Sircombe K, Sylvester P, Vermmesch P, Bowring JF, Condon DJ and Schoene B (2016) Community-derived standards for LA-ICP-MS U–(Th)–Pb geochronology–uncertainty propagation, age interpretation and data reporting. *Geostandards and Geoanalytical Research* **40**, 311–22.
- Hu Y, Feng D, Peckmann J, Roberts HH and Chen D (2014) New insights into cerium anomalies and mechanisms of trace metal enrichment in authigenic carbonate from hydrocarbon seeps. *Chemical Geology* **381**, 55–66.
- Jiang GQ, Kaufman AJ, Christie-Blick N, Zhang S and Wu H (2007) Carbon isotope variability across the Ediacaran Yangtze platform in South China: implications for a large surface-to-deep ocean $\delta^{13}\text{C}$ gradient. *Earth and Planetary Science Letters* **261**, 303–20.
- Jiang GQ, Kennedy MJ and Christie-Blick N (2003) Stable isotopic evidence for methane seeps in Neoproterozoic postglacial cap carbonates. *Nature* **426**, 822–6.
- Jiang GQ, Kennedy MJ, Christie-Blick N, Wu HC and Zhang SH (2006) Stratigraphy, sedimentary structures, and textures of the late Neoproterozoic Doushantuo cap carbonate in south China. *Journal of Sedimentary Research* **76**, 978–95.

- Jiang GQ, Shi XY, Zhang SH, Wang Y and Xiao SH (2011) Stratigraphy and paleogeography of the Ediacaran Doushantuo Formation (ca. 635–551 Ma) in South China. *Gondwana Research* **19**, 831–49.
- Kalliomäki H, Wagner T, Fusswinkel T and Schultze D (2019) Textural evolution and trace element chemistry of hydrothermal calcites from Archean gold deposits in the Hattu schist belt, eastern Finland: indicators of the ore-forming environment. *Ore Geology Reviews* **112**, 103006. doi: [10.1016/j.oregeorev.2019.103006](https://doi.org/10.1016/j.oregeorev.2019.103006).
- Kamber BS and Webb GE (2001) The geochemistry of Late Archaean microbial carbonate: implications for ocean chemistry and continental erosion history. *Geochimica et Cosmochimica Acta* **65**, 2509–25.
- Kennedy MJ, Christie-Blick N and Sohl LE (2001) Are Proterozoic cap carbonates and isotopic excursions a record of gas hydrate destabilization following Earth's coldest intervals? *Geology* **29**, 443–6.
- Kennedy M, Mrofka D and von der Borch C (2008) Snowball Earth termination by destabilization of equatorial permafrost methane clathrate. *Nature* **453**, 642–5.
- Ku TL, Knauss KG and Mathieu GG (1977) Uranium in open ocean: concentration and isotopic composition. *Deep Sea Research* **24**, 1005–17.
- Lan ZW, Roberts NMW, Zhou Y, Zhang SJ, Li ZS and Zhao TP (2022) Application of *in situ* U–Pb carbonate geochronology to Stenian-Tonian successions of North China. *Precambrian Research* **370**, 106551. doi: [10.1016/j.precamres.2021.106551](https://doi.org/10.1016/j.precamres.2021.106551).
- Lan ZW, Sano Y, Yahagi T, Tanaka K, Shirai K, Papineau D, Sawaki Y, Ohno T, Abe M, Yang HW, Liu H, Jiang T and Wang T (2019) An integrated chemostratigraphic ($\delta^{13}\text{C}$ – $\delta^{18}\text{O}$ – $^{87}\text{Sr}/^{86}\text{Sr}$ – $\delta^{15}\text{N}$) study of the Doushantuo Formation in western Hubei Province, South China. *Precambrian Research* **320**, 232–52.
- Lang XG, Chen JT, Cui H, Man L, Huang KJ, Fu Y, Zhou CM and Shen B (2018) Cyclic cold climate during the Nantuo Glaciation: evidence from the Cryogenian Nantuo Formation in the Yangtze Block, South China. *Precambrian Research* **310**, 243–55.
- Li XH, Li WX, Li ZX, Lo CH, Wang J, Ye MF and Yang YH (2009) Amalgamation between the Yangtze and Cathaysia Blocks in South China: constraints from SHRIMP U–Pb zircon ages, geochemistry and Nd–Hf isotopes of the Shuangxiwu volcanic rocks. *Precambrian Research* **174**, 117–28.
- Li Q, Parrish RR, Horstwood MSA and McArthur JM (2014) U–Pb dating of cements in Mesozoic ammonites. *Chemical Geology* **376**, 76–83.
- Liivamägi S, Šrodoň J, Bojanowski MJ, Gerdes A, Stanek JJ, Williams I and Szczerba M (2018) Paleosols on the Ediacaran basalts of the East European Craton: a unique record of paleoweathering with minimum diagenetic overprint. *Precambrian Research* **316**, 66–82.
- Liivamägi S, Šrodoň J, Bojanowski MJ, Stanek JJ and Roberts NMW (2021) Precambrian paleosols on the Great Unconformity of the East European Craton: an 800 million year record of Baltica's climate conditions. *Precambrian Research* **363**, 106327. doi: [10.1016/j.precamres.2021.106327](https://doi.org/10.1016/j.precamres.2021.106327).
- MacDonald JM, Faithfull JW, Roberts NMW, Davies AJ, Holdsworth CM, Newton M, Williamson S, Boyce A and John CM (2019) Clumped-isotope palaeothermometry and LA-ICPMS U–Pb dating of lava-pile hydrothermal calcite veins. *Contributions to Mineralogy and Petrology* **174**. doi: [10.1007/s00410-019-1599-x](https://doi.org/10.1007/s00410-019-1599-x).
- Meinhold G, Roberts NMW, Arslan A, Jensen S, Ebbestad JOR, Högström AES, Høyberget M, Agić H, Palacios T and Taylor WL (2020) U–Pb dating of calcite in ancient carbonates for age estimates of syn- to post-depositional processes: a case study from the upper Ediacaran strata of Finnmark, Arctic Norway. *Geological Magazine* **157**, 1367–72.
- Michard A (1989) Rare earth element systematics in hydrothermal fluids. *Geochimica et Cosmochimica Acta* **53**, 745–50.
- Nozaki Y, Zhang J and Amakawa H (1997) The fractionation between Y and Ho in the marine environment. *Earth and Planetary Science Letters* **148**, 329–40.
- Nuriel P, Weinberger R, Kylander-Clark ARC, Hacker BR and Craddock JP (2017) The onset of the Dead Sea transform based on calcite age-strain analyses. *Geology* **45**, 587–90.
- Paton C, Hellstrom J, Paul B, Woodhead J and Hergt J (2011) Iolite: freeware for the visualisation and processing of mass spectrometric data. *Journal of Analytical Atomic Spectrometry* **26**, 2508–18.
- Penman DE and Rooney AD (2019) Coupled carbon and silica cycle perturbations during the Marinoan snowball Earth deglaciation. *Geology* **47**, 317–20.
- Petrus JA and Kamber BS (2012) VizualAge: a novel approach to laser ablation ICP-MS U–Pb geochronology data reduction. *Geostandards and Geoanalytical Research* **36**, 247–70.
- Rasbury ET and Cole JM (2009) Directly dating geologic events: U–Pb dating of carbonates. *Review of Geophysics* **47**, 1–27.
- Rasbury ET, Ward WB, Hemming NG, Li H, Dickson JD, Hanson GN and Major RP (2004) Concurrent U–Pb age and seawater $^{87}\text{Sr}/^{86}\text{Sr}$ value of a marine cement. *Earth and Planetary Science Letters* **221**, 355–71.
- Ring U and Gerdes A (2016) Kinematics of the Alpenrhein-Bodensee graben system in the Central Alps: Oligocene/Miocene trans-tension due to formation of the Western Alps arc. *Tectonics* **35**, 1367–91.
- Roberts NMW, Drost K, Horstwood MS, Condon DJ, Chew D, Drake H, Milodowski AE, McLean NM, Smye AJ, Walker RJ and Haslam R (2020) Laser ablation inductively coupled plasma mass spectrometry (LA-ICP-MS) U–Pb carbonate geochronology: strategies, progress, and limitations. *Geochronology* **2**, 33–61.
- Roberts NMW, Rasbury ET, Parrish RR, Smith CJ, Horstwood MSA and Condon DJ (2017) A calcite reference material for LA-ICP-MS U–Pb geochronology. *Geochemistry, Geophysics, Geosystem* **18**, 2807–14.
- Roberts NMW and Walker RJ (2016) U–Pb geochronology of calcite-mineralized faults: absolute timing of rift-related fault events on the northeast Atlantic margin. *Geology* **44**, 531–4.
- Shen GT and Boyle EA (1987) Lead in corals: reconstruction of historical industrial fluxes to the surface ocean. *Earth and Planetary Science Letters* **82**, 289–304.
- Shields GA, Deynoux M, Strauss H, Paquet H and Nahon D (2007) Barite-bearing cap dolostones of the Taoudeni Basin, northwest Africa; sedimentary and isotopic evidence for methane seepage after a Neoproterozoic glaciation. *Precambrian Research* **153**, 209–35.
- Van Kranendonk MJ, Webb GE and Kamber BS (2003) Geological and trace element evidence for a marine sedimentary environment of deposition and biogenicity of 3.45 Ga stromatolitic carbonates in the Pilbara Craton, and support for a reducing Archaean ocean. *Geobiology* **1**, 91–108.
- Vermeech P (2018) IsoplotR: a free and open toolbox for geochronology. *Geoscience Frontiers* **9**, 1479–93.
- Wang JS, Jiang GQ, Xiao SH, Li Q and Wei Q (2008) Carbon isotope evidence for widespread methane seeps in the ca. 635 Ma Doushantuo cap carbonate in south China. *Geology* **36**, 347–50.
- Wang J and Li ZX (2003) History of Neoproterozoic rift basins in South China: implications for Rodinia break-up. *Precambrian Research* **122**, 141–58.
- Woodhead JD and Hergt JM (2001) Strontium, neodymium and lead isotope analyses of NIST glass certified reference materials: SRM 610, 612, 614. *Geostandards Newsletters* **25**, 261–6.
- Wu S, Karius V, Schmidt BC, Simon K and Woerner G (2018) Comparison of ultrafine powder pellet and flux-free fusion glass for bulk analysis of granitoids by laser ablation-inductively coupled plasma-mass spectrometry. *Geostandards and Geoanalytical Research* **42**, 575–91.
- Wu S, Worner G, Jochum KP, Stoll B, Simon K and Kronz A (2019) The preparation and preliminary characterisation of three synthetic andesite reference glass materials (ARM-1, ARM-2, ARM-3) for in situ microanalysis. *Geostandards and Geoanalytical Research* **43**, 567–84.
- Wu ST, Yang YH, Jochum KP, Romer RL, Glodny J, Savov IP, Agostini S, De Hoog JCM, Peters STM, Kronz A, Zhang C, Bao ZA, Wang XJ, Li YL, Tang GQ, Feng LJ, Yu HM, Li ZX, Zhang L, Lin J, Zeng Y, Xu CX, Wang YP, Cui Z, Deng L, Xiao J, Liu YH, Xue DS, Zhang D, Jia LH, Wang H, Xu L, Huang C, Xie LW, Pack A, Woerner G, He MY, Li CF, Yuan HL, Huang F, Li QL, Yang JH, Li XH and Wu FY (2021) Isotopic compositions (Li–B–Si–O–Mg–Sr–Nd–Hf–Pb) and $\text{Fe}^{2+}/\Sigma\text{Fe}$ ratios of three synthetic andesite glass reference materials (ARM-1, ARM-2, ARM-3). *Geostandards and Geoanalytical Research* **45**, 719–45.
- Wu ST, Yang YH, Wang H, Huang C, Xie LW and Yang JH (2020a) Characteristic performance of guard electrode in LA-SF-ICP-MS for multi-element quantification. *Atomic Spectroscopy* **41**, 154–61.
- Wu ST, Yang M, Yang YH, Xie LW, Huang C, Wang H and Yang JH (2020b) Improved *in situ* zircon U–Pb dating at high spatial resolution (5–16 μm) by

- laser ablation–single collector–sector field–ICP–MS using Jet sample and X skimmer cones. *International Journal of Mass Spectrometry* **456**, 116394. doi: [10.1016/j.ijms.2020.116394](https://doi.org/10.1016/j.ijms.2020.116394).
- Wu ST, Yang YH, Roberts NMW, Yang M, Wang H, Lan ZW, Xie BH, Li TY, Xu L, Huang C, Xie LW, Yang JH and Wu FY** (2022) In situ calcite U–Pb geochronology by high-sensitivity single-collector LA-SF-ICP-MS. *Science China Earth Sciences*, doi: [10.1007/s11430-021-9907-1](https://doi.org/10.1007/s11430-021-9907-1).
- Yang C, Rooney AD, Condon DJ, Li XH, Grazhdankin DV, Bowyer FT, Hu CL, Macdonald FA and Zhu MY** (2021) The tempo of Ediacaran evolution. *Science Advances* **7**, eabi9643. doi: [10.1126/sciadv.abi9643](https://doi.org/10.1126/sciadv.abi9643).
- Zhou CM, Bao HM, Peng YB and Yuan XL** (2010) Timing the deposition of ¹⁷O-depleted barite at the aftermath of Nantuo glacial meltdown in South China. *Geology* **38**, 903–6.
- Zhou GH, Luo TY, Zhou MZ, Xing LC and Gan T** (2017) A ubiquitous hydrothermal episode recorded in the sheet-crack cements of a Marinoan cap dolostone of South China: implication for the origin of the extremely ¹³C-depleted calcite cement. *Journal of Asian Earth Sciences* **134**, 63–71.



Application of *in situ* U-Pb carbonate geochronology to Stenian-Tonian successions of North China

Zhongwu Lan^{a,b,c,*}, Nick M.W. Roberts^d, Ying Zhou^e, Shujing Zhang^f, Zhensheng Li^g, Taiping Zhao^h

^a State Key Laboratory of Lithospheric Evolution, Institute of Geology and Geophysics, Chinese Academy of Sciences, Beijing 100029, China

^b State Key Laboratory of Palaeobiology and Stratigraphy, Nanjing Institute of Geology and Palaeontology, Chinese Academy of Science, Nanjing 210008, Jiangsu, China

^c State Key Laboratory of Geological Processes and Mineral Resources, China University of Geosciences, Wuhan 430074, Hubei, China

^d Geochronology and Tracers Facility, British Geological Survey, Keyworth NG12 5GG, UK

^e Department of Earth Sciences, University College London, London WC1E 6BT, UK

^f Ireland Department of Geology, School of Natural Sciences, Trinity College Dublin, Dublin 2, Ireland

^g School of Resources and Environmental Engineering, Hefei University of Technology, Anhui 230009, China

^h Key Laboratory of Mineralogy and Metallogeny, Guangzhou Institute of Geochemistry, Chinese Academy of Sciences, Guangzhou 510640, China

ARTICLE INFO

Keywords:

Carbonates

U-Pb geochronology

North China Craton

Stenian-Tonian

ABSTRACT

Linking geological and biological events requires a robust geochronologic framework, which is especially challenging for poorly fossiliferous Precambrian strata. Although this can be achieved through zircon U-Pb dating, only maximum or minimum ages can typically be obtained, with rare interbedded volcanic ash beds providing precise depositional ages. U-Pb dating of authigenic carbonates could potentially become a more widely applicable geochronometer, but only if carbonate minerals can be dated with sufficient precision. A renaissance in carbonate U-Pb geochronology, utilizing the *in situ* laser ablation method, has opened new doors in the application of this method to geological problems. Here we apply laser ablation U-Pb dating to carbonate-rich sedimentary strata of likely Meso-Neoproterozoic age on the southeastern margin of the North China Craton, resulting in two meaningful U-Pb ages of 1036 ± 45 Ma and 1010 ± 36 Ma (2σ), from early diagenetic fine-grained microspar samples. As well as being mutually consistent, these new ages show that precision approaching the limiting uncertainty of the reference material used ($\sim 2.5\%$ 2σ) can be achieved. Success in this study holds promise for dating other key Precambrian successions.

1. Introduction

As common sedimentary rocks on Earth, carbonate rocks host a wealth of vital information linking processes that involve the hydrosphere and atmosphere with biological evolution (Xiao et al., 2014; Tang et al., 2017; Zhou et al., 2020). The linking of these geological and biological events through strata is highly dependent on precise geochronological constraints on key stratigraphic horizons; however, this has proven difficult for many sedimentary successions that lack age-diagnostic fossil assemblages, i.e. much of the Precambrian, and that lack interbedded or cross-cutting igneous units containing co-magmatic zircon or baddeleyite crystals. Further issues for the dating of Precambrian successions are diagenetic alteration and the frequent hydrothermal or metamorphic overprint.

Zircon U-Pb dating from interbedded volcanic tuffs is the most robust method to constrain the depositional age of sedimentary rocks beyond the Phanerozoic (e.g. Condon and Bowring, 2011). In the absence of interbedded tuffs, Pb-Pb, Rb-Sr, Sm-Nd, Re-Os and K-Ar/Ar-Ar systems of whole rock or diagenetic minerals are also applicable methods, although obtaining accurate and precise ages of deposition can be highly problematic (e.g. Rasmussen, 2005; Condon and Bowring, 2011). U-Pb geochronology of carbonates was a method developed in the late 1980 s (Moorbath et al., 1987; Jahn, 1988), but also had significant limitations for providing precise primary ages of formation/deposition (e.g. Jahn and Cuvelier, 1994; Rasbury and Cole, 2009). More recently, the *in situ* technique, laser ablation inductively coupled plasma mass spectrometry (LA-ICP-MS), has been developed and shown to be of great promise for dating a wide range of carbonate occurrences (Li et al., 2014; Roberts

* Corresponding author.

E-mail address: lzw1981@126.com (Z. Lan).

<https://doi.org/10.1016/j.precamres.2021.106551>

Received 11 November 2021; Received in revised form 22 December 2021; Accepted 23 December 2021

0301-9268/© 2022 Elsevier B.V. All rights reserved.

et al., 2020). Although carbonate minerals incorporate large amounts of common Pb during their formation, the distribution of U and Pb during formation is typically heterogeneous, resulting in large variability in U/Pb ratios at the sub-millimeter scale (Roberts and Walker, 2016; Roberts et al., 2020); this large spread in U/Pb ratios can be exploited with the LA-ICP-MS method, potentially leading to robust U-Pb isochrons.

To demonstrate the applicability of this method to dating of Precambrian successions, and to further constrain the timing of biologically significant Meso- to Neoproterozoic strata, we present new LA-ICP-MS U-Pb carbonate geochronology from a late Mesoproterozoic to early Neoproterozoic sedimentary succession deposited on the North China Craton. The dated formations are from a suite of sedimentary strata that have clear chemostratigraphic and biostratigraphic constraints (Dong et al., 2008; Xiao et al., 2014; Tang et al., 2017; Zhou et al., 2020). The presence of the age-diagnostic fossil *Trachyhystrichosphaera aimika*, muted variability of $\delta^{13}\text{C}_{\text{carb}}$ values (-2.0‰ to $+5.0\text{‰}$), coupled with typically unradiogenic $^{87}\text{Sr}/^{86}\text{Sr}$ ratios (0.7052 to 0.7061) (Zhou et al., 2020), are typical of the global late Mesoproterozoic-early Neoproterozoic transitional interval (Halverson et al., 2010; Baludikay et al., 2016; Beghin et al., 2017; Silva-Tamayo et al., 2018) and ensure that our new calcite U-Pb ages can, using a well-established stratigraphic framework, be used to test the applicability of calcite U-Pb dating in the Precambrian carbonate rocks.

2. Geological setting and sampling horizons

The North China Craton (NCC) is separated from the South China Craton by the Qinling-Dabie orogenic belt (Fig. 1A; Lu et al., 2008). The NCC is also known as the Sino-Korean Craton that is composed of an Archean to Paleoproterozoic basement covered by Mesoproterozoic to Phanerozoic sedimentary successions with a total thickness of up to 9000 m (Lu et al., 2008). Platform carbonates are the dominant lithology over the NCC from the Mesoproterozoic to the Early Paleozoic (Yang et al., 2012), which is in accord with its paleolatitude in paleogeographic reconstructions (Fu et al., 2015). Mesoproterozoic to Neoproterozoic successions are well exposed in the Xu-Huai Aulacogen of the southeastern NCC (Fig. 1B-C; Lu et al., 2008), which comprises the Huaibei region in the north and Huainan region in the south. On the northern NCC, a suite of mixed carbonate and siliciclastic sedimentary successions are divided into the Changcheng Group (c.1700–1620 Ma), Jixian Group (c.1620–1440 Ma), Xiamaling Formation or Xishan Group (c.1370 Ma), and the transitional Meso- to Neoproterozoic Qingbaikou Group. These four groups have been widely adopted as a reference for stratigraphic correlation within China (Fig. 2A). In southeastern NCC, the Qingbaikou Group is composed of the Huaibei, Huainan and Feishui groups (Wang et al., 1984; Xiao et al., 2014; He et al., 2017; Wan et al., 2019).

Across the NCC, Mesoproterozoic to Neoproterozoic successions display a typical sequence of lithologies, with coarse siliciclastic sediments at the base succeeded by mudstone and then carbonate of variable

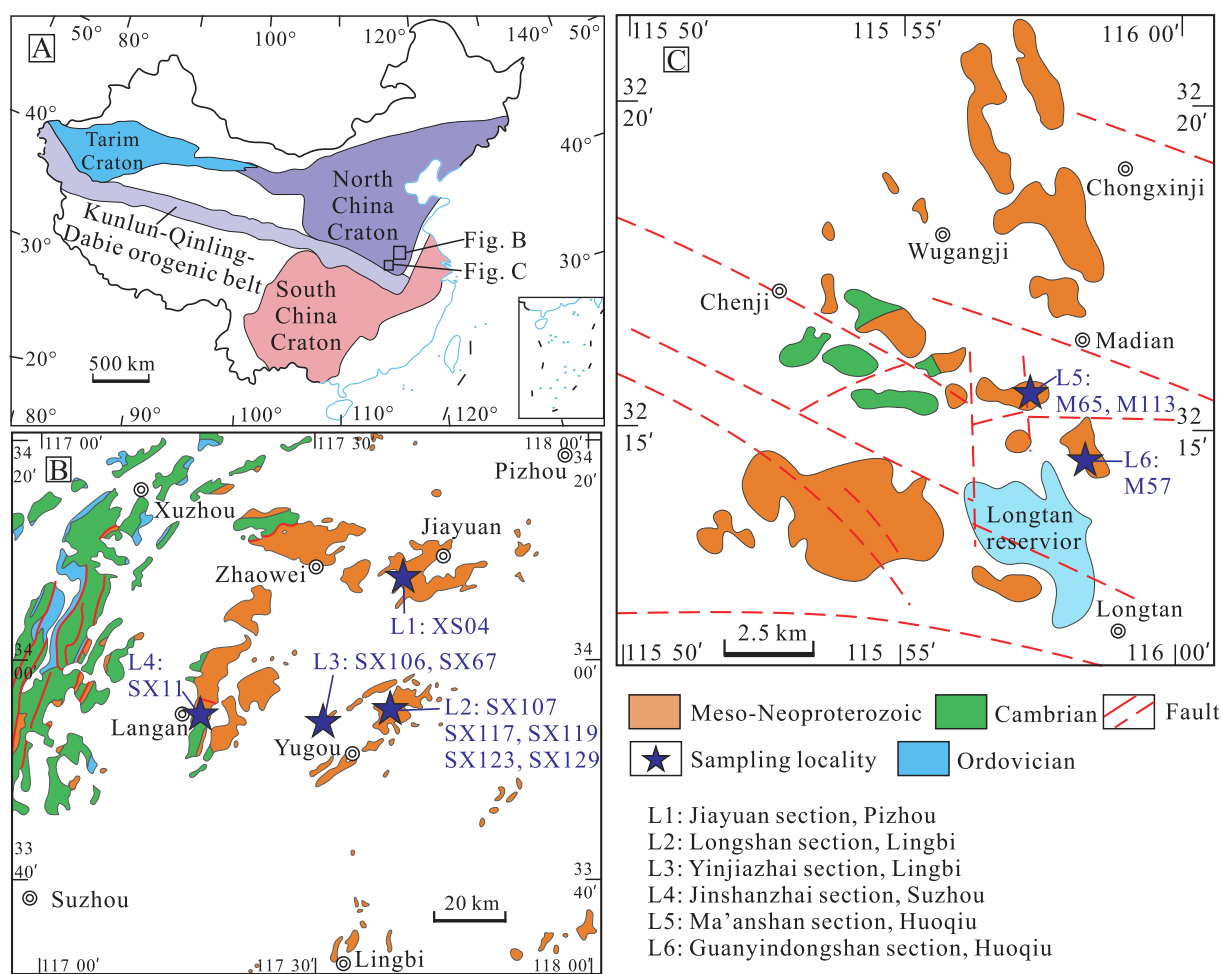


Fig. 1. (A) Simplified geological map showing the tectonic framework of China, comprising the North China Craton and South China Craton separated by the Kunlun-Qinling-Dabie Orogenic Belt. (B)-(C) Simplified geological map showing the sampling locations in the Huaibei and western Huainan regions of the southeastern margin of North China Craton, respectively.

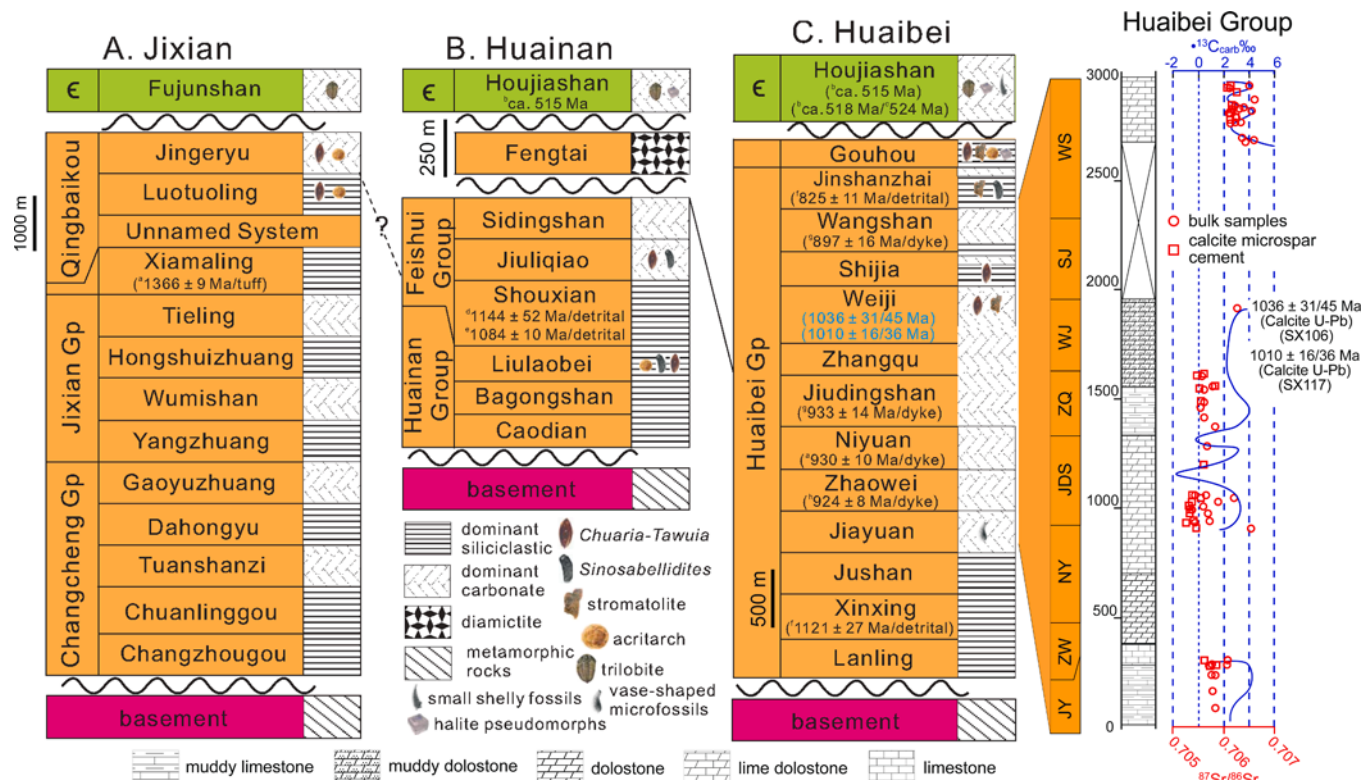


Fig. 2. Lithostratigraphy in the Huainan, Huaibei and Jixian regions. Age data source: a-Gao et al. (2009); b-He et al. (2017); c-Wan et al. (2019); d-Sun et al. (2020); e-Zhao et al. (2019); f-Yang et al. (2012); g-Wang et al. (2012); h-Liu et al. (2006); The blue-colored ages are calcite U-Pb age in this study. Carbon and strontium isotope data are from Zhou et al. (2020). The green and orange colors represent Cambrian and Precambrian strata, respectively.

thickness. Such a tripartite succession is overlain either by glaciogenic deposits of supposedly Ediacaran age (Zhou et al., 2019) and/or phosphatic and evaporitic carbonate-rich units of Cambrian age (He et al., 2017; Wan et al., 2019). Some Mesoproterozoic to Neoproterozoic carbonates and siliciclastic sedimentary rocks outcropping along the northern and southern margins of the NCC have a very low metamorphic grade, lower than prehnite–pumpellyite facies (Chu et al., 2007; Xiao et al., 2014; Zhou et al., 2020). Such a unique feature makes the NCC an ideal natural laboratory to trace the co-evolution of life and the physical environment during the Proterozoic Eon by means of biostratigraphic and chemostratigraphic studies such as $\delta^{13}\text{C}_{\text{carb}}$ and biomarker analyses (Chu et al., 2007; Xiao et al., 2014; Luo et al., 2014; Tang et al., 2015, 2017; Shang et al., 2019).

Late Mesoproterozoic to early Neoproterozoic successions, the Huaibei, Huainan and Feishui groups, assigned to the Qingbaikou Group, outcrop on the southeastern margin of the NCC. Of the three groups, the Huaibei Group is composed of thirteen lithostratigraphic units: the Lanling, Xinxing, Jushan, Jiayuan, Zhaowei, Niyuan, Jiudingshan, Zhangqu, Weiwei, Shijia, Wangshan, Jinshanzhai and Gouhou formations (Fig. 2C). The lower three formations, Lanling, Xinxing and Jushan, comprise siliciclastic rocks and are poorly exposed (Cao et al., 2001). The dominant lithology of the overlying 10 formations is carbonate, except for the Shijia Formation, which is composed of mostly light gray and reddish purple shale with interbeds of stromatolitic dolostone (Cao et al., 1985). The carbonate formations of the group, from the oldest to youngest, comprise the Jiayuan Formation, which is composed of ribbon dolostone interbedded with sandstone and more massive dolomitic limestone upwards; the Zhaowei Formation, which is more limestone-dominated with bioherms of intraclastic breccia and stromatolite; the Niyuan Formation, which comprises light gray dolostone with some ripple marks, indicating a very shallow depositional environment; the Jiudingshan Formation, which ranges from dolostone to limestone upwards with the appearance of early diagenetic calcite

microspar cement (CMS, Zhou et al., 2020), traditionally named Molar Tooth Structure; the Zhangqu Formation, which comprises dark muddy limestone with reddish clay partings, and abundant CMC and stromatolite; the Weiwei Formation, which has some light greenish shale at the base, stromatolitic limestone in its lower part, and reddish domal stromatolites dominating the top half of the formation; the Wangshan Formation, which has thinly bedded lime mudstone (marl) in its lower part and grey limestone with abundant CMC and stromatolite in the upper half; the Jinshanzhai Formation, which is very thin, ca. 20 m, composed of reddish shale and red small columnar stromatolite; and finally the Gouhou Formation, which comprises greenish shales and siltstones. The Huaibei Group is exposed in different isolated outcrops and so only by correlation can a complete succession be reconstructed.

Diabase dykes intruding the Zhaowei, Niyuan, Jiudingshan and Wangshan formations yielded *in situ* zircon $^{206}\text{Pb}/^{238}\text{U}$ or $^{207}\text{Pb}/^{206}\text{Pb}$ ages of 924 ± 8 Ma (Liu et al., 2006), 930 ± 10 Ma (Gao et al., 2009) / 940.6 ± 5 Ma (Zhao et al., 2019), 933 ± 14 Ma / 919 ± 12 Ma (Wang et al., 2012), 897 ± 16 Ma / 890 ± 14 Ma (Wang et al., 2012), 913 ± 10 Ma (Zhu et al., 2019), and 906 ± 10 Ma (Su et al., 2021), respectively. The youngest group of detrital zircons from the underlying Xinxing Formation yielded a U-Pb age of 1121 ± 27 Ma (Yang et al., 2012). These radioisotopic ages allow us to place conservative estimates on the age range for deposition of the Huaibei Group (from Xinxing to Wangshan Fms) of 1121 ± 27 to 897 ± 16 Ma.

$\delta^{13}\text{C}_{\text{carb}}$ values from the Huaibei Group range from -2‰ to $+4\text{‰}$ and $^{87}\text{Sr}/^{86}\text{Sr}$ ratios from 0.7052 to 0.7061 (Fig. 2D, Xiao et al., 2014; Zhou et al., 2020), which are typical of the Mesoproterozoic–Neoproterozoic transitional interval worldwide. These are also supported by biostratigraphic studies (Dong et al., 2008; Xiao et al., 2014) and particularly by the occurrence of *Trachyhystrichosphaera aimika* (*T.aimika*), a Tonian age diagnostic index acritarch, in both the Huaibei and Huainan areas of the NCC (Tang et al., 2013, 2015).

Late Mesoproterozoic–early Neoproterozoic successions in the

Huainan region are represented by the Huainan and Feishui groups (Fig. 2B). The Huainan Group is composed of the Caodian, Bagongshan and Liulaobei Formations, whereas the Feishui Group is made up of the Shouxian, Jiuliqiao and Sidingshan Formations. Depositional ages of the Huainan and Feishui groups can be roughly bracketed between the Mesoproterozoic and Ediacaran, given that they overlie the Paleoproterozoic Fengyang Group and underlie the Fengtai Formation of probable Ediacaran age (Liu and Cai, 2017; Zhou et al., 2019). Detrital zircon U-Pb dating from the basal Feishui Group (Shouxian Formation) constrains its maximum depositional age to be 1084 ± 10 Ma (Zhao et al., 2019; Sun et al., 2020). Lithological and isotopic correlation of the Sidingshan Formation in the Feishui Group with the Jiudingshan Formation in the Huaibei Group (e.g. Xiao et al., 2014) implies that the carbonate units dated in our study are younger than the Shouxian Formation, so the age of 1084 ± 10 Ma also represents an indirect maximum age constraint on carbonate successions of the Huaibei Group. Biostratigraphically, *T.aimika*'s appearance in the Liulaobei Formation favors a Tonian age (Tang et al., 2013). The occurrence of *Sinosabellidites*, *Pararenicola*, *Protoarenicola* in the Liulaobei and Jiuliqiao formations also indicates a Tonian age based on biostratigraphic correlation with Russia and India (Xiao et al., 2014). Furthermore, recent provenance analysis of the Huaibei and Huainan region supports the hypothesis that the Xuhuai rift basins along the southeastern margin of the NCC, comprise the same rift system during 1.1–0.9 Ga as the coeval basins along the eastern and western margin of the São Francisco craton, as

well as those along the southwestern margin of the Congo craton (Sun et al., 2020).

In this study, a total of twelve fresh carbonate/marl hand specimens from seven stratigraphic units at the southeastern margins of NCC were prepared as 100 μ m thick polished thin sections for carbonate U-Pb dating (Figs. 3, 4). The collected samples are: XS04 (a sample of light grey dolomitic limestone from the upper Jiayuan Formation at Jiayuan Section, Pizhou County); SX129 (a sample of light grey, stromatolitic dolostone from the basal Jiudingshan Formation); three samples from the Zhangqu Formation: SX123 (a dark grey muddy limestone with clay laminations from the lower to middle part), SX67 (a typical dark limestone from the upper formation), and SX119 (a dolomitic limestone from the top of the formation); three samples from the Weiwei Formation: SX107 and SX117 (stromatolitic carbonate from the lower half of the formation), and SX106 (a laminated muddy dolostone from the upper Weiwei Formation). All Jiudingshan, Zhangqu and Weiwei samples were collected at Longshan and Yinjiazhai sections, Lingbi County. In addition, SX11 (a typical dolomitic limestone interbedded with muddy layers from the lower Wangshan Formation) was collected at Jinshanzhai Section, Suzhou County. Samples M65 (a calcareous siltstone from the Liulaobei Formation), M113 (grayish limestone from the Liulaobei Formation) and M57 (grayish dolomitic limestone from the Jiuliqiao Formation) were collected at the Guanyindongshan and Ma'anshan sections, Huoqiu County.

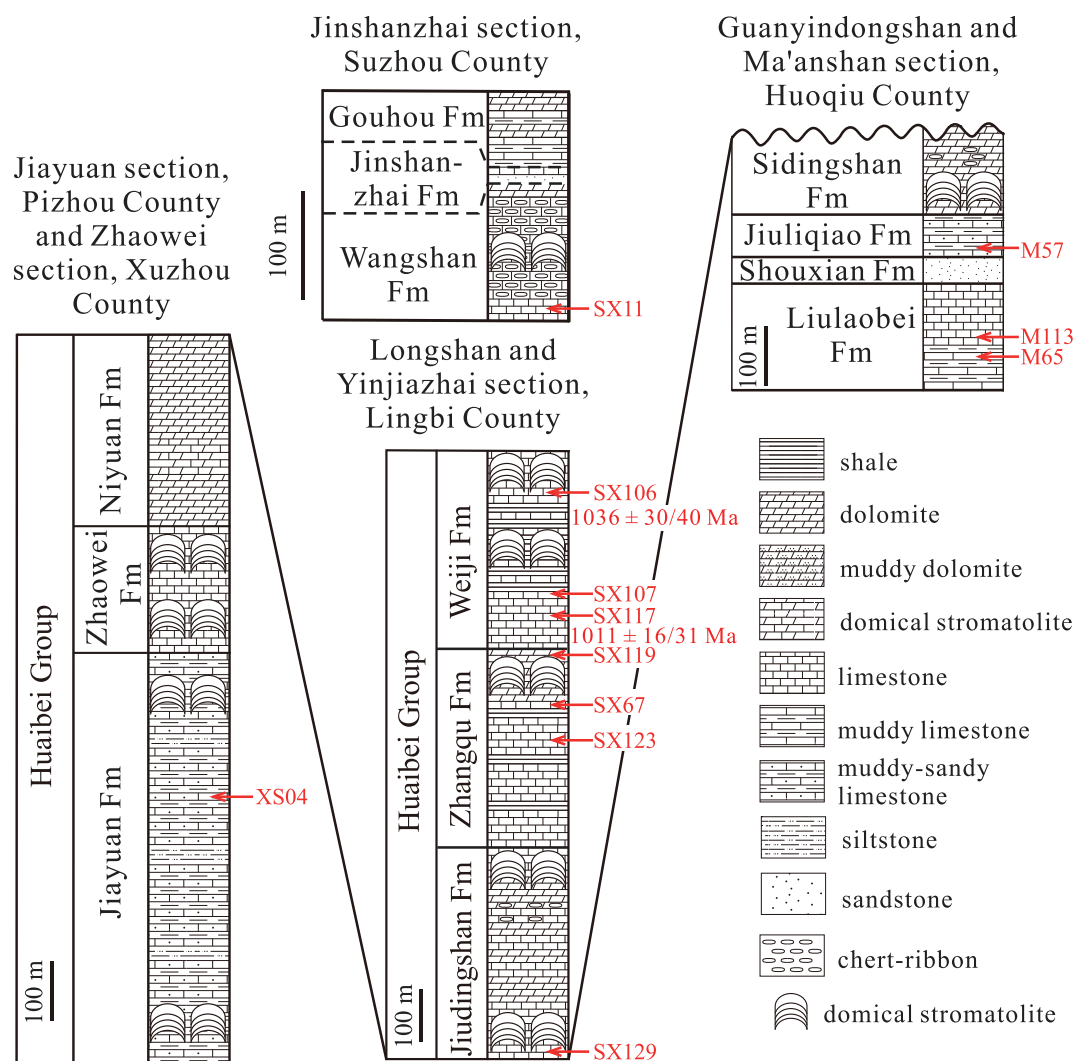


Fig. 3. Stratigraphic columns showing the sampling sections and horizons in the Huaibei and western Huainan regions.

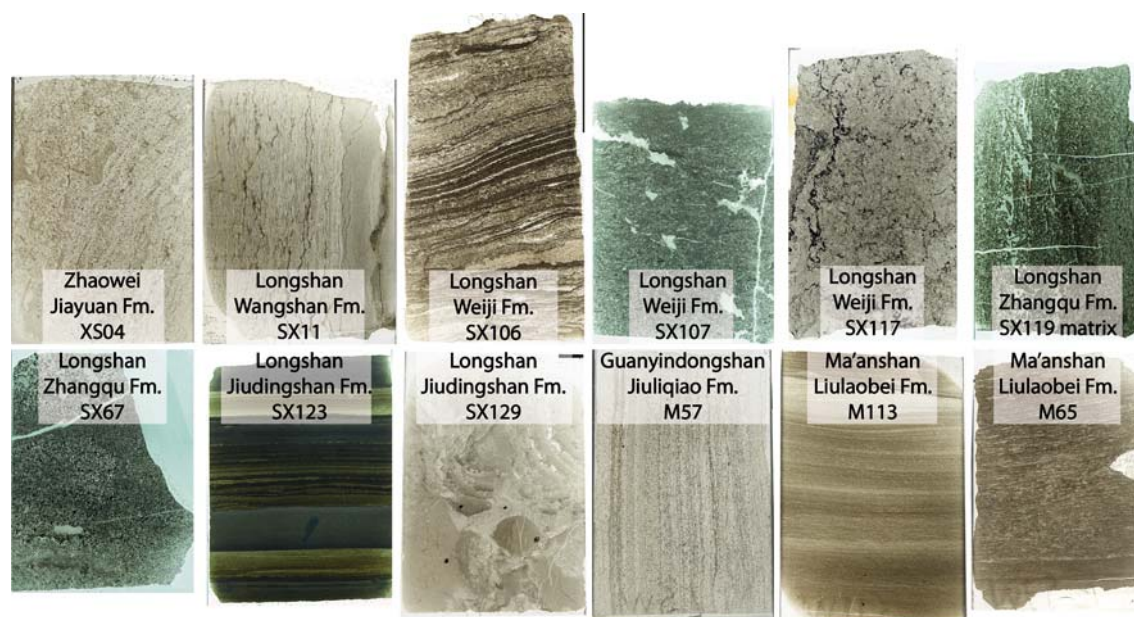


Fig. 4. Thin section photomicrographs showing the petrographic variability amongst the sampled carbonates and muddy carbonates in the Huainan and Huai-bei regions.

3. Analytical methods

Prior to U-Pb dating, optical examination was conducted on polished thin sections followed by Secondary Electron Microscopy (SEM) and Cathodoluminescence (CL) imaging of specific sample areas in order to distinguish different phases and areas of alteration (methodology in Roberts et al., 2020). LA-ICP-MS U-Pb geochronology was conducted at the Geochronology and Tracers Facility, British Geological Survey, UK, using the protocol as described in Roberts and Walker (2016), Roberts et al. (2017) and Roberts et al. (2020). The instrumentation was a Nu Instruments Attom single collector ICP-MS, coupled to a NWR193UC laser ablation system fitted with a TV2 cell. Ablation conditions were a 80 μm spot, ablated for 20 s, using a fluence of 5 J/cm² with a repetition rate of 10 Hz. A gas blank of 60 s was subtracted at the beginning of each run, and a washout of 5 s was allowed between each ablation. For detailed experimental conditions refer to Supplement 01.

Standard sample bracketing was employed, using NIST614 glass (values of Woodhead and Hergt, 2001) for normalization of Pb-Pb ratios, and WC1 (254 Ma; Roberts et al., 2017) for normalization of Pb-U ratios. ASH15D was run as a secondary reference material (2.964 ± 0.009 Ma; Nuriel et al., 2021) during one session, and provided an age of 2.886 ± 0.109 Ma. Duff Brown Tank (64.04 ± 0.67 Ma; Hill et al., 2016) was run as another secondary reference material yielding an age of 65.34 ± 0.61 Ma, indicating an accuracy within the ca. 2.5 % uncertainty of the WC1 reference material. Uncertainty propagation is based on the fundamentals of Horstwood et al. (2016), and age uncertainties are quoted as $\pm \alpha/\beta$, where α is without systematic uncertainties, and β is with systematic uncertainties. The latter include the decay constant for ²³⁸U, the uncertainty of the WC1 reference material, and an estimate of the long-term reproducibility (as excess variance) of our ²³⁸U/²⁰⁶Pb measurements (this is somewhat difficult to fully characterize without homogeneous secondary reference materials).

4. Results

LA-ICP-MS calcite U-Pb dating results are tabulated in Supplement 02. Sample XS04 is a grey muddy limestone from the lower Jiayuan Formation at the Jiayuan section, Pizhou County (Fig. 3). A total of 54 point analyses were conducted on the matrix of sample XS04 (Fig. 6), yielding an intercept age of $798 \pm 103/106$ Ma (MSWD = 2.9).

Sample SX11 is a grey limestone from the middle Wangshan Formation at Jinshanzhai section, Suzhou County (Fig. 3). A total of 92 spot analyses were conducted (Fig. 6). The data are highly scattered, hindering a single regression calculation. Although applied with caution, the data can be bound by regressions dated at 1700 and 400 Ma.

Sample SX106 is a dark limestone from the upper Weiji Formation at Yinjiazhai section, Lingbi County, which is ca. 280 m distance from its base (Fig. 3). It consists of alternating laminations of microspar to fine calcite spar with a dark CL color suggestive of primary precipitation (Fig. 5a). Of these, laminations of the coarsest spar have been exclusively selected for calcite U-Pb analysis. A total of 144 point analyses were conducted on sample SX106 (Fig. 6) which yielded a lower intercept age of $1036 \pm 31/45$ Ma (MSWD = 1.3).

Sample SX107 is a limestone from the middle-lower Weiji Formation at Longshan section, Lingbi County, which is ca. 120 m distance from its base (Fig. 3). Secondary calcite veins and cracks occur (Fig. 4), as well different domains of sparry micrite. A coarser patch of micrite yielded a poorly defined regression dominated by common Pb (Fig. 6) with a lower intercept age of $1042 \pm 212/215$ Ma (MSWD = 2.4). A patch of micrite representing recrystallisation of a fossil yielded a regression with a lower intercept age of $860 \pm 124/127$ Ma (MSWD = 3.2). A fine-grained sparry micrite domain yielded a regression with a lower intercept age of $831 \pm 118/121$ Ma (MSWD = 3.4). Finally, a vein yielded a regression with a higher content of radiogenic Pb, and a lower intercept age of $142.5 \pm 10.5/11.4$ Ma (MSWD = 6.1).

Sample SX117 is a microsparitic limestone from the lower Weiji Formation at Longshan section, Lingbi County, which is ca. 80 m distance from its base (Fig. 3). It is generally homogeneous and relatively pure with pockets of clotted micrite and spar, and thin, wispy organic laminations (Fig. 5b). Calcite veins and cracks occasionally occur (Fig. 5b). For calcite U-Pb dating, cracks were avoided and only smooth surfaces with densely packed calcite spar (30–50 μm crystal size) were selected. CL images of dated regions are dark to the naked eye, suggestive of primary precipitation (Fig. 5b). The calcite veins are grey-green, have a smoother surface and a mixed CL response. A total of 120 point analyses were conducted on the isolated pockets of micro spar of sample SX117. One region had a mixed CL response, suggesting the possibility of mixed phases, thus we didn't include this region from the regression (leaving a total of 100 spots). When disregarding one outlier (which lowers the MSWD from 1.7 to 1.5), a lower intercept age of 1010

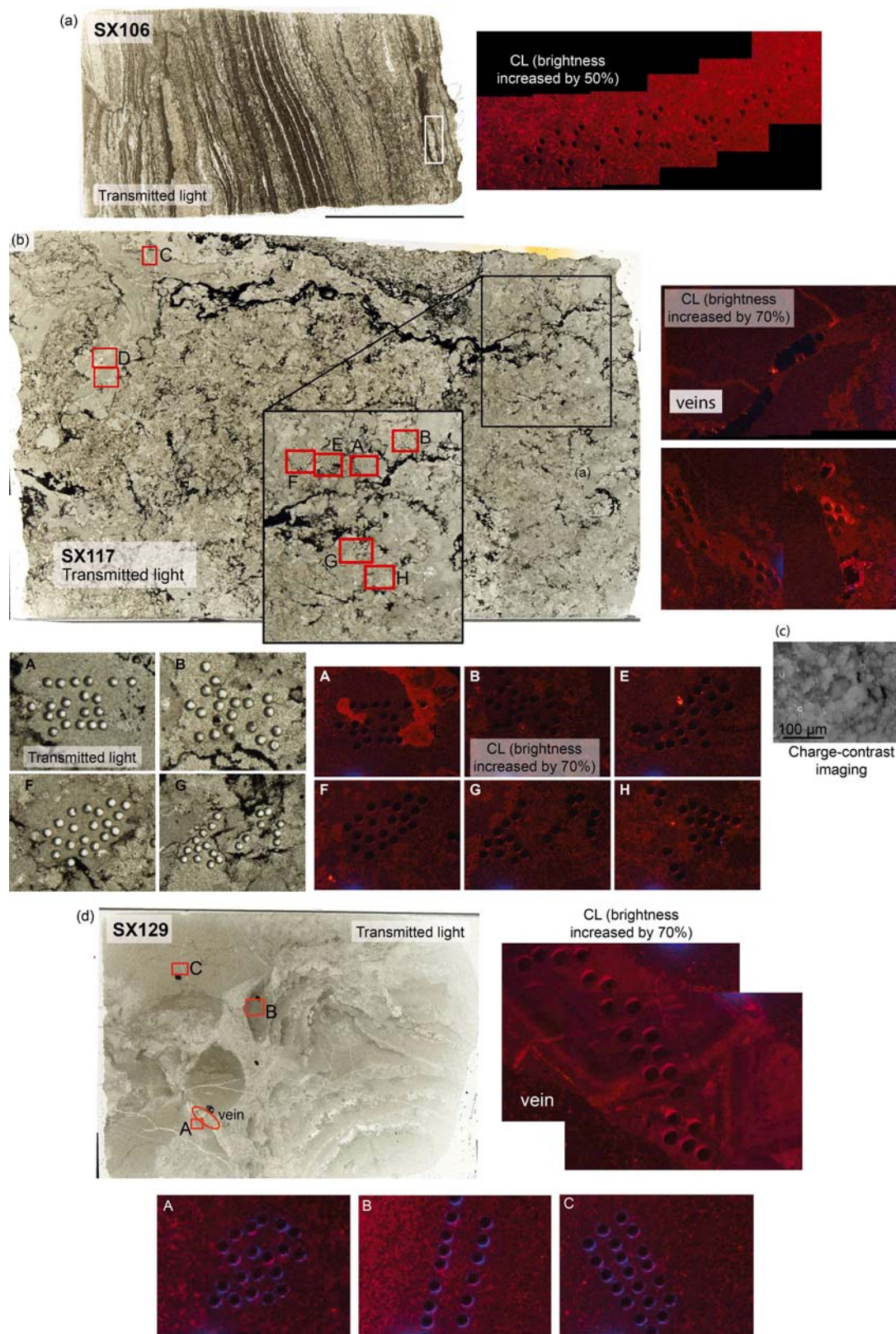


Fig. 5. (A) Transmitted light photomicrograph of entire thin section of sample SX106, with region imaged by CL shown by white box; and corresponding CL image. (B) Transmitted light photomicrograph of thin section of SX117, highlighting the regions analysed for U-Pb; and corresponding transmitted light and CL photomicrographs of labelled regions. (C) Charge-contrast image of microspar of SX117. (D) Transmitted light photomicrograph of thin section of SX129, showing regions analysed by U-Pb; and corresponding CL images of calcite microspar and vein region. CL images are almost dark to the naked eye, and thus the brightness is turned up by a fixed amount to show the textural detail.

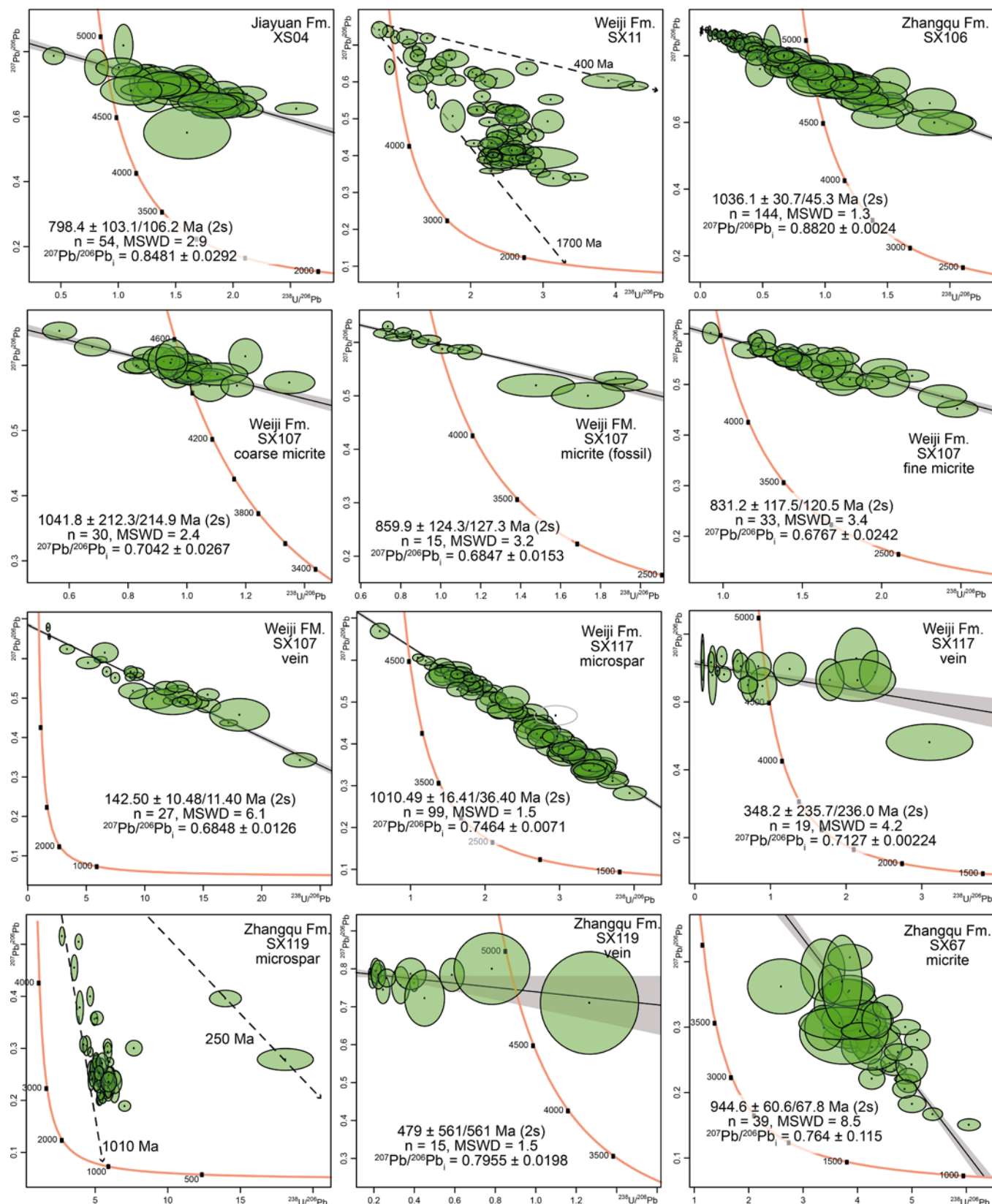


Fig. 6. Tera-Wasserburg plots for samples XS04, SX11, SX106, SX107, SX117, SX119 and SX67. All ellipses are 2σ uncertainties.

$\pm 16/36$ Ma (MSWD = 1.5) was obtained (Fig. 6). A total of 19 analyses were obtained on a calcite vein intersecting this sample, the data do not form a robust regression, but imply a younger age of recrystallization. The free regression through the data provides a lower intercept age of

$348 \pm 236/236$ Ma (Fig. 6).

Sample SX119 is a dark thin-bedded limestone from the upper Zhangqu Formation at Longshan section, Lingbi County (Fig. 3). It has pervasive late-stage veining and comprises blocky microspar (similar to

SX117 but not as pure), with isolated clots of brown peloidal fabric. The data from sample SX119 are too spread to constitute a robust regression (Fig. 6). However, plotting a reference line intercepting at 1010 Ma, indicates that the sample probably formed around the same time as other samples. Fifteen data points from the vein constitute a regression with a lower intercept age of $479 \pm 561/561$ Ma (Fig. 6).

Sample SX67 is a dark grey limestone from the upper Zhangqu Formation at Yinjiashai section, Lingbi County, which is ca. 100 m distance from its top (Fig. 3). Secondary calcite veins and cracks occur (Fig. 4), which were avoided for calcite U-Pb dating, and several domains of micrite were split by their appearance. The fine-grained micro-spar matrix yielded radiogenic data (Fig. 6), but with a scattered array, provided an imprecise lower intercept age of $945 \pm 61/68$ Ma (MSWD = 8.5). A distinct patch of micritic spar did not provide a regression, and bounding regressions purely for demonstration provide maximum and minimum ages of 500 and 220 Ma. An area that looks to be recrystallized with coarser spar, also does not yield a regression, with bounding regressions calculated at 1150 and 300 Ma (Fig. 7).

Sample SX123 is a grey dolomitic limestone from the upper Zhangqu Formation at Longshan section, Lingbi County, which is ca. 150 m distance beneath its top (Fig. 3). The transmitted light image shows that it consists of alternating laminations of organic-rich and micritic-microsparitic layers of variable width (Fig. 4). A total of 80 spot analyses were conducted on sample SX123 (Fig. 7). The data are highly non-radiogenic, falling entirely to the left of the concordia line, and yielding an apparent lower intercept age of $533 \pm 78/80$ Ma (MSWD = 1.3).

Sample SX129 is a grey limestone with clotted micrite and microspar patches from the basal Jiudingshan Formation at Longshan section, Lingbi County (Fig. 3). It shows a dark CL color and the occurrence of bright, very fine veins extending in varying directions (Fig. 5d). A total of 99 spot analyses were conducted on microspar of sample SX129 which yielded a lower intercept age of $881 \pm 49/54$ Ma. The data are rather scattered (MSWD = 3.5); however, this scatter was largely derived from data obtained from one specific region of the sample. Removing this region of spots from the regression provided a lower intercept age of $977 \pm 71/78$ Ma (MSWD = 2.8) (Fig. 7).

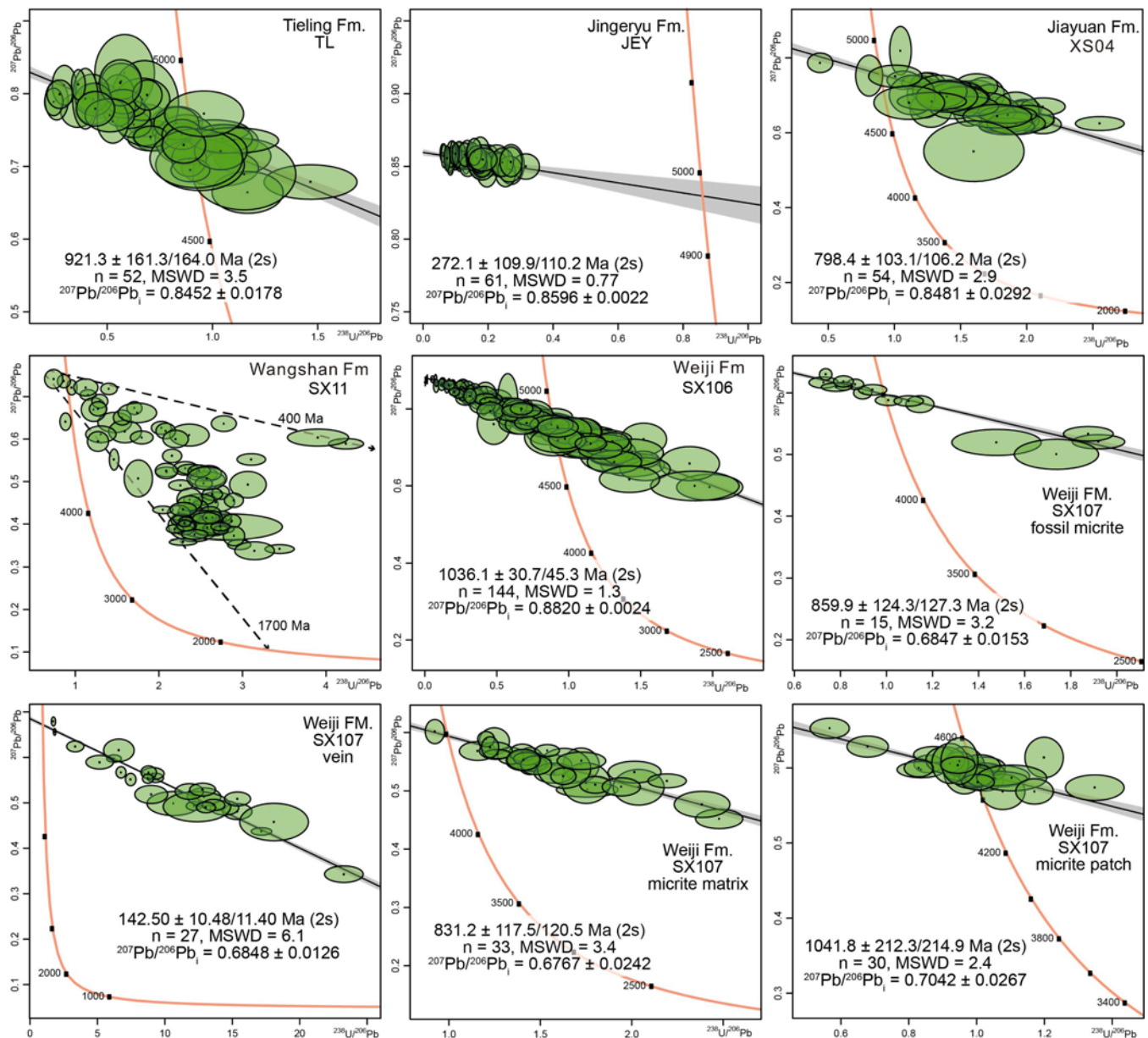


Fig. 7. Tera-Wasserburg plots for samples SX67, SX123, SX129, M57, M113 and M65. Pooled analyses of reference materials Duff Brown Tank and ASH15D also shown (systematic uncertainties not propagated). All ellipses are 2σ uncertainties.

Sample M57 is a grey laminated muddy limestone from the basal Jiuliqiao Formation at Guanyindongshan section, Huoqiu County (Fig. 3). A total of 23 spot analyses were conducted. The data are highly scattered and non-radiogenic, falling entirely to the left of the concordia line (Fig. 7), and yielding an apparent lower intercept age of $1775 \pm 1283/1284$ Ma (MSWD = 29).

Sample M113 is a dark grey limestone from the middle Liulaobei Formation at Ma'anshan section, Huoqiu County (Fig. 3). Thirty eight data points from the microspar provide a regression with a lower intercept age of $890 \pm 252/253$ Ma (MSWD = 9.8; Fig. 7).

Sample M65 is a dark grey limestone from the lower Liulaobei Formation at Ma'anshan section, Huoqiu County (Fig. 3). A total of 25 spot analyses were conducted. The data have large datapoint uncertainties (Fig. 7), and lack strongly radiogenic compositions, yielding an apparent lower intercept age of $298 \pm 161/161$ Ma (Fig. 7).

5. Discussion

5.1. Primary age constraints?

The age data produced from this suite of carbonates are highly variable in terms of the amount of radiogenic Pb, the amount of scatter, and the datapoint uncertainties. All of these factors compound a simple interpretation of the resulting ages. We have used an objective criterion to screen for robust ages: age uncertainties of less than 10%, and a MSWD below 2. Only two dates pass these criteria, those of SX106 and SX117, at $1036 \pm 31/45$ and $1010 \pm 16/36$ Ma, respectively. Since these dates both arise from microspar that comprises the bulk of these samples, we interpret them to reflect the best estimate of a depositional age. SX129 yielded an array with a MSWD of 2.8 and an age uncertainty of 8%. This age overlaps those of SX106 and SX117, albeit with a large uncertainty, and also poses a potential primary depositional age.

Several samples have more scattered regressions that overlap the ages of SX106 and SX117 (SX11, SX107, SX119, M113), or provide apparently younger intercept ages (XS04, SX107, SX67, SX123, M57, M65). Since these exhibit scatter, and are generally lacking in radiogenic Pb that provides more confidence in the age interpretation, it is difficult to pinpoint the accuracy of these age estimates. Samples where several domains have been dated yield varying apparent ages, i.e. SX107 and SX67. These sample data indicate that at least some samples within the studied successions have been host to later diagenetic or hydrothermal alteration that has affected the U-Pb isotope system (Roberts et al., 2020). This is corroborated by dated vein domains that all yield demonstrably younger ages, ranging from ca. 480 to 143 Ma. We do not wish to place any particular significance on the meaning of the younger age estimates, but we note some of the ages overlap the Paleozoic Caledonian orogeny affecting the North Qinling region, an adjacent terrane to the southern margin of North China Craton (Dong and Santosh, 2016). In addition, the younger ca. 889–798 Ma ages are within uncertainty of the timing of ca. 940–897 Ma dyke swarms in the upper Huaibei Group (Liu et al., 2006; Gao et al., 2009; Wang et al., 2012; Zhao et al., 2019; Zhu et al., 2019; Su et al., 2021). This indicates a possible genetic link, with fluid-related alteration/recrystallization being driven by intrusion-related hydrothermal activity. As such, Proterozoic sedimentation in the southern margin of North China Craton was probably influenced by several tectonothermal events, leading to fluid circulation in these early formed Proterozoic sedimentary successions, and forming veins that yield younger radioisotopic ages. Such fluid circulation driven by orogenic magmatism is not uncommon in Precambrian sedimentary successions, and can induce multiple episodes of authigenic/hydrothermal mineral growth following their initial deposition (e.g. Lan et al., 2013).

The combination of younger vein ages, and scattered data in recrystallized or potentially altered domains, highlights the challenge in obtaining primary ages from ancient carbonate successions. Ideally, objective criteria for distinguishing primary ages should first be

conducted on the material using petrographic methods. Using the U-Pb data alone is subject to potential inaccuracy, since it is possible that later events could also provide reliable age constraints. In this study, we note that our most robust results come from the purest coarser regions of homogeneous microspar, distant from veins, laminations, and other textural heterogeneities.

5.2. Relevance of the new ages

Our interpreted primary calcite U-Pb dates of 1036 ± 45 Ma and 1010 ± 36 Ma for the Weiji Formation, both fall within known radioisotopic age constraints for the Huaibei Group of 1121 ± 27 Ma to 913 ± 10 Ma (Yang et al., 2012; Zhu et al., 2019; Su et al., 2021). Insofar as carbonates from the Huaibei Group are relatively well preserved (Xiao et al., 2014; Zhou et al., 2020), these calcite U-Pb ages are interpreted to faithfully record the depositional age of the sampled horizons, and thus provide new absolute chronological markers for this succession. An independent analysis on the basis of measured rate of change of seawater $^{87}\text{Sr}/^{86}\text{Sr}$ estimated an approximate 60 million-year duration for carbonate rocks within the Huaibei Group (Zhou et al., 2020). Considering the occurrence of ca. 920–900 Ma dyke swarms in the upper Huaibei Group, carbonate rocks of the middle-lower Huaibei Group have been estimated at ca. 980 Ma (Zhou et al., 2020). The most precise age from the Weiji Formation, i.e. 1010 ± 36 Ma, overlaps within uncertainty, the ca. 980 Ma age inferred by independent strontium isotope analysis, and provides a pinning point in absolute time for this succession.

$\delta^{13}\text{C}_{\text{carb}}$ values of carbonate rocks from the Jiayuan, Zhaowei, Niyuan, Jiudingshan, Zhangqu and Weiji Formations in the Huaibei Group fall in the range of +2 to +4‰ (deviation from V-PDB) and decrease to –2 to 0‰ in the Shijia Formation, followed by an increase to 0 to +4‰ in the Wangshan Formation (Xiao et al., 2014). Such a trend is consistent with other late Mesoproterozoic-early Neoproterozoic geochemical records elsewhere, particularly in Siberia, Canada, Brazil and Mauritania (Kah et al., 2001; Bartley et al., 2001; Frank et al., 2003; Silva-Tamayo et al., 2018; Zhou et al., 2020). Carbonate rocks from the Niyuan, Jiudingshan, and Zhangqu Formations have relatively unradiogenic $^{87}\text{Sr}/^{86}\text{Sr}$ ratios (commonly 0.7053–0.7064), whereas those from the Wangshan Formation have relatively higher $^{87}\text{Sr}/^{86}\text{Sr}$ ratios > 0.7064 (Xiao et al., 2014; Zhou et al., 2020). The trends of the $^{87}\text{Sr}/^{86}\text{Sr}$ ratios are also typical of the late Mesoproterozoic-early Neoproterozoic transitional interval (<0.7065), and contrast with the gradual increase of $^{87}\text{Sr}/^{86}\text{Sr}$ ratios in the middle Neoproterozoic (0.7070–0.7075) and abrupt increase of values (>0.7085) during the Ediacaran Period (Halverson et al., 2010; Silva-Tamayo et al., 2018).

Our new U-Pb dates also align with biostratigraphic constraints. The Liulaobei Formation in the Huainan region hosts the age-diagnostic acritarch fossil *Trachyhystrichosphaera aimika*, which is known from about 20 sections worldwide of ca. 1150–720 Ma (Pang et al., 2020) or ca. 1100–800 Ma age (Riedman and Sadler, 2018). It is found together with other forms of characteristically Meso-Neoproterozoic acritarch fossils such as *Trachysphaeridium lauffeldi*, *Satka favosa* and *Simia annulata*. Traditional lithostratigraphy allows correlation of the Liulaobei and Shouxian Formations of the Huainan region with the Xinxing and Jushan Formations of the Huaibei region (Dong et al., 2008; Zhao et al., 2019), which is constrained to an age range of 1121 ± 27 to 940.6 ± 5 Ma (Liu et al., 2006; Yang et al., 2012; Zhao et al., 2019).

In summary, our new laser ablation U-Pb ages are consistent with all available geochronologic, chemostratigraphic and biostratigraphic age constraints. Moreover, they represent the oldest obtained by the LA-ICP-MS method published thus far (c.f. 655 Ma; Liivamägi et al., 2021), greatly extending the possibilities of utilizing this method for constraining the ages of Proterozoic sedimentary successions. The most precise age (SX117) of $1010 \pm 16/36$ Ma has an analytical precision of 1.6%, highlighting that the systematic uncertainties, dominated by the reference material uncertainty of ~ 2.5% (Roberts et al., 2017), provide a significant limiting constraint on the precision at which reported age

data can be interpreted. As further reference materials are characterized and become used widely (e.g. Guillong et al., 2020; Nuriel et al., 2021), this limit can potentially be reduced in the future.

6. Conclusions

In this study, two meaningful carbonate U-Pb ages of 1010 ± 36 Ma (lower Weiji Formation) and 1036 ± 45 Ma (upper Weiji Formation) were obtained from early diagenetic, fine-grained sparite samples of the Huaibei Group on the North China Craton. These new ages are supported by existing geochronology, chemostratigraphy and biostratigraphy, and help to produce a more precise age model for the Huaibei Group and its correlatives. The success of this study gives us confidence that reliable U-Pb carbonate ages for other Precambrian successions may be obtained in the future. Because Precambrian carbonate rocks host important information about the evolution of life and oxygenation of the hydrosphere and atmosphere, laser ablation U-Pb dating of carbonate minerals holds considerable promise for constraining key timing nodes for these biological and environmental events.

Declaration of Competing Interest

The authors declare that they have no known competing financial interests or personal relationships that could have appeared to influence the work reported in this paper.

Acknowledgements

This project was funded by National Science Foundation of China (grants 41673016 to ZWL and 41630211 to TPZ), State Key Laboratory of Lithospheric Evolution, Institute of Geology and Geophysics, Chinese Academy of Sciences (grant SKL-Z202001 to ZWL), State Key Laboratory of Palaeobiology and Stratigraphy, Nanjing Institute of Geology and Palaeontology, Chinese Academy of Sciences (grant 193112 to ZWL), and State Key Laboratory of Geological Processes and Mineral Resources, China University of Geosciences (grant GPMR201902 to ZWL). Zhuoya Zhao was appreciated for assistance with field work. We are indebted to Graham Shields for discussion and language improvement.

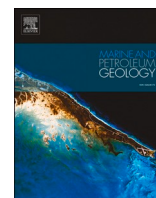
Appendix A. Supplementary data

Supplementary data to this article can be found online at <https://doi.org/10.1016/j.precamres.2021.106551>.

References

- Baludikay, B.K., Storme, J.-Y., François, C., Baudet, D., Javaux, E.J., 2016. A diverse and exquisitely preserved organic-walled microfossil assemblage from the Meso-Neoproterozoic Mbuj-Mayi Supergroup (Democratic Republic of Congo) and implications for Proterozoic biostratigraphy. *Precamb. Res.* 281, 166–184.
- Bartley, J.K., Semikhatov, M.A., Kaufman, A.J., Knoll, A.H., Pope, M.C., Jacobsen, S.B., 2001. Global events across the Mesoproterozoic-Neoproterozoic boundary: C and Sr isotopic evidence from Siberia. *Precamb. Res.* 111, 165–202.
- Beghin, J., Storme, J.-Y., Blanpied, C., Gueneli, N., Brocks, J.J., Poulton, S.W., Javaux, E. J., 2017. Microfossils from the late Mesoproterozoic-early Neoproterozoic Atar/Elmreiti Group, Taoudeni Basin, Mauritania, northwestern Africa. *Precamb. Res.* 291, 63–82.
- Cao, R.J., Zhao, W.J., Xia, G.S., 1985. Late Precambrian stromatolites from north Anhui Province. *Mem. J. Nanjing Inst. Geol. Palaeontol., Academy Sinica* 21, 1–54.
- Cao, R.J., Yuan, X.L., Xiao, S.H., 2001. On morphogenesis of Conophyton stromatolites. *Acta Palaeontologica Sinica* 40, 318–329.
- Chu, X.L., Zhang, T.G., Zhang, Q.R., Lyons, T.W., 2007. Sulfur and carbon isotope records from 1700 to 800 Ma carbonates of the Jixian section, northern China: implications for secular isotope variations in Proterozoic seawater and relationships to global supercontinental events. *Geochim. Cosmochim. Acta* 71, 4668–4692.
- Condon, D.J., Bowring, S.A., 2011. A user's guide to Neoproterozoic geochronology. *Geol. Soc. Lond. Mem.* 36, 135–149.
- Dong, L., Xiao, S., Shen, B., Yuan, X., Yan, X., Peng, Y., 2008. Restudy of the worm-like carbonaceous compression fossils Protoarenicola, Pararenicola, and Sinosabellites from early Neoproterozoic successions in North China. *Palaeogeogr. Palaeoclimatol. Palaeoecol.* 258, 138–161.
- Dong, Y., Santosh, M., 2016. Tectonic architecture and multiple orogeny of the Qinling Orogenic Belt, Central China. *Gondwana Res.* 29, 1–40.
- Frank, T.D., Kah, L.C., Lyons, T.W., 2003. Changes in organic matter production and accumulation as a mechanism for isotopic evolution in the Mesoproterozoic Ocean. *Geol. Mag.* 140, 397–420.
- Fu, X., Zhang, S., Li, H., Ding, J., Li, H., Yang, T., Wu, H., Yuan, H., Lv, J., 2015. New paleomagnetic results from the Huaibei Group and Neoproterozoic mafic sills in the North China Craton and their paleogeographic implications. *Precamb. Res.* 269, 90–106.
- Gao, L.Z., Zhang, C., Liu, P.J., Tang, F., Song, B., Ding, X., 2009. Reclassification of the Meso- and Neoproterozoic chronostratigraphy of North China by SHRIMP zircon ages. *Acta Geol. Sin.* 83, 1074–1084.
- Guillong, M., Wotzlaw, J.F., Looser, N., Laurent, O., 2020. Evaluating the reliability of U-Pb laser ablation inductively coupled plasma mass spectrometry (LA-ICP-MS) carbonate geochronology: matrix issues and a potential calcite validation reference material. *Geochronology* 2, 155–167.
- Halverson, G.P., Wade, B.P., Hurtgen, M.T., Barovich, K.M., 2010. Neoproterozoic chemostratigraphy. *Precamb. Res.* 182, 337–350.
- He, T., Zhou, Y., Vermeesch, P., Rittner, M., Miao, L., Zhu, M., Carter, A., Pogge von Strandmann, P.A.E., Shields, G.A., 2017. Measuring the “Great Unconformity” on the North China Craton Using New Detrital zircon age data. *Geol. Soc. Lond. Spec. Publ.* 448, 145–159.
- Hill, C.A., Polyak, V.J., Asmerom, Y., P. Provencio, P., 2016. Constraints on a Late Cretaceous uplift, denudation, and incision of the Grand Canyon region, southwestern Colorado Plateau, USA, from U-Pb dating of lacustrine limestone. *Tectonics* 35, 896–906.
- Horstwood, M.S.A., Köser, J., Gehrels, G., Jackson, S.E., McLean, N.M., Paton, C., Pearson, N.J., Sircombe, K., Sylvester, P., Vermeesch, P., Bowring, J.F., Condon, D.J., Schoene, B., 2016. Community-derived standards for LA-ICP-MS U-Th-Pb geochronology—uncertainty propagation, age interpretation and data reporting. *Geostand. Geoanal. Res.* 40, 311–332.
- Jahn, B.-M., 1988. Pb-Pb dating of young marbles from Taiwan. *Nature* 332, 429–432.
- Jahn, B.-M., Cuvelier, H., 1994. Pb-Pb and U-Pb geochronology of carbonate rocks: an assessment. *Chem. Geol.* 115, 125–151.
- Kah, L.C., Lyons, T.W., Chesley, J.T., 2001. Geochemistry of a 1.2 Ga carbonate-evaporite succession, northern Baffin and Bylot Islands: Implications for Mesoproterozoic marine evolution. *Precamb. Res.* 111, 203–234.
- Lan, Z.-W., Chen, Z.-Q., Li, X.-H., Li, B., Adams, D., 2013. Hydrothermal origin of the Paleoproterozoic xenotime from the King Leopold Sandstone of the Kimberley Group, Kimberley, NW Australia: Implications for a ca 1.7 Ga far field hydrothermal event. *Aust. J. Earth Sci.* 60, 497–508.
- Li, Q., Parrish, R.R., Horstwood, M.S.A., McArthur, J.M., 2014. U-Pb dating of cements in Mesozoic ammonites. *Chem. Geol.* 376, 76–83.
- Liivamägi, S., Šrodoň, J., Bojanowski, M.J., Stanek, J.J., Roberts, N.M.W., 2021. Precambrian paleosols on the Great Unconformity of the East European Craton: An 800 million year record of Baltica's climatic conditions. *Precamb. Res.* 363, 106327. <https://doi.org/10.1016/j.precamres.2021.106327>.
- Liu, C.H., Cai, J., 2017. Provenance and depositional age of the Baiyunshan Formation of the Fengyang Group in the Wuhe Complex: Constraints from zircon U-Pb age and Lu-Hf isotopic studies. *Acta Petrologica Sinica* 33, 2867–2880 in Chinese with English Abstract.
- Liu, Y., Gao, L., Liu, Y., Song, B., Wang, Z., 2006. Zircon U-Pb dating for the earliest Neoproterozoic mafic magmatism in the southern margin of the North China Block. *Chin. Sci. Bull.* 51, 2375–2382.
- Lu, S.N., Zhao, G.C., Wang, H.C., Hao, G.J., 2008. Precambrian metamorphic basement and sedimentary cover of the North China Craton: A review. *Precamb. Res.* 160, 77–93.
- Luo, G.M., Junium, C.K., Kump, L.R., Huang, J.H., Li, C., Feng, Q.L., Shi, X.Y., Bai, X., Xie, S.C., 2014. Shallow stratification prevailed for ca. 1700 to ca. 1300 Ma ocean: Evidence from organic carbon isotopes in the North China Craton. *Earth Planet. Sci. Lett.* 400, 219–232.
- Moorbath, S., Taylor, N.P., Orpen, J.L., Treloar, P., Wilson, J.F., 1987. First direct radiometric dating of Archean stromatolite limestone. *Nature* 326, 865–867.
- Nuriel, P., Wotzlaw, J.F., Ovtcharova, M., Vaks, A., Stremtan, C., Sala, M., Roberts, N.M. W., Kylander-Clark, R.C., 2021. The use of ASH-15 flowstone as a matrix-matched reference material for laser-ablation U-Pb geochronology of calcite. *Geochronology* 3, 35–47.
- Pang, K., Tang, Q., Wan, B., Yuan, X.L., 2020. New insights on the palaeobiology and biostratigraphy of the acritarch Trachyhystrichosphaera aimika: A potential late Mesoproterozoic to Tonian index fossil. *Palaeoworld*. <https://doi.org/10.1016/j.palwor.2020.02.003>.
- Rasmussen, B., 2005. Radiometric dating of sedimentary rocks: the application of diagenetic xenotime geochronology. *Earth-Sci. Rev.* 68, 197–243.
- Rasbury, E.T., Cole, J.M., 2009. Directly dating geologic events: U-Pb dating of carbonates. *Rev. Geophys.* 47, RG3001. <https://doi.org/10.1029/2007RG000246>.
- Riedman, L.A., Sadler, P.M., 2018. Global species richness record and biostratigraphic potential of early to middle Neoproterozoic eukaryote fossils. *Precamb. Res.* 319, 6–18.
- Roberts, N.M.W., Drost, K., Horstwood, M.S.A., Condon, D.J., Chew, D., Drake, H., Milodowski, A.E., McLean, N.M., Smye, A.J., Walker, R.J., Haslam, R., Hodson, K., Imber, J., Beaudoin, N., Lee, J.K., 2020. Laser ablation inductively coupled plasma mass spectrometry (LA-ICP-MS) U-Pb carbonate geochronology: strategies, progress, and limitations. *Geochronology* 2, 33–61.
- Roberts, N.M., Walker, R.J., 2016. U-Pb geochronology of calcite mineralized faults; absolute dating of rift-related fault events on the northeast Atlantic margin. *Geology* 44, 531–534.

- Roberts, N.M.W., Rasbury, E.T., Parrish, R.R., Smith, C.J., Horstwood, M.S.A., Condon, D.J., 2017. A calcite reference material for LA-ICP-MS U-Pb geochronology. *Geochim. Geophys. Geosyst.* 18, 2807–2814.
- Shang, M.H., Tang, D.J., Shi, X.Y., Zhou, L.M., Zhou, X.Q., Song, H.Y., Jiang, G.Q., 2019. A pulse of oxygen increase in the early Mesoproterozoic ocean at ca. 1.57–1.56 Ga. *Earth Planet. Sci. Lett.* 527, 115797.
- Silva-Tamayo, J.C., Giovanni, N., Dussan-Tapias, K.T., 2018. Chemostratigraphy of the Mesoproterozoic-Neoproterozoic Transition. In: Sial, A.N., Gaucher, C., Ramkumar, M. and Ferreira, V.P. (Eds.). *Chemostratigraphy Across Major Chronological Boundaries*, Geophysical Monograph 240, First Edition, pp. 73–87.
- Su, X.D., Peng, P., Foley, S., Teixeira, W., Zhai, M.G., 2021. Initiation of continental breakup documented in evolution of the magma plumbing system of the ca. 925 Ma Dashigou large igneous province. *North China Lithos* 384–385, 105984.
- Sun, F.B., Peng, P., Zhou, X.Q., Magalhaes, A.J.C., Guadagnin, F., Zhou, X.T., Zhang, Z.Y., Su, X.D., 2020. Provenance analysis of the late Mesoproterozoic to early Neoproterozoic Xuhuai Basin in the southeast North China Craton: Implications for palaeogeographic reconstruction. *Precamb. Res.* 337, 105554.
- Tang, Q., Pang, K.e., Xiao, S., Yuan, X., Ou, Z., Wan, B., 2013. Organic-walled microfossils from the early Neoproterozoic Liulaobei Formation in the Huainan region of North China and their biostratigraphic significance. *Precamb. Res.* 236, 157–181.
- Tang, Q., Pang, K.e., Yuan, X., Wan, B., Xiao, S., 2015. Organic-walled microfossils from the Tonian Gouhou Formation, Huaibei region, North China Craton, and their biostratigraphic implications. *Precamb. Res.* 266, 296–318.
- Tang, Q., Pang, K.e., Yuan, X., Xiao, S., 2017. Electron microscopy reveals evidence for simple multicellularity in the Proterozoic fossil Chuaria. *Geology* 45, 75–78.
- Wan, B., Tang, Q., Pang, K.e., Wang, X., Bao, Z., Meng, F., Zhou, C., Yuan, X., Hua, H., Xiao, S., 2019. Repositioning the Great Unconformity at the southeastern margin of the North China Craton. *Precamb. Res.* 324, 1–17.
- Wang, G., Zhang, S., Li, S., Yan, Y., Dou, S., Fang, D., 1984. Research on the Upper Precambrian of Northern Jiangsu and Anhui Provinces. Anhui Press of Science and Technology, Hefei, Anhui, pp. 209 pp.
- Wang, QingHai, Yang, DeBin, Xu, WenLiang, 2012. Neoproterozoic basic magmatism in the southeast margin of North China Craton: evidence from whole-rock geochemistry, U-Pb and Hf isotopic study of zircons from diabase swarms in the Xuzhou-Huaibei area of China. *Sci. China Earth Sci.* 55, 1461–1479.
- Woodhead, J.D., Hergt, J.M., 2001. Strontium, neodymium and lead isotope analyses of NIST glass certified reference materials: SRM 610, 612, 614. *Geostandard Newsletters* 25, 261–266.
- Xiao, S., Shen, B., Tang, Q., Kaufman, A.J., Yuan, X., Li, J., Qian, M., 2014. Biostratigraphic and chemostratigraphic constraints on the age of early Neoproterozoic carbonate successions in North China. *Precamb. Res.* 246, 208–225.
- Yang, D.-B., Xu, W.-L., Xu, Y.-G., Wang, Q.-H., Pei, F.-P., Wang, F., 2012. U-Pb ages and Hf isotope data from detrital zircons in the Neoproterozoic sandstones of northern Jiangsu and southern Liaoning Provinces, China: implications for the late Precambrian evolution of the southeastern North China Craton. *Precamb. Res.* 216–219, 162–176.
- Zhao, H., Zhang, S., Ding, J., Chang, L., Ren, Q., Li, H., Yang, T., Wu, H., 2019. New geochronologic and paleomagnetic results from early Neoproterozoic mafic sills and late Mesoproterozoic to early Neoproterozoic successions in the eastern North China Craton, and implications for the reconstruction of Rodinia. *Geol. Soc. Am. Bull.* 132, 739–766. <https://doi.org/10.1130/B35198.110.1130/2019298>.
- Zhou, C., Yuan, X., Xiao, S., Chen, Z., Hua, H., 2019. Ediacaran integrative stratigraphy and timescale of China. *Sci. China Earth Sci.* 62, 7–24.
- Zhou, Y., Pogge von Strandmann, P.A.E., Zhu, M., Ling, H., Manning, C., Li, D.a., He, T., Shields, G.A., 2020. Reconstructing Tonian seawater $^{87}\text{Sr}/^{86}\text{Sr}$ using calcite microspar. *Geology* 48 (5), 462–467. <https://doi.org/10.1130/G46756.110.1130/2020125>.
- Zhu, R.-Z., Ni, P., Wang, G.-G., Ding, J.-Y., Fan, M.-S., Ma, Y.-G., 2019. Geochronology, geochemistry and petrogenesis of the Laozhaishan dolerite sills in the southeastern margin of the North China Craton and their geological implication. *Gondwana Res.* 67, 131–146.



A ca. 290 Ma hydrothermal calcite in Cambrian dolostone

Zhongwu Lan^{a,b,c,*}, Shitou Wu^a, Fangyue Wang^d, Bo Liu^e, Kaibo Shi^f, Jing Sun^g, Rong Cao^{a,h}, Xian-Hua Li^{a,h}

^a State Key Laboratory of Lithospheric Evolution, Institute of Geology and Geophysics, Chinese Academy of Sciences, Beijing, 100029, China

^b State Key Laboratory of Palaeobiology and Stratigraphy, Nanjing Institute of Geology and Palaeontology, Chinese Academy of Science, Nanjing, 210008, Jiangsu, China

^c State Key Laboratory of Geological Processes and Mineral Resources, China University of Geosciences, Wuhan, 430074, Hubei, China

^d School of Resources and Environmental Engineering, Hefei University of Technology, Hefei, 230009, Anhui, China

^e Institute of Oil and Gas, Peking University, Beijing, 100871, China

^f School of Earth and Space Sciences, Peking University, Beijing, 100871, China

^g College of Geosciences, China University of Petroleum, Beijing, 102249, China

^h College of Earth and Planetary Sciences, University of Chinese Academy of Sciences, Beijing 100049, China

ARTICLE INFO

Keywords:

Hydrothermal calcite

LA-ICP-MS U–Pb

Tarim basin

Ca. 290 Ma

ABSTRACT

Acquiring the absolute timing for hydrothermal carbonate is a precondition to probing into the basinal-scale, tectonically-driven fluid circulation processes. This study provides an absolute LA-ICP-MS age of ca. 290 Ma from calcite megacrysts within the early Paleozoic dolostones of the Tarim Basin, which corresponds to the timing of Early Permian Large Igneous Province (LIP), which we suggest is genetically linked. The ca. 290 Ma calcite underwent subsequent partial recrystallization or dissolution-precipitation forming younger calcite ages of ca. 250 Ma, consistent with the timing of the Indosinian orogeny. Th/U ratios are demonstrated to be an effective criterion to differentiate domains of primary (ca. 290 Ma) and alteration (ca. 250 Ma) calcite, with the former displaying lower Th/U ratios (0.005–0.05) in comparison to the latter that shows relatively higher Th/U ratios (>0.15). Such differential Th/U ratios may suggest differential involvement of fluids from both within the host dolostones and from magmatic/hydrothermal fluids. This study also demonstrates that Si and Pb preferentially enter into the crystal lattice of calcite to replace Ca via charge balance substitution mechanism. In contrast, U, Sr, Y, La and Ce are mainly concentrated around cleavage planes, cracks and veinlets within calcite.

1. Introduction

Formation of hydrothermal carbonates associated with tectono-magmatic activity has increasingly attracted global attention in recent years (Spencer-Cervato and Mullis, 1992; Nader et al., 2004; Davies and Smith, 2006; Dong et al., 2013; Rochelle-Bates et al., 2021; Cong et al., 2022). These studies have challenged the traditional interpretation of multiple mechanisms of dolomitization in many early Paleozoic deeply buried carbonates reservoirs. Tectono-magmatic activity is not only capable of providing an abnormal heat source inducing thermal baking in carbonates adjacent to the magmatic intrusions, but also can promote migration of hydrothermal fluids from the magmas into the host carbonates along fracture or fault pathways, leading to far field hydrothermal alteration of the carbonate host (Lonnee and Machel, 2006; Dong et al., 2013; Rochelle-Bates et al., 2021). The Tarim Basin is one

such example that hosts pervasive early Paleozoic dolostones within deeply buried Cambrian and Lower Ordovician strata. These strata underwent multiple episodes of complicated diagenetic processes and were potentially influenced by the early Permian extensive magmatism based on petrographic and geochemical evidence (Tian et al., 2010; Yu et al., 2011; Dong et al., 2013; Li et al., 2016; Hu et al., 2020). Ascertaining the absolute timing of these hydrothermal carbonates is a key to understanding the basinal-scale, tectonically-driven hydrothermal fluid circulation processes.

Calcite (CaCO₃) U–Pb geochronology is an emerging technique widely applied to sedimentary geology and petroleum geology to determine the absolute timing of sedimentation, diagenesis and fluid (including hydrocarbon) migration (Rasbury et al., 2020; Roberts et al., 2020; Liivamägi et al., 2021; Lan et al., 2022a, b). The susceptibility of calcite to hydrothermal fluid activities makes it a powerful tool for

* Corresponding author. State Key Laboratory of Lithospheric Evolution, Institute of Geology and Geophysics, Chinese Academy of Sciences, Beijing 100029, China..

E-mail address: lzw1981@126.com (Z. Lan).

<https://doi.org/10.1016/j.marpetgeo.2022.106011>

Received 20 June 2022; Received in revised form 27 October 2022; Accepted 30 October 2022

Available online 2 November 2022

0264-8172/© 2022 Elsevier Ltd. All rights reserved.

dating and characterizing fluid events. Depending on the U/Ca ratios of the fluid and the oxidation state of uranium, calcite may incorporate uranium upon its crystallization. Studies show multiple pathways for uranium incorporation (Rasbury et al., 2020). With the development of *in situ* analytical techniques, traditional measurement of calcite U–Pb ages by bulk dissolution methods have been increasingly superseded with laser ablation LA-ICP-MS, which is capable of quickly finding and analyzing high U/Pb domains that are smaller than the large sample volumes used in ID-TIMS dating (Roberts et al., 2020). As such, LA-ICP-MS is an effective tool for *in situ* calcite geochronology owing to its rapid spot analysis and sufficiently high precision (Roberts et al., 2020).

Recent research shows that fluid influx and alteration and/or recrystallization of primary calcite can disturb the U–Pb isotopic systematics (Roberts et al., 2021; Lan et al., 2022a). Combined cathodoluminescence (CL), back scattered electron (BSE) and trace element mapping techniques reveal structural and chemical information that

bears on the origin (primary or secondary) of dated calcite (Roberts et al., 2020, 2021). Building on these careful studies, we carry out detailed petrography and trace element mapping guided U–Pb geochronology on calcite megacrysts from the Cambrian dolostones in the Tarim Basin to decipher their formation timing and investigate their causal links with large scale Permian magmatism.

2. Geological setting, stratigraphy and sedimentology

Bounded by the Kunlun, Tian Shan and Altyn Tagh mountains, the Tarim Basin is a large complex sedimentary basin made up of a Paleozoic cratonic basin and a Mesozoic–Cenozoic foreland basin (Fig. 1). This NW China basin has undergone multiple stages of tectonic evolution, magmatism and deformation (Kang and Kang, 1994; Tang, 1997). An intra-cratonic extensional basin developed during the Ediacaran–Early Ordovician, followed by the development of an intra-cratonic compressional basin during the Middle Ordovician–Middle Devonian,

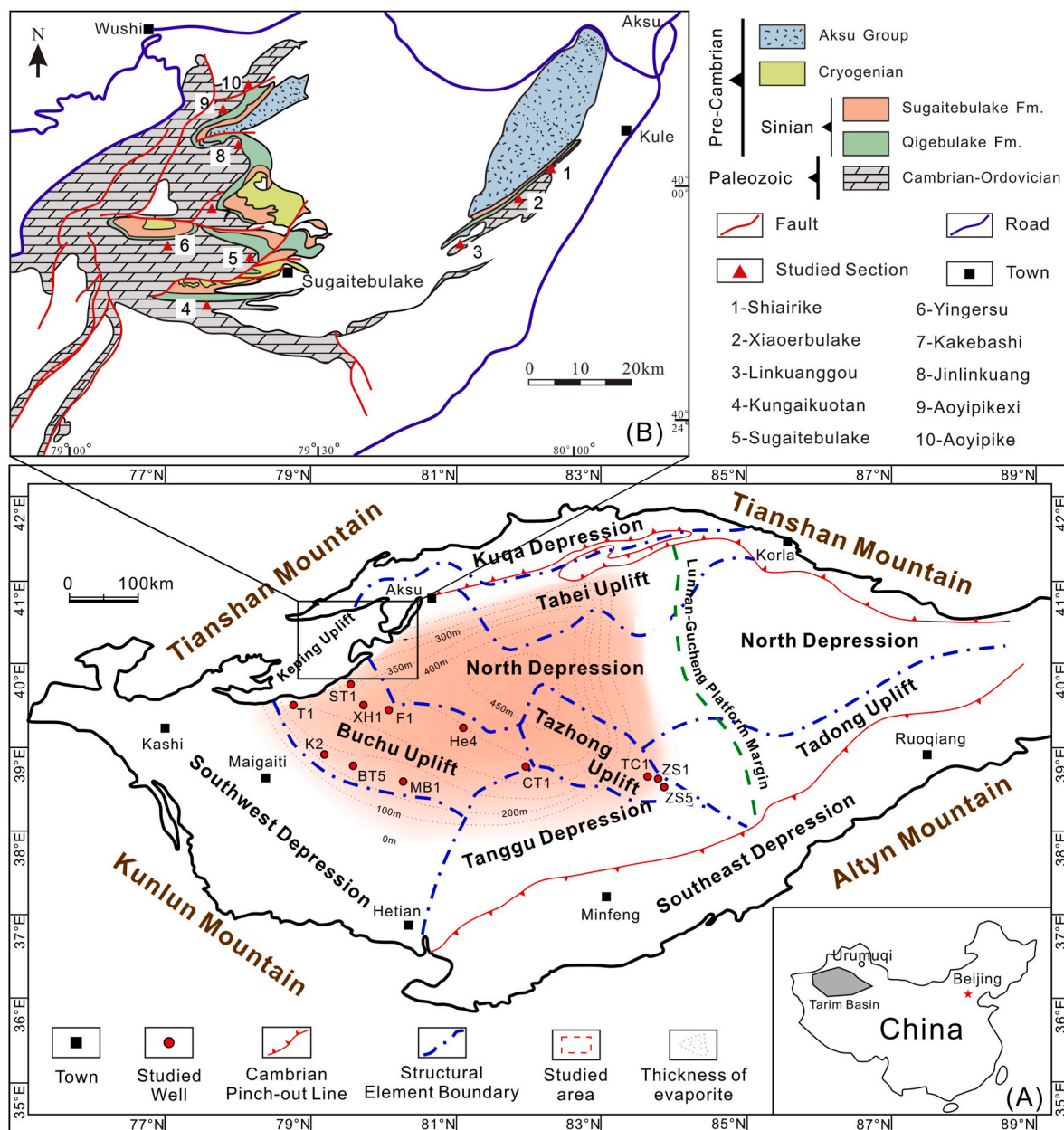


Fig. 1. Geological map and stratigraphy for the Xiaerblak Formation. (A) Simplified geological map displaying dominant lithotectonic zones in the Tarim basin. (B) Generalized stratigraphic column of the Xiaerblak Formation in the Yingsu Section.

and then a back-arc extensional basin during the Late Devonian–Early Permian (Li et al., 2016). During the late Paleozoic to early Mesozoic transition, a retro-arc foreland basin developed, which was followed by a collisional reactivated foreland basin during the Jurassic–Paleogene, and the Indian–Tibetan collisional basin during the Neogene–Quaternary (Tang et al., 2004; Li et al., 2016).

The Tarim Basin was situated in a relatively stable marine carbonate platform which experienced multiple episodes of marine transgression and regression (Cai et al., 2001; Zheng et al., 2007). Shallow marine dolomitized carbonates of up to 2000 m were accumulated during the Cambrian and Ordovician periods (Cai et al., 2001; Shao et al., 2002; Zheng et al., 2007; Dong et al., 2013). The terminal Ordovician carbonate deposition was replaced with siliciclastic deposition, with subsequent persistence of burial because of continuous basin subsidence. During the Permian period, a large igneous province (LIP) accompanied extensive faulting (Yang et al., 2007; Zhang et al., 2008, 2010; Tian et al., 2010; Yu et al., 2011; Dong et al., 2013) that was induced by southward convergent subduction of the Middle Tianshan arc to the north of the Tarim Block (Tang et al., 2004). Basalt and diabase within the LIP yielded a SIMS zircon U–Pb age of ca. 290–288 Ma (Yu et al., 2011; Dong et al., 2013). Recent high resolution CA-ID-TIMS U–Pb dating of interbedded tuff layers constrained occurrence timing of Tarim LIP from 289.77 ± 0.95 Ma to 284.27 ± 0.39 Ma, with an entire eruption duration of ca. 5.5 m.y. (Zhong et al., 2022). Merging of the Middle Tianshan island arc with the Tarim plate during the Late Permian–Early Triassic produced a period of uplift, exhumation and erosion particularly on the northwestern margin of Tarim Block during the amalgamation of Tarim and Siberia blocks (Jia, 1997). The Cenozoic witnessed a strengthening of positive relief along the northwestern margin of Tarim Block with the collision between the Eurasiatic Block and Indian Block, which induced a series of NEE striking and imbricated overthrust nappes such as the Keping uplift as well as exhumation and erosion of Paleozoic rocks throughout the Neogene (Burchfiel et al., 1999; Dong et al., 2013). In contrast, the majority of the plate interior experienced an accelerating subsidence and downwards plunging, which induced the formation of pervasive negative relief of the Tarim Basin bounded by numerous uplifts (Shu et al., 2004; Tang et al., 2004).

Cambrian and Ordovician dolostones underwent multiple episodes of diagenetic and hydrothermal processes (Dong et al., 2013; Li et al., 2016; Hu et al., 2020). Based on trace element, rare earth element (REE), stable isotope data coupled with petrographic analyses, Li et al. (2016) demonstrated an interaction of hydrothermal fluid with formation water that leached the host dolostone and created large volumes of porosity, inducing the formation of vugs- and pore-filling dolomite/calcite. Post-depositional hydrothermal influence was also demonstrated by the occurrence of less radiogenic $^{87}\text{Sr}/^{86}\text{Sr}$ ratios in the vugs- and pore-filling dolomite/calcite (Dong et al., 2013). The Cambrian successions are composed of, in ascending order, the Lower Cambrian Yuertus (E_{1y}), Xiaerbulak (E_{1x}), and Wusongger (E_{1w}) formations, the Middle Cambrian Shayilike (E_{2y}) and Awatage (E_{2a}) formations, and the Upper Cambrian Qiulitage (E_{3q}) Formation. The Lower Cambrian Xiaerbulak Formation (E_{1x}) was targeted on in this study, which is mainly composed of micritic dolostone (Fig. 1). Well-exposed outcrop sections (Shiairike, Xiaerbulake, Linkuanggou, Kungaiquotan, Sugaitetbulake, Yingersu, Kakebashi, Jinlinkuang, Aoyipikexi, and Aoyipike) were chosen to provide a better understanding of relationships between the tectonothermal history and post-depositional dolomitization. Abundant dissolution vugs and cavities filled with calcite, commonly in the size range of 4–9 cm, are present within the lower Xiaerbulak Formation at the Yingersu Section (Fig. 2A–D). Fractures occasionally cross-cut the host micritic dolostone and extend to varying directions constituting network morphology (Fig. 2A–B). Abundant bitumen fills vugs and cavities within the Yuertus and middle-upper Xiaerbulak formations (Fig. 2E–G). Large transparent calcite crystals, commonly 3–5 cm in size, were scooped out from vugs and cavities for LA-ICP-MS U–Pb geochronology (Fig. 2H).

3. Methods

3.1. Imaging analysis

In situ mineral chemistry and calcite geochronology were performed on polished thin-sections. A high spatial resolution scanning electron microscope (Zeiss 1555 VP-FESEM) and a Nikon Eclipse E800 microscope equipped with a Nikon DS-Fi 1 camera based in the State Key Laboratory of Lithospheric Evolution, Institute of Geology and Geophysics, Chinese Academy of Sciences (SKLLE, IGGCAS) were employed for petrographic observation and imaging analyses. An optimal resolution at $38\text{--}803 \times$ magnification, an optimal working distance of 8–10 mm and a voltage of 15 kV were obtained by specifically manipulating the SEM under backscattered electron mode. A cold CL microscope at the Key Lab of Petroleum Resources at IGGCAS was employed to acquire CL images of carbonates, with a beam diameter of 4 mm, a beam voltage of 15 kV, and a current of 325 μA .

3.2. LA-ICP-MS mapping

LA-ICP-MS mapping was performed at the Ore Deposit and Exploration Centre (ODEC), School of Resources and Environmental Engineering, Hefei University of Technology, using a laser ablation system (Photon Machines Analyte HE with 193-nm ArF Excimer), coupled to a quadrupole-based inductively coupled plasma-mass spectrometer (ICP-MS) (Agilent 7900) (Ning et al., 2017). The Analyte HE utilizes a two-volume ablation cell designed by Laurin Technic Pty. Ablation was performed in an atmosphere of UHP He (0.9 L/min), and the aerosol is mixed with Ar (0.87 L/min) immediately upon exiting the ablation cell via a T-connector before entering the ICP. In addition, for high resolution profiling, the signal-smoothing device, which is used for routine analysis, is removed, providing an almost instantaneous response time. The ICP-MS system was optimized daily to maximize sensitivity on isotopes of the mass range of interest, while keeping production of molecular oxide species (i.e., $^{232}\text{Th}^{16}\text{O}/^{232}\text{Th}$) as low as possible, and usually $<0.3\%$. Element maps were created by ablating sets of parallel line raster in a grid across the sample. A beam size of 40 μm and scan speeds of 40 $\mu\text{m}/\text{s}$ (equal to beam size) was chosen in this study. A laser repetition of 7 Hz was selected at a constant energy output in an energy density of $\sim 2.5 \text{ J}/\text{cm}^2$ at the target. A 20 s background acquisition was acquired at the start of scanning, and to allow for cell wash-out, gas stabilization, and computer processing, a delay of 20 s was used after ablation. Reference materials NIST 612 and NIST 614 at the start and end of each mapping was analyzed for data calibration. Images were compiled and processed using the program LIMS2.0 (Wang et al., 2017; Xiao et al., 2018). For each raster and every element, the average background was subtracted from its corresponding raster, and the raster was compiled into a 2-D image displaying combined background/drift corrected intensity for each element (Wang et al., 2017).

3.3. Calcite U–Pb dating

Analytical procedures and instrumental configuration for calcite U–Pb geochronology are only briefly summarized herein. For analytical details refer to Wu et al. (2022) and Lan et al. (2022b). *In situ* calcite LA-ICP-MS U–Pb dating was carried out on polished thin sections via a PhotoMachine Analyst G2 laser ablation system (Teledyne CETAC, Omaha, USA) coupled to an Element XR (Thermo Fisher Scientific, Bremen, Germany) at SKLLE, IGGCAS. A T junction was employed to add N_2 into the Ar sample gas flow behind the ablation cell, whereas the guard electrode was utilized to improve sensitivity (Wu et al., 2020a,b).

Prior to *in situ* U–Pb spot dating analysis, a blind spot analysis was conducted using a laser beam of 80–100 μm to locate high uranium regions. Detection of the signals of ^{202}Hg , $^{204}(\text{Hg} + \text{Pb})$, ^{206}Pb , ^{207}Pb , ^{208}Pb , ^{232}Th and ^{238}U was achieved in a peak jumping mode with a total integration time of 0.30 s to produce 130 mass scans during the data

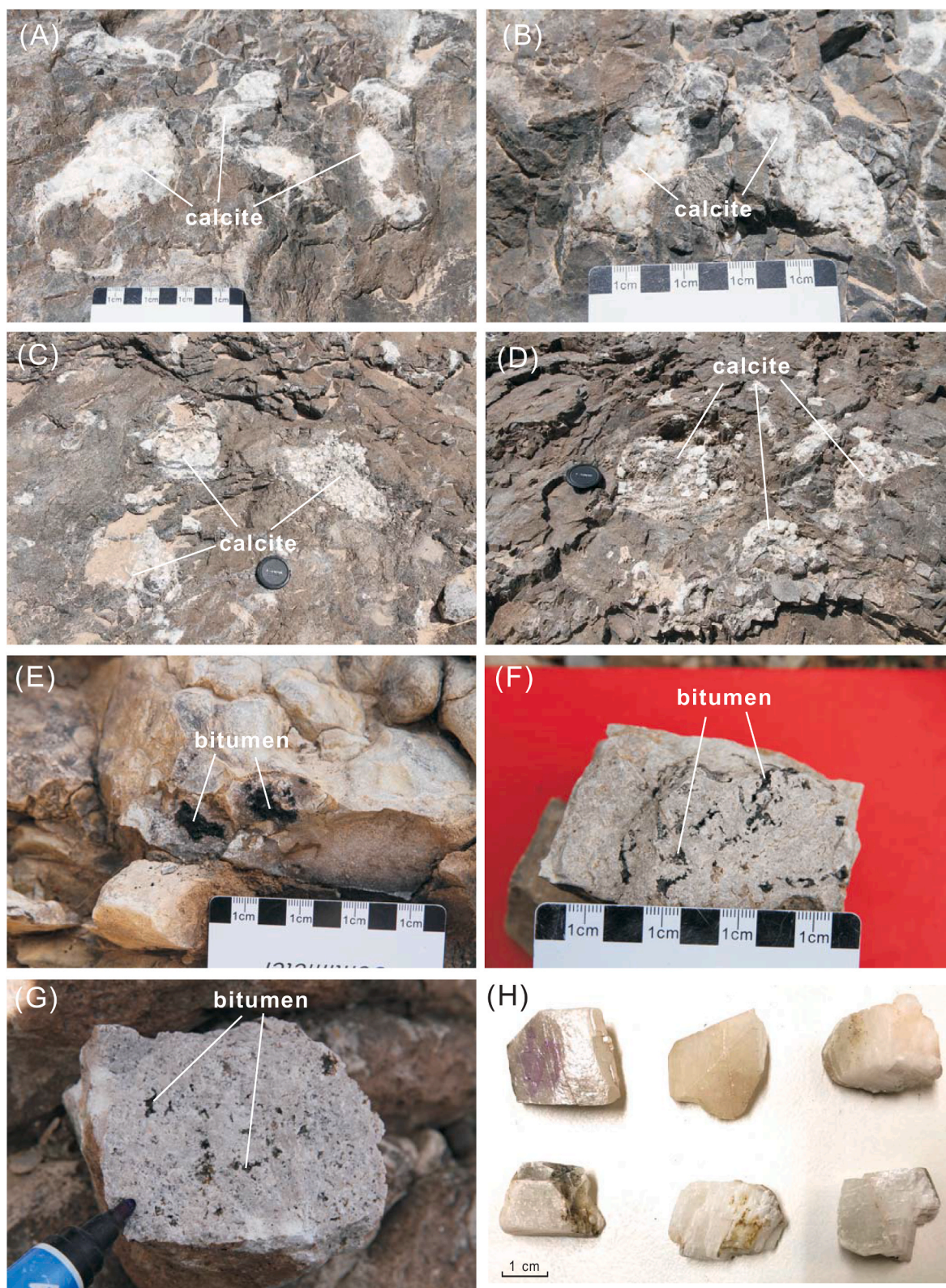


Fig. 2. Field photos showing the occurrence of vug- and pore-filling calcite and bitumen in the Yuertus and Xiaerblak formations. (A)–(D) Field outcrops showing the presence of abundant whitish to pale grey calcite crystals commonly in the size range of 5–10 cm infilling the pores/cavities within the dolomite of the Xiaerblak Formation. (E) Bitumen within carbonates from upper Yuertusi Formation which immediately underlies the Xiaerblak Formation. (F) Bitumen within carbonates from the middle Xiaerblak Formation. (G) Bitumen within carbonates from the middle-upper Xiaerblak Formation. (H) Large calcite crystals dug out from pores/cavities of the lower Xiaerblak Formation.

acquisition. Four reference materials (RMs) were employed including two calcite U–Pb reference materials WC-1 and Duff Brown Tank (Hill et al., 2016; Roberts et al., 2017) for calibration of U/Pb ratios and two glass reference materials ARM-3 and NIST SRM 614 (Woodhead and Hergt, 2001; Wu et al., 2021) for calibration of Pb/Pb ratios.

A total of six regions were chosen from a large calcite crystal for U–Pb geochronology, with 40 spot analyses carried out on each selected domain. During the course of this study, a total of 48 analyses were conducted on Duff Brown Tank, which yielded a U–Pb age of 64.26 ± 0.65 Ma (MSWD = 2.3; $n = 48$) consistent with the published isotope dilution age of 64.04 ± 0.67 Ma (Hill et al., 2016). The method described by Wu et al. (2022) was adopted for data reduction. Raw data (time-resolved intensities) were reduced using the Iolite 3.7 data reduction software and the VizualAge data reduction scheme from the ICP-MS (Paton et al., 2011; Petrus and Kamber, 2012). Matrix induced mass bias in $^{238}\text{U}/^{206}\text{Pb}$ ratios between RMs and unknown samples were calibrated using WC-1 (Roberts et al., 2017) and was accomplished in Microsoft Excel. The uncertainty propagation of LA-ICP-MS calcite geochronology is a modified approach based upon Lan et al. (2022a), wherein the final age is quoted without and with systematic uncertainties, as $\pm \alpha/\beta$, respectively.

4. Results

4.1. Petrography

Most of domains in the calcite crystals have smooth surface and distinct growth zones (Figs. 3–7). Cleavage planes, cracks and/or veinlets with a width of 3–10 μm have relatively bright CL color. The cleavage planes and veinlets commonly display parallel alignment, whereas cracks are not aligned (Fig. 4b; Fig. 5e; Fig. 7b). In Domain 1, veinlets are common with a distance of 250–300 μm (Fig. 4b). Dolomite remnants in the size range of 10–30 μm are occasionally present, and have relatively dark CL color in comparison to calcite matrix (e.g. Fig. 3c).

4.2. Trace element mapping

Sr, Y, La and Ce commonly show broadly correlative enrichment and depletion across the six domains, whereas Eu, Tm and Yb display broadly correlative enrichment and depletion (Figs. S1–S6). LREEs such as La and Ce display strong signals in comparison to MREEs such as Eu and HREEs such as Tm and Yb (Figs. S1–S6). All Domains show similar

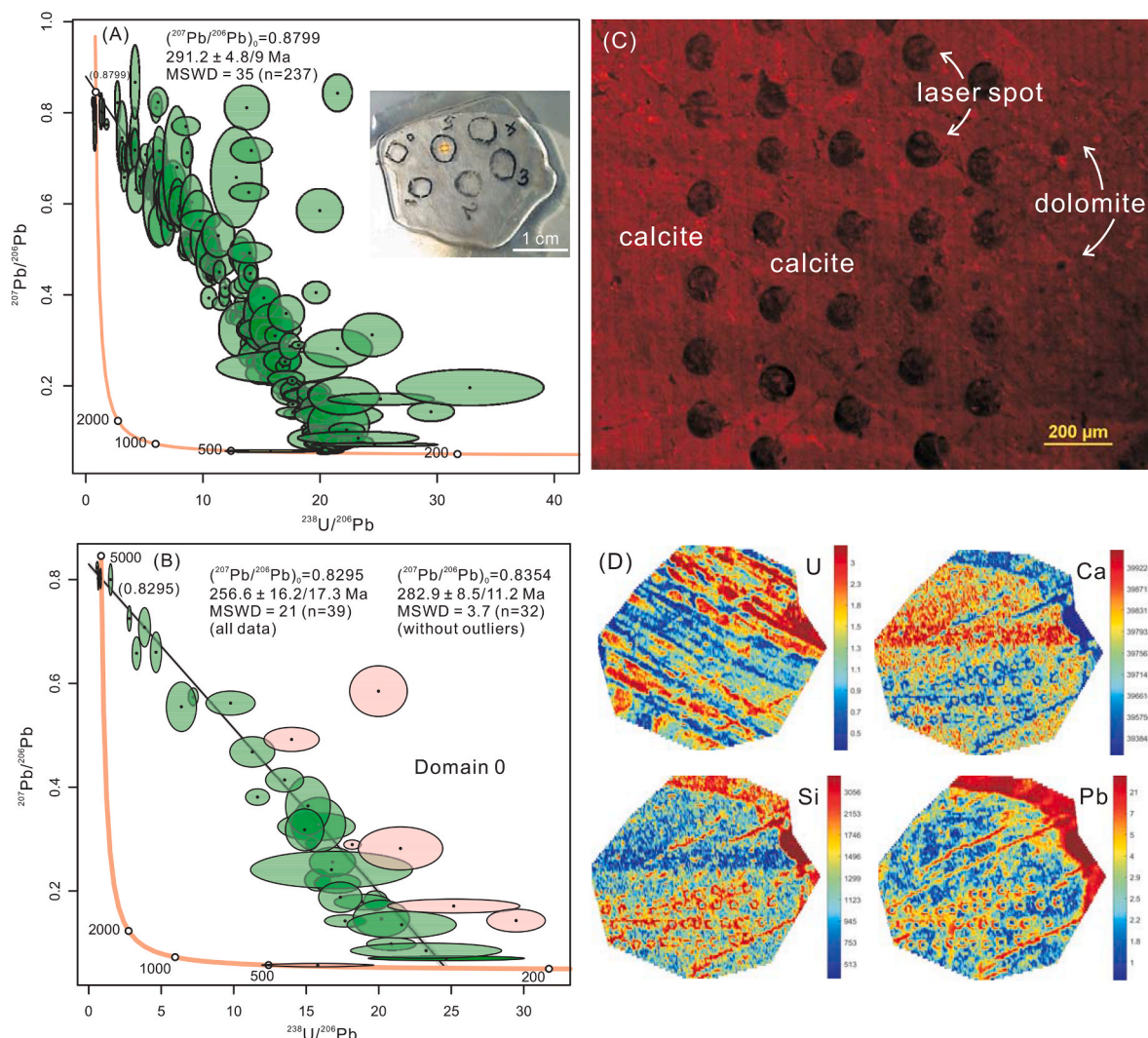


Fig. 3. Tera-Wasserburg plot for all dated domains (A). Uncertainties are plotted and quoted at 2σ as $\pm \alpha/\beta$, where α and β are without and with systematic uncertainty propagation, respectively. Note a total of six domains (Domain 0, Domain 1, Domain 2, Domain 3, Domain 4, and Domain 5) are analyzed in the calcite megacryst. (B) Tera-Wasserburg plot for Domain 0. Filled pink colours are outliers. (C) CL image for Domain 0. Note the presence of fine-grained dolomite remnants. (D) LA-ICP-MS trace element maps for Domain 0 where Si and Pb exhibit similar enrichment and depletion in contrast to Ca. (For interpretation of the references to colour in this figure legend, the reader is referred to the Web version of this article.)

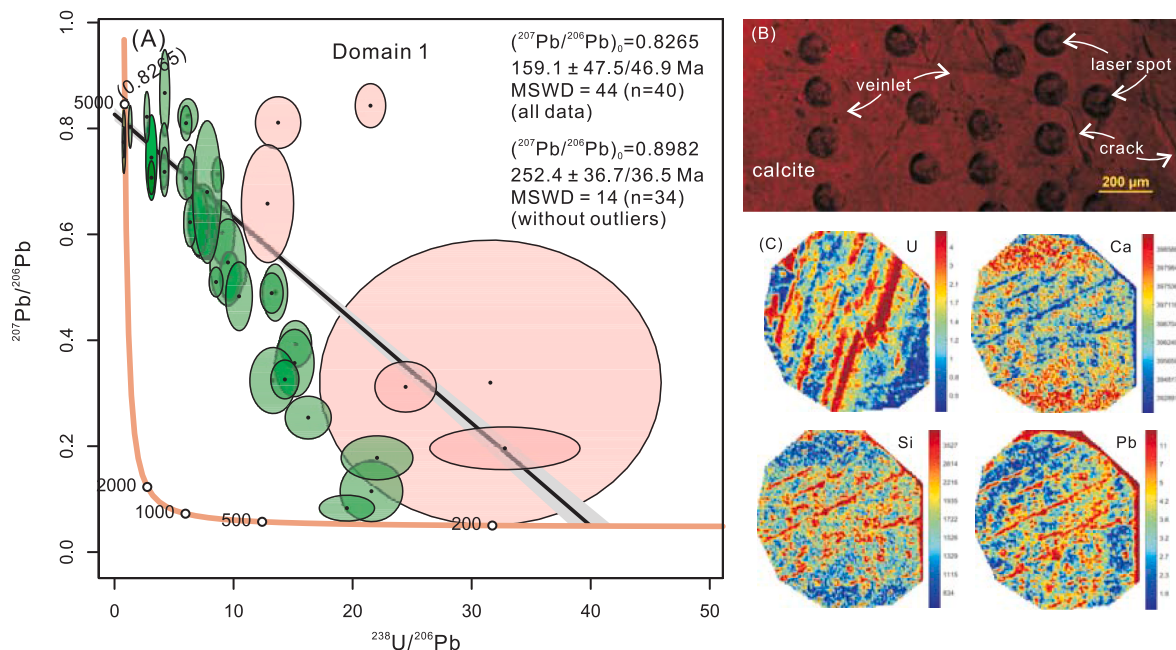


Fig. 4. Calcite geochronology and petrography for Domain 1. (A) Tera–Wasserburg plot for Domain 1. Filled pink colours are outliers. (B) CL image for Domain 1, where veinlets and cracks are clearly displayed. (C) LA-ICP-MS trace element maps for Domain 1 where Si and Pb show similar enrichment and depletion in contrast to Ca. Note enrichment of Si and Pb along cleavage planes that are suggestive of hydrothermal fluid activities. (For interpretation of the references to colour in this figure legend, the reader is referred to the Web version of this article.)

enrichment and depletion of Si and Pb, which are in sharp contrast to Ca (Figs. 3–7). U distribution shows no obvious correlations with other elements (Figs. 3–7). Signals of U, Sr, Y, La and Ce are more pronounced around cleavage planes or cracks or veinlets.

4.3. LA-ICP-MS calcite U–Pb age

A compilation of all LA-ICP-MS U–Pb data that is composed of spot traverses across all six domains recognized by petrography and trace element mapping is tabulated in [Supplementary Table 1](#) and is displayed in Figs. 3–7. Forty spot analyses were conducted in each textural domain within the calcite megacryst, resulting in a total of 240 analyses. All data demonstrates a very consistent population of data yielding an upper intercept $^{207}\text{Pb}/^{206}\text{Pb}$ ratio of 0.8799 and a lower intercept $^{206}\text{Pb}/^{238}\text{U}$ age of 291.2 ± 9 Ma with a MSWD of 35 (Fig. 3A). Several outliers deviate from this trend, and scatter to the right side of the discordia line between the high initial lead and radiogenic lead of the array. Domain 0 produces an upper intercept $^{207}\text{Pb}/^{206}\text{Pb}$ ratio of 0.8295 and a lower intercept age of 256.6 ± 17.3 Ma, with a MSWD of 21 (Fig. 3B). Removing seven outliers gets an upper intercept $^{207}\text{Pb}/^{206}\text{Pb}$ ratio of 0.8354 and a lower intercept age of 282.9 ± 11.2 Ma, with a MSWD of 3.7 (Fig. 3B).

Domain 1 yields an upper intercept $^{207}\text{Pb}/^{206}\text{Pb}$ ratio of 0.8265 and a lower intercept age of 159.1 ± 46.9 Ma, with variable degrees of scatter and a MSWD of 44 (Fig. 4A). Removing six distinct outliers improves this marginally to 252.4 ± 36.5 Ma, with a MSWD of 14. Domain 2 displays a very consistent population of data producing an upper intercept $^{207}\text{Pb}/^{206}\text{Pb}$ ratio of 0.8504 and a lower intercept age of 294.9 ± 9.7 Ma, with a MSWD of 1.6 (Fig. 5A). Likewise, Domain 3 also displays a very consistent population of data producing an upper intercept $^{207}\text{Pb}/^{206}\text{Pb}$ ratio of 0.8652 and a lower intercept age of 302.0 ± 9.4 Ma, with a MSWD of 2.7 (Fig. 5D). Domain 4 produces an upper intercept $^{207}\text{Pb}/^{206}\text{Pb}$ ratio of 0.8628 and a lower intercept age of 290.7 ± 8.7 Ma, with a MSWD of 9.7 (Fig. 6A). Removing three outliers gives an upper intercept $^{207}\text{Pb}/^{206}\text{Pb}$ ratio of 0.8594 and a lower intercept age of 292.1 ± 8.5 Ma, with a MSWD of 6.3. Domain 5 yields an upper intercept $^{207}\text{Pb}/^{206}\text{Pb}$ ratio of 0.9138 and a lower intercept age of 279.4 ± 27.7

Ma, with a MSWD of 47 (Fig. 7A). Removing five distinct outliers gets an upper intercept $^{207}\text{Pb}/^{206}\text{Pb}$ ratio of 0.8485 and a lower intercept age of 292.2 ± 11.5 Ma, with a MSWD of 4.7.

The Th/U ratio of the domains is indicative of different fluids as they display distinctly different ratios (Fig. 8). Domain 0 and Domain 2–5 have Th/U ratios that are dominated in the range of 0.005–0.05, whereas Domain 1 has Th/U ratios >0.15 .

5. Discussion

5.1. Primary or secondary ages?

The sample C4A displays very consistent U–Pb age systematics across six dated domains, as demonstrated in Fig. 3A. A distinct pattern appears when each domain was considered separately with a main age of ca. 280–290 Ma. Disturbed isotope systematics occur to varying extent in some domains, particularly in Domain 1, as demonstrated by outliers away from the regression line. Domain 2 and Domain 3 yield overlapping ages without disturbance. Domain 0, Domain 4 and Domain 5 produce overlapping ages with only minor disturbance. Of these, data-points that show a sub-horizontal trend with high $^{207}\text{Pb}/^{206}\text{Pb}$ ratios possibly suggest U addition, whereas those producing low $^{207}\text{Pb}/^{206}\text{Pb}$ and ^{238}U – ^{206}Pb ratios likely point to U loss (c.f. Roberts et al., 2020). Domain 1 displays elevated U/Pb ratios resulting in an obviously younger lower intercept age, the isotope systems of which is possibly associated with younger growth or hydrothermal alteration. Given that Domain 1 possibly represents recrystallization or dissolution and re-precipitation of an antecedent texture, the data is interpreted to indicate disturbance of the U–Pb system.

Trace element data have been used to distinguish domains of alteration and primary calcite, but the criterion is not universally applicable as fluid resetting and fluid-driven recrystallization will induce elemental mobility to varying extent (Roberts et al., 2020, 2021; Simpson et al., 2021). In contrast, the differential Th/U ratio within variously dated domains potentially suggests origination of fluids from different sources to have precipitated calcite cements/crystals, particularly in Domain 1 (Fig. 8). Thorium and uranium are highly incompatible elements that

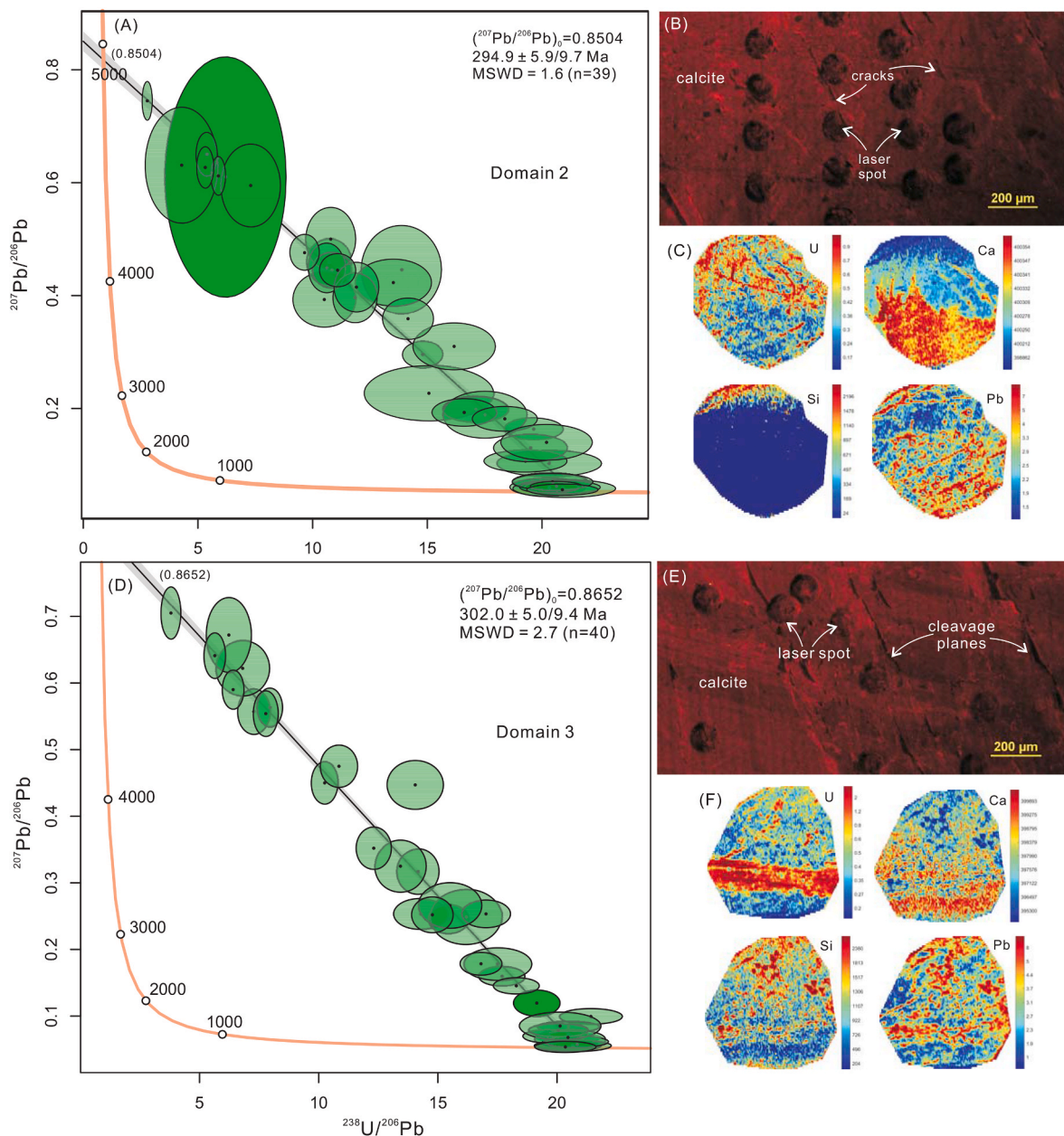


Fig. 5. Calcite geochronology and petrography for Domain 2 & 3. (A) Tera–Wasserburg plot for Domain 2. (B) CL image for Domain 2. Cracks are present in varying directions. (C) LA-ICP-MS trace element maps for Domain 2 where Si and Pb show similar enrichment and depletion in contrast to Ca. (D) Tera–Wasserburg plot for Domain 3. (E) CL image for Domain 3. Note near parallel alignment of cleavage planes. (F) LA-ICP-MS trace element maps for Domain 3 where Si and Pb show similar enrichment and depletion in contrast to Ca.

are commonly coupled with each other in magmatic/hydrothermal process in comparison to supergene processes where they display differential behaviors (Liu et al., 2019), yielding differential Th/U ratios in magmatic/hydrothermal and deposition/diagenetic processes (Hazen et al., 2009). In this regard, it is inferred that calcite in Domain 0 and Domain 2–5 (Th/U ratios of 0.005–0.05) was mainly formed via fluid cannibalization and migration from host dolostones, whereas calcite in Domain 1 (Th/U > 0.15) was dominantly precipitated from magmatic/hydrothermal fluids, which was possibly induced by the Early Permian large scale basic magmatic emplacement (Dong et al., 2013). In comparison to their sedimentary/diagenetic counterparts, calcite precipitated in hydrothermal fluids typically has a LREE-enrichment with positive Eu anomalies (Dekov et al., 2014; Zhang et al., 2014). The six domains show striking LREE enrichment in comparison to MREE and HREE (Figs. S1–S6), which is also consistent with a hydrothermal

origin. As such, we are confident to interpret Domain 1 (ca. 250 Ma) represents dominantly magmatic/hydrothermal fluid influenced mobilization of U and Pb isotopes, whereas Domain 0 and Domain 2–5 (ca. 290 Ma) represent a dominantly magmatic intrusion driven fluid circulation within the host dolostones; meteoric waters penetrated downward and circulated into the host dolostones driven by magmatic intrusion related thermal baking.

Si and Pb show similar enrichment and depletion across the six domains. Pb has slightly larger ionic radii of 1.19 Å in comparison to Ca (1.0 Å), thus only inducing less dilation of the local environment around Pb (Reeder et al., 1999). Si has a much smaller ionic radii of (0.4 Å) in comparison to Ca (1.0 Å) (Shannon, 1976), and thus should readily enter into the crystal lattice of calcite without causing obvious dilation. Nanoscale replacement of calcite by quartz provides a possible mechanism to explain the strong positive correlations between Si and Pb and

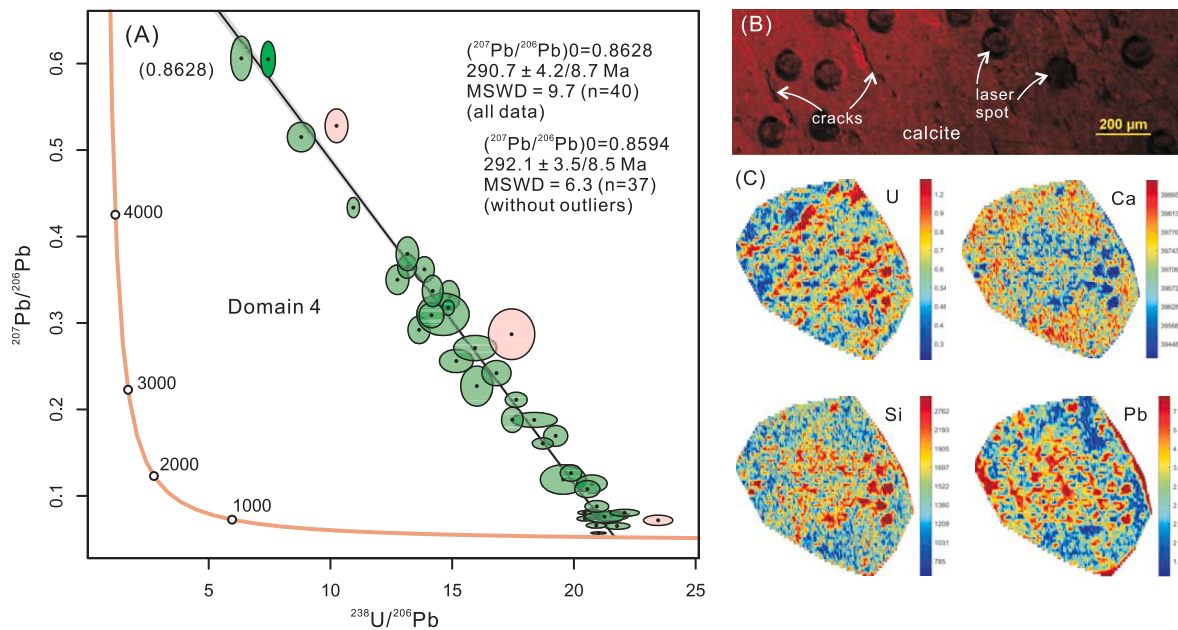


Fig. 6. Calcite geochronology and petrography for Domain 4. (A) Tera-Wasserburg plot for Domain 4. Filled pink colours are outliers. (B) CL image for Domain 4. Cracks of variable width are present. (C) LA-ICP-MS trace element maps for Domain 4 where Si and Pb show similar enrichment and depletion in contrast to Ca. (For interpretation of the references to colour in this figure legend, the reader is referred to the Web version of this article.)

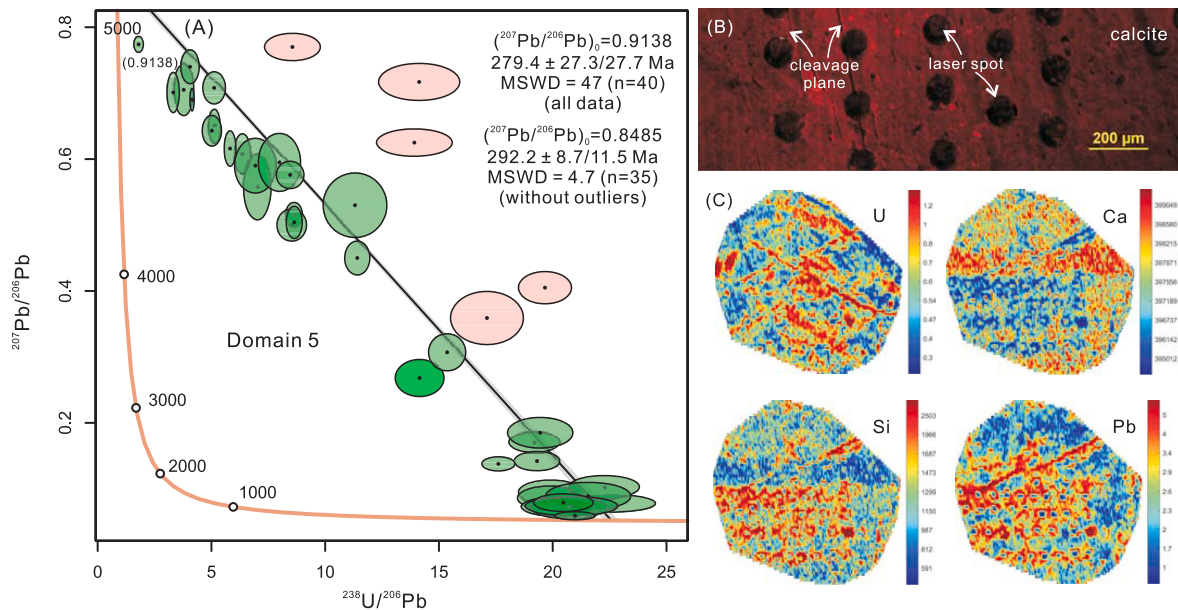


Fig. 7. Calcite geochronology and petrography for Domain 5. (A) Tera-Wasserburg plot for Domain 5. Filled pink colours are outliers. (B) CL image for Domain 5. Cleavage planes are present crosscutting the laser spot positions. (C) LA-ICP-MS trace element maps for Domain 5 where Si and Pb show similar enrichment and depletion in contrast to Ca. Note enrichment of Si and Pb along cleavage plane, indicating hydrothermal fluid activities. (For interpretation of the references to colour in this figure legend, the reader is referred to the Web version of this article.)

their negative correlations with Ca. The higher abundance of Si is a straightforward indication of enrichment of Si in fluids, as demonstrated by the precipitation of fine-grained authigenic quartz which should have dominantly sourced from hydrothermal fluids (Li et al., 2016). A combined x-ray absorption spectroscopy and x-ray fluorescence microprobe analyses demonstrate that under reducing conditions U^{4+} substitutes for Ca^{2+} possibly by means of $3Ca^{2+} \rightarrow U^{4+} + 2Na^{+}$ to make it occupy a stable crystal lattice site in calcite (Sturchio et al., 1998). Alternatively, a linear uranyl (UO_2^{2+}) moiety may have been incorporated at the Ca^{2+} site in calcite which distinguishes from Ca^{2+} cation in terms of size and morphology (Kelly et al., 2006). No correlations exist between U/Sr and

Ca concentration in trace element mappings across the six domains (Figs. S1–S6). This means U probably travels with oxygen as uranyl which makes it an awkward fit. Alternatively, U and Sr possibly occupy crystal lattice defect or cleavage plane site rather than growth zones in our calcite (c.f. Roberts et al., 2020).

5.2. A ca. 290 Ma hydrothermal carbonate

Dolostones from the Lower Paleozoic Cambrian and Ordovician strata in the Tarim Basin have been commonly associated with multiple mechanisms of dolomitization, with only a few studies mentioning

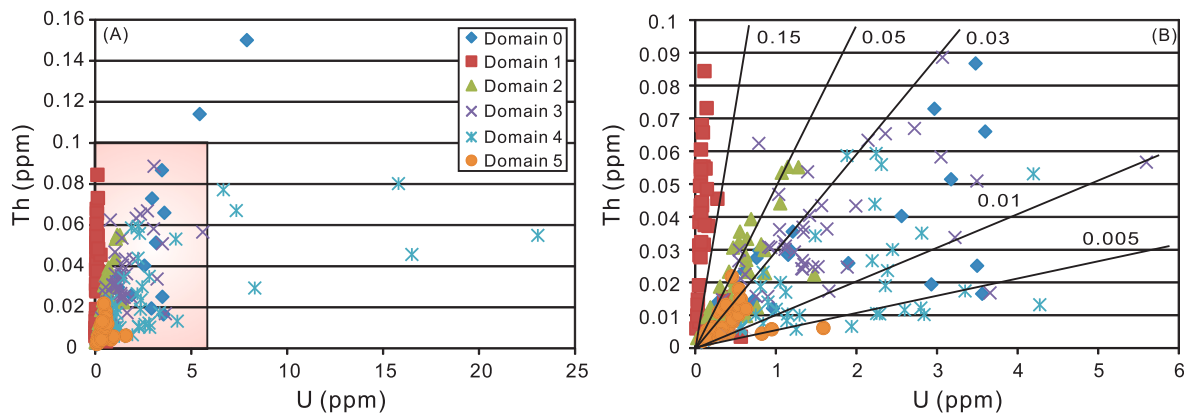


Fig. 8. Th/U ratios for different domains within the calcite megacryst, which are dominated in the range of 0.005–0.05. Note Domain 1 differs from other domains by its striking high Th/U ratios, mainly >0.15. (B) is close-up of the pink rectangular region in (A). Sample symbols in (A) also apply to (B). (For interpretation of the references to colour in this figure legend, the reader is referred to the Web version of this article.)

hydrothermal influences (Dong et al., 2013; Li et al., 2016). Linking post-depositional dolomitization with tectonothermal events have been recently demonstrated by carbonate LA-ICP-MS U–Pb geochronology on dolomite and calcite filling in vugs and pores (Hu et al., 2020); mainly during the early-middle Caledonian (ca. 460–400 Ma) and Indosinian (ca. 250–190 Ma) when fractures formed functioning as the pathways for hydrothermal migration. Hu et al. (2020) obtained dolomite LA-ICP-MS U–Pb ages of 491.6 ± 9.2 Ma to 488 ± 24 Ma from the host dolostone within the Xiaerbulake Formation, which was interpreted to represent the timing of dolomitization. In addition, calcite and dolomite filling primary vugs yielded LA-ICP-MS U–Pb ages of 486 ± 23 Ma to 476 ± 13 Ma, whereas dolomite/calcite filling pores/cracks produced LA-ICP-MS U–Pb ages of 471 ± 10 Ma to 204 ± 37 Ma (Hu et al., 2020). Collectively, these carbonate U–Pb ages demonstrate the occurrence of post-depositional dolomitization during the early-middle Caledonian (ca. 460–400 Ma) and Indosinian (ca. 250–190 Ma) when fractures provide conduits for fluid migration that induced the formation of carbonate cements in the vugs and pores (Hu et al., 2020).

Within analytical errors, none of the calcite U–Pb ages reported by Hu et al. (2020) correspond to the timing of Early Permian LIP in Tarim Basin, which yielded zircon CA-ID-TIMS U–Pb ages of 289.77 ± 0.95 Ma to 284.27 ± 0.39 Ma from interbedded tuff layers, constraining the entire eruption duration of basalt to be ca. 5.5 m.y. (Zhong et al., 2022). Initial petrographic and geochemical studies suggest a possible link between the diagenesis and porosity evolution history of the early Paleozoic dolomite reservoir and Permian LIP, although direct geochronological evidence is lacking (Dong et al., 2013; Li et al., 2016). The calcite U–Pb age of 291.2 ± 9 Ma in this study is within errors consistent with the timing of Early Permian LIP and calcite LA-ICP-MS U–Pb age of 294–262 Ma from the ultra-deep Ordovician reservoirs in the Halahatang oilfield, Tarim Basin (Cong et al., 2022), thus providing a direct absolute age constraint to support the causal relationships between post-depositional dolomitization and Early Permian LIP.

The large scale magmatic activities could have induced a thermal anomaly and fracturing in the sedimentary successions and promoted hydrothermal fluid migration via fracture/fault systems. These fluids may have triggered initial dolomite dissolution followed by calcite/dolomite precipitation and simultaneous recrystallization of matrix dolomite in the host dolostone (Dong et al., 2013; Li et al., 2016), thereby decreasing the effective porosities (Hu et al., 2020). The Early Permian LIP-induced hydrothermal fluids not only triggered the precipitation of calcite/dolomite in vugs and pores, but also probably promoted hydrocarbon migration and charge along the faults and cracks, as evidenced by the occurrence of abundant bitumen (Fig. 2). Such causal links need to be confirmed by further Re–Os dating on the vug- and pore filling bitumen, given that Caledonian (ca. 460–400 Ma)

and Indosinian (ca. 250–190 Ma) tectono-magmatism occurred also around the study area (Hu et al., 2020).

5.3. Implications for dating calcite crystals

U–Pb calcite geochronology is an emerging tool to obtain the absolute timing in various geoscience disciplines (Roberts et al., 2020, 2021; Lan et al., 2022a,b). In this study, we demonstrate that with the aid of CL imaging, trace element mapping and Th/U ratios, a robust interpretation on carbonate geochronology is feasible. In particular, Th/U ratios seem to be a more efficient tool for us to identify zones of alteration and primary calcite in the Tarim basin, which is expected to apply to other basins. As proposed by Roberts et al. (2021), single calcite dates should be treated with caution as they could simply indicate isotope mobility and an apparent age; robust overlapping ages from multiple domains should be acquired in order to produce reliable absolute radiometric dates for various geological events.

6. Conclusions

Tectono-magmatic activity induced formation of hydrothermal carbonates continues to attract worldwide attentions because it challenged the traditional interpretation of multiple mechanisms of dolomitization in many early Paleozoic deeply buried carbonates being targeted as the potential reservoir. The Tarim Basin hosts abundant early Paleozoic dolostones that underwent multiple episodes of complicated diagenetic processes and was potentially influenced by the early Permian extensive magmatism. Acquiring formation age of these hydrothermal carbonates is important for us to understand basinal-scale, tectonically-driven hydrothermal fluid circulation processes. By means of calcite U–Pb geochronology, this study provides an age of ca. 290 Ma from hydrothermal carbonate within the early Paleozoic dolostones of the Tarim Basin, which are consistent with the timing of Early Permian LIP. New ages suggest possible genetic links between the formation of hydrothermal carbonates and Early Permian LIP in the Tarim Basin. The Early Permian magmatic-driven fluid circulation induced the dissolution of host dolostone and formed abundant vugs, pores and cracks that were subsequently filled by calcite crystals/cements. These early formed calcite crystals/cements underwent partial hydrothermal alteration during the Indosinian orogenic event, which disturbed the U–Pb isotope system, forming calcite cements of ca. 250 Ma corresponding to Indosinian period.

Aside from calcite U–Pb geochronology, this study also conducted detailed *in situ* geochemical analyses to further distinguish different generations of calcite, as demonstrated by different age and chemical domains in the early Paleozoic strata of Tarim Basin. Specifically, the

primary calcite (ca. 290 Ma) is characterized by lower Th/U ratios of 0.005–0.05 in comparison to the secondary calcite that is typical of higher Th/U ratios of >0.15. This differentiation criterion is expected to be applicable to other basins given the readily mobility of U and Pb in calcite U–Pb system. Trace element mapping demonstrates that the Tarim hydrothermal calcite displays enrichment in LREEs such as La and Ce in comparison to MREEs such as Eu and HREEs such as Tm and Yb. Trace element mapping also reveals that Si and Pb preferentially enter into the crystal lattice of calcite to replace Ca via charge balance substitution mechanism, whereas U, Sr, Y, La and Ce are mainly concentrated around cleavage planes, cracks and veinlets within calcite.

Declaration of competing interest

The authors declare that they have no known competing financial interests or personal relationships that could have appeared to influence the work reported in this paper.

Data availability

Data will be made available on request.

Acknowledgments

Troy Rasbury was thanked for reading the draft of manuscript and making edits and constructive comments. We are indebted to two anonymous reviewers for their constructive reviews which significantly improved the quality of this manuscript. This project was funded by National Key Research and Development Program of China (2018YFA0702600), the National Science Foundation of China (U19B6003, 41873034, 41673016), Petro China Open Fund (2022-KFKT-07), State Key Laboratory of Lithospheric Evolution, Institute of Geology and Geophysics, Chinese Academy of Sciences (grant SKLZ202001), State Key Laboratory of Geological Processes and Mineral Resources, China University of Geosciences (grant GPMR201902), and State Key Laboratory of Palaeobiology and Stratigraphy, Nanjing Institute of Geology and Palaeontology, Chinese Academy of Sciences (grant 193112).

Appendix A. Supplementary data

Supplementary data to this article can be found online at <https://doi.org/10.1016/j.marpetgeo.2022.106011>.

References

- Burchfiel, B.C., Brown, E.T., Deng, Q., Feng, X., Li, J., Molnar, P., Shi, J., Wu, Z., You, H., 1999. Crustal shortening on the margins of the Tien Shan, Xinjiang, China. *Int. Geol. Rev.* 41, 665–700.
- Cai, C.F., Hu, W.S., Worden, R.H., 2001. Thermochemical sulphate reduction in cambro-ordovician carbonates in central Tarim. *Mar. Petrol. Geol.* 18, 729–741.
- Cong, F.Y., Tian, J.Q., Hao, F., Kylander-Clark, A.R.C., Pan, W.Q., Zhang, B.S., 2022. Calcite U–Pb ages constrain petroleum migration pathways in tectonic complex basins. *Geology*. <https://doi.org/10.1130/G49750.1>.
- Davies, G.R., Smith Jr., L.B., 2006. Structurally controlled hydrothermal dolomite reservoir facies: an overview. *AAPG (Am. Assoc. Pet. Geol.) Bull.* 90, 1641–1690.
- Dekov, V.M., Egueh, N.M., Kamenov, G.D., Bayon, G., Lalonde, S.V., Schmidt, M., Liebetrau, V., Munnik, F., Fouquet, Y., Tanimizu, M., Awaleh, M.O., Guirreh, I., Le Gall, B., 2014. Hydrothermal carbonate chimneys from a continental rift (Afar Rift): mineralogy, geochemistry, and mode of formation. *Chem. Geol.* 387, 87–100.
- Dong, S.F., Chen, D.Z., Qing, H., Zhou, X., Wang, D., Guo, Z., Jiang, M., Qian, Y., 2013. Hydrothermal alteration of dolostones in the Lower Ordovician, Tarim Basin, NW China: multiple constraints from petrology, isotope geochemistry and fluid inclusion microthermometry. *Mar. Petrol. Geol.* 46, 270–286.
- Hazen, R.M., Ewing, R.C., Sverjensky, D.A., 2009. Evolution of uranium and thorium minerals. *Am. Mineral.* 94, 1293–1311.
- Hill, C.A., Polyak, V.J., Asmerom, Y., Provencio, P., 2016. Constraints on a Late Cretaceous uplift, denudation, and incision of the Grand Canyon region, southwestern Colorado Plateau, USA, from U–Pb dating of lacustrine limestone. *Tectonics* 35, 896–906.
- Hu, A.P., Shen, A.J., Liang, F., Zhao, J.X., Luo, X.Y., Feng, Y.X., Cheng, T., 2020. Application of laser in-situ U–Pb dating to reconstruct the reservoir porosity evolution in the Cambrian Xiaerbulake Formation, Tarim Basin. *Oil Gas Geol.* 41, 37–49 (in Chinese with English Abstract).
- Jia, C., 1997. Tectonic Characteristics and Petroleum, Tarim Basin. Petroleum Industry Press, China (in Chinese).
- Kang, Y., Kang, Z., 1994. Tectonic evolution and oil and gas of Tarim Basin. *Acta Geosci. Sin.* 2, 180–191 (in Chinese with English abstract).
- Kelly, S.D., Rasbury, E.T., Chattopadhyay, S., Kropf, A.J., Kemner, K.M., 2006. Evidence of a stable uranyl site in ancient organic-rich calcite. *Environ. Sci. Technol.* 40, 2262–2268.
- Lan, Z.W., Roberts, N.M.W., Zhou, Y., Zhang, S.J., Li, Z.S., Zhao, T.P., 2022a. Application of in situ U–Pb carbonate geochronology to Stenian-Tonian successions of North China. *Precambrian Res.* 370, 106551.
- Lan, Z.W., Wu, S.T., Roberts, N.M.W., Zhang, S.J., Cao, R., Wang, H., Yang, Y.H., 2022b. Geochronological and geochemical constraints on the origin of highly $^{13}\text{C}_{\text{carb}}$ -depleted calcite in basal Ediacaran cap carbonate. *Geol. Mag.* <https://doi.org/10.1017/S001675682200019X>.
- Li, Q., Jiang, Z.X., Hu, W.X., You, X.L., Hao, G.L., Zhang, J.T., Wang, X.L., 2016. Origin of dolomites in the lower cambrian Xiaerbulake formation in the Tarim basin, NW China: implications for porosity development. *J. Asian Earth Sci.* 115, 557–570.
- Liivamägi, S., Šrodoň, J., Bojanowski, M.J., Stanek, J.J., Roberts, N.M.W., 2021. Precambrian paleosols on the great unconformity of the east European craton: an 800 million year record of baltica's climatic conditions. *Precambrian Res.* 363, 106327.
- Liu, H., Zartman, R.E., Ireland, T.R., Sun, W.D., 2019. Global atmospheric oxygen variations recorded by Th/U systematics of igneous rocks. *Proc. Natl. Acad. Sci. USA* 116, 18854–18859.
- Lonner, J., Machel, H.G., 2006. Pervasive dolomitization with subsequent hydrothermal alteration in the clark lake gas field, middle devonian slave point formation, British Columbia, Canada. *AAPG (Am. Assoc. Pet. Geol.) Bull.* 90, 1739–1761.
- Nader, F.H., Swennen, R., Ellam, R., 2004. Reflux stratabound dolostone and hydrothermal volcanism-associated dolostone: a two-stage dolomitization model (Jurassic, Lebanon). *Sedimentology* 51, 339–360.
- Ning, S.Y., Wang, F.Y., Xue, W.D., Zhou, T.F., 2017. Geochemistry of the baoshan pluton in the tongling region of the lower yangtze river belt. *Geochimica* 46, 397–412.
- Paton, C., Hellstrom, J., Paul, B., Woodhead, J., Hergt, J., 2011. Iolite: freeware for the visualisation and processing of mass spectrometric data. *J. Anal. Atomic Spectrom.* 26, 2508–2518.
- Petrus, J.A., Kamber, B.S., 2012. VizualAge: a novel approach to laser ablation ICP-MS U–Pb geochronology data reduction. *Geostand. Geoanal. Res.* 36, 247–270.
- Rasbury, E.T., Present, T.M., Northrup, P., Tappero, R.V., Lanzirrotti, A., Cole, J.M., Wootton, K.M., Hatton, K., 2020. A sample characterization toolkit for carbonate U–Pb geochronology. *Geochronology*. <https://doi.org/10.5194/gchron-2020-20>.
- Reeder, R.J., Lumble, G.M., Northrup, P.A., 1999. XAFS study of the coordination and local relaxation around Co^{2+} , Zn^{2+} , Pb^{2+} , and Ba^{2+} trace elements. *Am. Mineral.* 84, 1049–1060.
- Roberts, N.M.W., Rasbury, E.T., Parrish, R.R., Smith, C.J., Horstwood, M.S.A., Condon, D.J., 2017. A calcite reference material for LA-ICP-MS U–Pb geochronology. *G-cubed* 18, 2807–2814.
- Roberts, N.M.W., Drost, K., Horstwood, M.S., Condon, D.J., Chew, D., Drake, H., Milodowski, A.E., McLean, N.M., Smye, A.J., Walker, R.J., Haslam, R., 2020. Laser ablation inductively coupled plasma mass spectrometry (LA-ICP-MS) U–Pb carbonate geochronology: strategies, progress, and limitations. *Geochronology* 2, 33–61.
- Roberts, N.M.W., Žák, J., Vacek, F., Sláma, J., 2021. No more blind dates with calcite: fluid-flow vs. fault-slip along the Očkov thrust, Prague Basin. *Geosci. Front.* 12, 101143.
- Rochelle-Bates, N., Roberts, N.M.W., Sharp, I., Freitag, U., Verwer, K., Halton, A., Fiordalisi, E., van Dongen, B.E., Swart, R., Ferreira, C.H., Dixon, R., Schröder, S., 2021. Geochronology of volcanically associated hydrocarbon charge in the pre-salt carbonates of the Namibe Basin, Angola. *Geology* 49, 335–340.
- Shannon, R.D., 1976. Revised effective ionic radii and systematic studies of interatomic distances in halides and chalcogenides. *Acta Crystallogr.* A32, 751–767.
- Shao, L.Y., He, H., Peng, S.P., Li, R.J., 2002. Types and origin of dolomites of the cambrian and ordovician of bachu uplift area in Tarim basin. *J. Palaeogeogr.* 4, 19–29 (in Chinese with English abstract).
- Shu, L., Guo, Z., Zhu, W., Lu, H., Wang, B., 2004. Post-collision tectonism and basin range evolution in the Tianshan belt. *Geol. J. China Univ.* 10, 393–404 (in Chinese with English abstract).
- Simpson, A., Glorie, S., Morley, C.K., Roberts, N.M.W., Gillespie, J., Lee, J.K., 2021. In-situ calcite U–Pb geochronology of hydrothermal veins in Thailand: new constraints on Indosinian and Cenozoic deformation. *J. Asian Earth Sci.* 206, 104649.
- Spencer-Cervato, C., Mullis, J., 1992. Chemical study of tectonically controlled hydrothermal dolomitization: an example from the Lessini Mountains, Italy. *Geol. Rundsch.* 81, 347–370.
- Sturchio, N.C., Antonio, M.R., Soderholm, L., Sutton, S.R., Brannon, J.C., 1998. Tetraavalent uranium in calcite. *Science* 281, 971–973.
- Tang, L.J., 1997. Major evolutionary stages of Tarim basin in phanerozoic time. *Earth Sci. Front.* 4, 318–324.
- Tang, L., Zhang, Y., Jin, Z., Jia, C., 2004. Opening–closing cycles of the Tarim and Qaidam basins, northwestern China. *Geol. Bull. China* 23, 254–260.
- Tian, W., Campbell, I.H., Allen, C.M., Guan, P., Pan, W., Chen, M., Yu, H., Zhu, W., 2010. The Tarim picro-basalt-rhyolite suite, a Permian flood basalt from northwest China with contrasting rhyolites produced by fractional crystallization and anatexis. *Contrib. Mineral. Petrol.* 160, 407–425.
- Wang, F.Y., Ge, C., Ning, S.Y., Nie, L.Q., Zhong, G.X., Noel, C.W., 2017. A new approach to LA-ICP-MS mapping and application in geology. *Acta Petrol. Sin.* 33, 3422–3436 (in Chinese with English abstract).

- Woodhead, J.D., Hergt, J.M., 2001. Strontium, neodymium and lead isotope analyses of NIST glass certified reference materials: SRM 610, 612, 614. *Geostand. News* 25, 261–266.
- Wu, S.T., Yang, Y.H., Wang, H., Huang, C., Xie, L.W., Yang, J.H., 2020a. Characteristic performance of guard electrode in LA-SF-ICP-MS for multi-element quantification. *Atom. Spectrosc* 41, 154–161.
- Wu, S.T., Yang, M., Yang, Y.H., Xie, L.W., Huang, C., Wang, H., Yang, J.H., 2020b. Improved in situ zircon U–Pb dating at high spatial resolution (5–16 μm) by laser ablation–single collector–sector field–ICP–MS using Jet sample and X skimmer cones. *Int. J. Mass Spectrom.* 456, 116394 <https://doi.org/10.1016/j.ijms.2020.116394>.
- Wu, S.T., Yang, Y.H., Jochum, K.P., Romer, R.L., Glodny, J., Savov, I.P., Agostini, S., De Hoog, J.C.M., Peters, S.T.M., Kronz, A., Zhang, C., Bao, Z.A., Wang, X.J., Li, Y.L., Yang, J.H., Li, X.H., Wu, F.Y., 2021. Isotopic compositions (Li–B–Si–O–Mg–Sr–Nd–Hf–Pb) and $\text{Fe}^{2+}/\Sigma\text{Fe}$ ratios of three synthetic andesite glass reference materials (ARM-1, ARM-2, ARM-3). *Geostand. Geoanal. Res.* 45, 719–745.
- Wu, S.T., Yang, Y.H., Roberts, N.M.W., Yang, M., Wang, H., Lan, Z.W., Xie, B.H., Li, T.Y., Xu, L., Huang, C., Xie, L.W., Yang, J.H., Wu, F.Y., 2022. In situ calcite U–Pb geochronology by high-sensitivity single-collector LA-SF-ICP-MS. *Sci. China Earth Sci.* 65 <https://doi.org/10.1007/s11430-021-9907-1>.
- Xiao, X., Zhou, T.F., White, N.C., Zhang, L.J., Fan, Y., Wang, F.Y., Chen, X.F., 2018. The formation and trace elements of garnet in the skarn zone from the Xinqiao Cu–S–Fe–Au deposit, Tongling ore district, Anhui Province, Eastern China. *Lithos* 302–303, 467–479.
- Yang, S.F., Li, Z.L., Chen, H.L., Santosh, M., Dong, C.W., Yu, X., 2007. Permian bimodal dyke of Tarim Basin, NW China: geochemical characteristics and tectonic implications. *Gondwana Res.* 12, 113–120.
- Yu, X., Yang, S., Chen, H., Chen, Z., Li, Z., Batt, G.E., Li, Y., 2011. Permian flood basalts from the Tarim Basin, Northwest China: SHRIMP zircon U–Pb dating and geochemical characteristics. *Gondwana Res.* 20, 485–497.
- Zhang, C.L., Li, X.H., Li, Z.X., Ye, H.M., Li, C.N., 2008. A permian layered intrusive complex in the western Tarim block, northwestern China: product of a Ca 275-ma mantle plume? *J. Geol.* 116, 269–287.
- Zhang, C.L., Xu, Y., Li, Z., Wang, H., Ye, H., 2010. Diverse permian magmatism in the Tarim block, NW China: genetically linked to the permian Tarim mantle plume? *Lithos* 119, 537–552.
- Zhang, W., Guan, P., Jian, X., Feng, F., Zou, C.N., 2014. *In situ* geochemistry of Lower Paleozoic dolomites in the northwestern Tarim basin: implications for the nature, origin, and evolution of diagenetic fluids. *G-cubed* 15, 2744–2764.
- Zheng, H.R., Wu, M.B., Wu, X.W., Zhang, T., Liu, C.Y., 2007. Oil–gas exploration prospect of dolomite reservoir in the Lower Paleozoic of Tarim Basin. *Acta Petrol. Sin.* 28, 1–8 (in Chinese with English abstract).
- Zhong, Y.T., Luo, Z.Y., Mundil, R., Wei, X., Liu, H.Q., He, B., Huang, X.L., Tian, W., Xu, Y. G., 2022. Constraining the duration of the Tarim flood basalts (northwestern China): CA–TIMS zircon U–Pb dating of tuffs. *Geol. Soc. Am. Bull.* 134, 325–334.